Faculdade de Engenharia da Universidade do Porto

Finite Element Analysis of a Novel Ligament Fixation Device for Ligamentoplasty Applications

Luís Carlos Machado Martins



Master in Mechanical Engineering
specialization in Machine Design

Supervisor: Dr. Dulce Oliveira

Co-Supervisor: Prof. Dr. Marco Parente

October 1, 2026

Finite Element Analysis of a Novel Ligament Fixation Device for Ligamentoplasty Applications

Luís Carlos Machado Martins

Master in Mechanical Engineering
specialization in Machine Design

October 1, 2026

Author Statement

I, Luís Carlos Machado Martins, declare that I am the sole author of this Master's Dissertation entitled *"Finite Element Analysis of a Novel Ligament Fixation Device for Ligamentoplasty Applications"*. I wrote all sections of this document and all the supplementary materials, and carried out the research presented herein. This work has not previously been submitted or assessed, in English or in any other language, as part of the requirements for any other degree or non-degree programme at this or any other institution.

References to other authors (statements, ideas and thoughts), as well as the use of published works, strictly comply with the applicable rules of attribution and are duly identified in the text and in the bibliographic references. Any figures or materials taken from other works are clearly attributed to their original authors, with the corresponding references. I am aware that plagiarism and self-plagiarism constitute academic offences, as established in the U.Porto Code of Ethics.

Disclosure of Delegation to Generative AI

The author declares the use of generative AI (GAI) in the research and writing process. In accordance with the GAIDeT taxonomy (2025), the following tasks were delegated to GAI tools under full human supervision: Text generation; Proofreading and editing; Reformatting. The GAI tool used was Claude Pro. Responsibility for the final manuscript lies entirely with the author. GAI tools are not listed as authors and do not bear responsibility for the final outcomes. All engineering decisions, data analysis and intellectual contributions remain exclusively the author's own, and all AI-assisted text underwent rigorous manual revision and adaptation.

Licensing

This document is submitted under the terms of the Creative Commons Attribution-NonCommercial-ShareAlike 4.0 International License (full legal code). This means that, while others are free to share, adapt and build upon the content for non-commercial purposes, appropriate credit must be given to the author, Luís Martins, and any derivative works must be licensed under similar terms.

Luís Martins
Faculdade de Engenharia da Universidade do Porto
October 1, 2026

Objetivos de Desenvolvimento Sustentável

Este trabalho relaciona-se diretamente com os Objetivos de Desenvolvimento Sustentável (ODS) das Nações Unidas, em particular os Objetivos 3 e 9, com uma ligação secundária ao Objetivo 12.

ODS 3 — Saúde de Qualidade. A lesão do ligamento cruzado anterior (LCA) é uma das lesões ligamentares mais comuns do joelho, afetando predominantemente uma população jovem e ativa, para quem a reconstrução cirúrgica é o tratamento padrão. O método de fixação mais utilizado atualmente — o parafuso de interferência — tem uma limitação mecânica bem documentada: a própria ação de inserção opõe-se à tensão já aplicada ao enxerto, sendo uma causa reconhecida de laceração e de perda de pré-tensão, com repercussões na estabilidade articular pós-operatória. Este trabalho avalia um conceito de fixação alternativo, especificamente concebido para eliminar essa limitação mecânica, contribuindo para o desenvolvimento de métodos de fixação mais fiáveis e com menor risco de complicação — um contributo direto para a qualidade dos cuidados de saúde músculo-esqueléticos e para o bem-estar de uma população de doentes jovens e ativos.

ODS 9 — Indústria, Inovação e Infraestruturas. O trabalho desenvolve e caracteriza, através de um modelo de elementos finitos combinado com ensaios mecânicos em protótipos impressos em 3D, um dispositivo médico com um princípio de ancoragem geometricamente distinto de todos os métodos de fixação estabelecidos na literatura. A simulação explícita do próprio processo de inserção — ausente de todos os estudos de elementos finitos publicados sobre dispositivos de fixação ligamentar, que assumem consistentemente o estado já montado — representa um contributo metodológico à investigação em engenharia biomédica, demonstrando a aplicação de métodos computacionais avançados ao desenvolvimento inicial de dispositivos médicos inovadores.

ODS 12 — Produção e Consumo Sustentáveis. O material considerado para o dispositivo, o poli(ácido L-láctico) (PLLA), é bioabsorvível — ao contrário de implantes metálicos permanentes, degrada-se progressivamente no organismo, eliminando a necessidade de uma segunda intervenção cirúrgica para remoção de material, com o consequente benefício em termos de recursos de saúde utilizados por doente.

Abstract

Anterior cruciate ligament (ACL) reconstruction depends critically on the mechanical performance of the graft fixation method, yet the most widely used technique — interference screw fixation — anchors the graft through an action that mechanically opposes the tension already applied to it, a recognised source of graft laceration and pretension loss. This thesis evaluates LiFix, a novel intra-tunnel fixation concept that anchors the graft through angled internal spikes rather than radial compression, decoupling the mechanics of insertion from those of anchoring. A finite element model in Abaqus, combining an anisotropic hyperelastic graft representation with finite-sliding frictional contact, simulated both graft insertion and extraction explicitly — distinctively, since published finite element studies of ligament fixation devices are consistently formulated in the already-assembled state. This was complemented by a supplementary ductile damage analysis and by mechanical testing of 3D-printed prototypes.

A central finding emerged from the insertion phase: plastic strain within the spikes, reaching approximately 28% at the tip and mid-height, was found to exceed the elongation-at-break of PLLA before any extraction load was applied. A damage-inclusive simulation, robust across the ductility range reported for the material, predicted fracture of all four spike rows during insertion itself, with fracture location matching that observed in mechanically tested prototypes. This fracture was shown to degrade rather than eliminate fixation capacity, owing to the device's redundant, multi-row architecture. Under idealised, undamaged geometry, the construct achieved a peak extraction load of 581 N (finite element) and 725 ± 108 N (experimental, $n = 3$), matching the range reported for interference screw fixation, with graft stress remaining distributed rather than concentrated as reported for that method in the literature. A preliminary refinement of the spike geometry, evaluated as a single design point without independent mesh convergence or experimental confirmation, brought insertion-phase plastic strain below the fracture-strain criterion, without eliminating plastic deformation altogether, while further improving extraction resistance, indicating that the central limitation identified is a property of the specific geometry tested rather than of the anchoring principle as a whole.

These results characterise the time-zero feasibility of the LiFix concept and identify spike geometry refinement as the priority for its continued development, while not substituting for cyclic loading validation, bone representation, or clinical evidence.

Keywords: ACL reconstruction; ligament fixation device; pull-out strength; finite element analysis; graft insertion mechanics; biomechanics

Resumo

A reconstrução do ligamento cruzado anterior (LCA) depende de forma crítica do desempenho mecânico do método de fixação do enxerto, mas a técnica mais utilizada — o parafuso de interferência — fixa o enxerto através de uma ação que se opõe mecanicamente à tensão já aplicada, uma causa reconhecida de laceração do enxerto e de perda de pré-tensão. Esta dissertação avalia o LiFix, um novo conceito de fixação intratunelar que ancora o enxerto através de espigões internos angulados em vez de compressão radial, dissociando a mecânica da inserção da mecânica da ancoragem. Um modelo de elementos finitos em Abaqus, combinando uma representação hiperelástica anisotrópica do enxerto com contacto friccional de deslizamento livre, simulou explicitamente tanto a inserção como a extração do enxerto — de forma distintiva, já que os estudos de elementos finitos publicados sobre dispositivos de fixação ligamentar assumem consistentemente o estado já montado. Este trabalho foi complementado por uma análise suplementar de dano dúctil e por ensaios mecânicos em protótipos impressos em 3D.

Um ponto central ao sistema de fixação surgiu na fase de inserção: a deformação plástica nos espigões, atingindo aproximadamente 28% na ponta e a meia-altura, revelou-se superior à elongação na rotura do PLLA ainda antes de qualquer carga de extração ser aplicada. Uma simulação com dano, robusta em toda a gama de ductilidade reportada para o material, previu a fratura das quatro filas de espigões já durante a inserção, com localização coincidente com a observada nos protótipos ensaiados mecanicamente. Esta fratura demonstrou degradar, em vez de eliminar, a capacidade de fixação, devido à arquitetura redundante e multi-fila do dispositivo. Sob geometria idealizada e intacta, o construto atingiu uma carga máxima de extração de 581 N (elementos finitos) e 725 ± 108 N (experimental, $n = 3$), equiparável à gama reportada para fixação por parafuso de interferência, com a tensão no enxerto a manter-se distribuída em vez de concentrada, ao contrário do reportado na literatura para esse método. Um refinamento preliminar da geometria dos espigões, avaliado como um único ponto de projeto sem convergência de malha independente nem confirmação experimental, trouxe a deformação plástica na inserção para abaixo do critério de deformação de fratura, sem eliminar por completo a deformação plástica, melhorando simultaneamente a resistência à extração — indicando que a limitação central identificada é uma propriedade da geometria específica testada, não do princípio de ancoragem em si.

Estes resultados caracterizam a viabilidade a tempo-zero do conceito LiFix e identificam o refinamento da geometria dos espigões como prioridade para o seu desenvolvimento

futuro, sem substituírem a validação sob carga cíclica, a representação do osso, ou a evidência clínica.

Palavras-chave: reconstrução do LCA; dispositivo de fixação ligamentar; resistência ao arrancamento; análise por elementos finitos; mecânica de inserção do enxerto; biomecânica

Agradecimentos

Primeiramente, gostava de agradecer às pessoas que tornaram este projeto possível. À Professora Dulce Oliveira, pela ajuda e orientação do projeto, como pela providência de bom ambiente. De seguida, expressar a minha gratidão ao Professor Marco Parente, pelas reuniões onde partilhou o seu conhecimento sobre a área de computação de elementos finitos, e pelo seu bom humor. Um agradecimento também ao Doutor Nuno Camelo por propor o presente conceito e pela consulta prestada ao longo do projeto. À equipa LiFix, agradecer pelo trabalho e camaradagem durante o semestre.

De seguida, às pessoas que me iluminam a vida e fizeram o meu percurso académico possível, a minha família. Aos meus tios, obrigado pelos conselhos, brincadeiras e ajudas. Às minhas tias, obrigado pelo carinho, doces e preocupação. Obrigado ao meu padrinho e madrinha, por estarem sempre dispostos a apoiar-me com o que eu precisasse. Aos meus primos, obrigado pela mentoria, pelo apelo à ousadia e pela alegria.

À minha mana, que esteve longe de mim mas sempre perto, que me alegrou, que foi meiga e prestável comigo enquanto traçava o próprio caminho. E um caminho de excelência, de que o mano se orgulha muito. Um beijinho e um obrigado.

À minha avó, de quem eu sou o gatinho, agradecer por sempre acreditar em mim e ajudar com tudo o que eu precisasse. Obrigado pelo traje, fiz bom uso dele. Terei sempre a minha querida avó associada ao meu percurso académico, e em todos os meus projetos futuros estará presente um bocadinho dela, certamente nas contas de tabuadas.

Obrigado, mãe, porque tudo o que fazes vem de amor. Durante 5 anos a maior adepta da engenharia do filho, e a maior saudade no coração dele. O espírito indomável que me passaste foi muitas vezes o que me valeu para completar esta fase. Um beijinho do teu filhinho.

Ao meu pai, que foi a minha rocha, o meu abrigo e a minha bússola. Obrigado por aturares as minhas asneiras e desarrumações. Por me suportares a viver experiências extra-académicas. Por me aconselhares e respeitares as minhas escolhas. Por me transmitires um espírito de confiança e coragem. Fui feliz aqui.

Há pessoas que fizeram com que esta fase valesse a pena. Pessoas que transformaram um curso de 5 anos numa fase de vida própria, em momentos maiores que o próprio curso. Estes foram a personificação da frase "*Shared joy is a double joy; shared sorrow is half a sorrow*".

Começando pelos que me acompanham há mais de duas décadas, os meus irmãos de coração. Ao André, pela vida que partilhamos juntos, por todas as aventuras, missões e gargalhadas. Continua a ser uma pessoa íntegra, altruísta e não percas a tua chama. Ao Ivo, pelas memórias, pela companhia, pelas conversas e por tudo o que crescemos juntos. Continua o teu caminho, sempre com os olhos postos no que importa. De seguida ao meu amigo Paulo, por me ajudar com tudo, pelas piadas e pela sua mera presença que anima qualquer sala. Estou orgulhoso por todos os teus feitos, continua uma pessoa única.

Por último nesta categoria, os grupos de pessoas que são a definição de segundas famílias. Aos Puessegos, estou muito grato por vos ter conhecido. Por todas as piadas internas, risos, e mágoas que desaparecem no momento em que a porta (ou janela) da Casa do Povo se abre. Por todas as histórias que um dia vamos contar aos nossos filhos e netos. Por cada um de vós. Obrigado, Puessegos. Aos Patos, já que cada um teve um agradecimento personalizado, vou só dizer que me permitiram viver o que o Porto e a academia são verdadeiramente, e que vos vou levar até ao fim, Filhotes. Obrigado, Patos.

Obrigado a todos os que passaram, à minha Jade, e às maiores adversidades, reais e imaginárias, que nos aperfeiçoaram.

Finalmente, obrigado a Deus, Jesus Cristo, que me ama e me ensinou a amar.

Luís Martins || Rei dos Marmelos

"What do you want to be when you grow up?"

"Kind."

Contents

1 Introduction **1**
- 1.1 Context . . . 1
- 1.2 Goal . . . 2
- 1.3 Methodology . . . 3
- 1.4 Structure . . . 3

2 State of the Art **5**
- 2.1 Anatomical context . . . 5
- 2.2 Fixation Methods . . . 7
  - 2.2.1 Interference screws . . . 7
  - 2.2.2 Bone-Patellar-Tendon-Bone graft . . . 9
  - 2.2.3 Suspensory Cortical Fixation . . . 10
  - 2.2.4 Cross-Pins . . . 12
  - 2.2.5 Suture Anchors . . . 14
  - 2.2.6 Staples . . . 16
- 2.3 Comparison between methods . . . 16
- 2.4 Finite element analysis studies on fixation devices . . . 18

3 Methods **21**
- 3.1 SolidWorks Environment . . . 22
- 3.2 Abaqus Environment . . . 23
  - 3.2.1 Tendon geometry . . . 23
  - 3.2.2 Materials . . . 24
  - 3.2.3 Step and Boundary Conditions . . . 25
  - 3.2.4 Interaction . . . 26
  - 3.2.5 Mesh . . . 26

4 Results **29**
- 4.1 Insertion results . . . 29
- 4.2 Pull out results . . . 30
- 4.3 Fixator Stress and Strain fields . . . 32
- 4.4 Graft focused results . . . 35
- 4.5 Damage inclusive insertion results . . . 37

5 Mechanical Test **39**
- 5.1 Materials . . . 39
- 5.2 Methods . . . 40
- 5.3 Parameter of interest . . . 42

5.4 Results 42

6 Discussion **45**
6.1 Overview 45
6.2 Numeric model interpretation 45
6.2.1 Insertion mechanics 45
6.2.2 Pull out 49
6.2.3 Graft response 50
6.3 Comparison with the literature 52
6.3.1 Biomechanical positioning against established fixation methods . . . 52
6.3.2 Methodological comparison with the finite element literature 54
6.3.3 Summary of contribution relative to prior work 56
6.4 Design Implications 56
6.5 Limitations and Assumptions 58

7 Preliminary Spike Geometry Refinement **63**
7.1 Design Changes 63
7.2 Results 64
7.3 Discussion 66

8 Conclusion **69**

9 Future Works **73**

References **77**

Appendix **87**

List of Figures

2.1 Anatomical representation of the human knee joint . . . 6
2.2 The two bundles of the ACL . . . 7
2.3 Interference screw fixation of the ACL . . . 8
2.4 BPTB fixation with interference screw . . . 9
2.5 Fixed-loop and Adjustable-Loop devices . . . 11
2.6 Alignment of the Cross Pins in the fixation procedure . . . 12
2.7 Cross Pins Fixation visualisation . . . 12
2.8 Suture anchor fixation of the ACL . . . 14
2.9 Post-operative X-ray showing patellar suture anchors and interference screw 15
2.10 Radiographs of a post operative knee with three staples, interference screw, and endobutton . . . 16
2.11 Comparison between methods of Maximum Failure Load . . . 18

3.1 Method flowchart . . . 21
3.2 LiFix SolidWorks Model . . . 23
3.3 Tendon graft geometry . . . 24
3.4 Mesh convergence study . . . 27
3.5 Final mesh of the fixator system . . . 28

4.1 Insertion Force as a function of time across Step 1 . . . 29
4.2 Insertion Force as a function of Displacement across Step 1 . . . 30
4.3 Pull out Force as a function of Displacement across Step 2 . . . 31
4.4 Pull out Force as a function of time across Step 2 . . . 31
4.5 Fixator von Mises Stress distribution at t = 0.1 s . . . 32
4.6 Fixator von Mises Stress distribution at t = 0.1 s — spike detail . . . 32
4.7 Fixator von Mises Stress distribution at t = 0.2 s . . . 33
4.8 Fixator von Mises Stress distribution at t = 0.2 s — spike detail . . . 33
4.9 Fixator PE Max Principal distribution at t = 0.1 s . . . 34
4.10 Fixator PE Max Principal distribution at t = 0.1 s — Cross sectional detail 34
4.11 Fixator PEEQ distribution at t = 0.1 s . . . 34
4.12 Fixator PE Max Principal distribution at t = 0.2 s . . . 35
4.13 Fixator PEEQ distribution at t = 0.2 s . . . 35
4.14 Graft von Mises Stress distribution at t = 0.165 s . . . 36
4.15 Global system von Mises Stress distribution at t = 0.165 s . . . 36
4.16 Displacement as a function of time across Step 2 of 3 nodes — pulled face node (orange), node before the fixator (green) and node after the fixator (blue) . . . 37
4.17 resulting fixator geometry for the conservative case (fracture strain 0.03) . . 38

4.18 resulting fixator geometry for the upper-bound case (fracture strain 0.08) . 38

5.1 MultiTest-dV Motorised force tester machine 41
5.2 Experimental tests configuration 41
5.3 Test 1 43
5.4 Test 2 43
5.5 Test 3 44

6.1 FE model and experimental tests benchmark against previous method comparison 53

7.1 Refined spike geometry, showing the curved engagement face across all four spike rows 64
7.2 Refined spike geometry, showing the wider spike tip and reduced spike protrusion 64
7.3 Refined geometry: pull out force as a function of time 65
7.4 Refined geometry: PE Max Principal at the end of insertion (Step 1, t = 0.1 s), cross-sectional detail 65
7.5 Refined geometry under the damage-inclusive insertion model (fracture strain 0.08): spike geometry remains intact 66

List of Tables

2.1 Biomechanical Comparison Matrix of Ligament Fixation Methods 17

3.1 Parameter values for the tendon HGO model 24
3.2 PLLA plastic stress–strain curve values (isotropic hardening) 25
3.3 Mesh convergence study: reaction force (pull out) as a function of mesh refinement 27

5.1 Comprehensive Material Properties: PLA vs PLLA 39
5.2 Nylon rope properties used as graft surrogate 40
5.3 Descriptive statistics of the measured values 44

6.1 Biomechanical comparison of LiFix (numerical and experimental) against interference screw fixation 52

7.1 Comparison between the original and refined spike geometries 66

Acronyms

ACL	anterior cruciate ligament
AMB	anteromedial bundle
AP	anteroposterior
BC	boundary condition
BPTB	bone-patellar tendon-bone
CPRESS	contact pressure
CT	computed tomography
FDA	Food and Drug Administration
FE	finite element
FEM	finite element method
HGO	Holzapfel-Gasser-Ogden
LCL	lateral collateral ligament
MCL	medial collateral ligament
MPFL	medial patellofemoral ligament
MRI	magnetic resonance imaging
PA6	polyamide 6
PCL	posterior cruciate ligament
PE	plastic strain
PEEQ	equivalent plastic strain
PLA	polylactic acid
PLB	posterolateral bundle
PLLA	poly-L-lactic acid
RCT	randomised controlled trial
RF3	reaction force in the 3-direction (Z-axis)
TCP	tricalcium phosphate
U3	displacement in the 3-direction (Z-axis)
UHMWPE	ultra-high-molecular-weight polyethylene

Chapter 1

Introduction

1.1 Context

Anterior cruciate ligament (ACL) rupture is among the most common ligamentous injuries of the knee, and its surgical management has been studied extensively worldwide, though with notable disparities in both incidence and surveillance. In the United States, the annual incidence of ACL reconstruction rose from approximately 87 000 to nearly 130 000 procedures between 1994 and 2006, based on national hospital discharge data [1]. Considerable international variation exists beyond this figure: a comparison of national knee ligament registries across four countries reported annual incidences ranging from 4.1 to 51.3 reconstructions per 100 000 inhabitants [2]. Within Europe, the Scandinavian countries maintain the most established national surveillance, reporting annual incidences of 32 to 38 reconstructions per 100 000 inhabitants [3]. No equivalent national registry or dedicated epidemiological study of ACL reconstruction incidence in Portugal was identified in the literature, an absence that is itself indicative of the lack of standardised national surveillance for this procedure outside a small number of countries.

Regardless of the precise incidence in any given setting, ACL reconstruction is the established standard of care for restoring joint stability in active patients, and its long-term success depends not only on graft selection but, critically, on the mechanical performance of the fixation method used to anchor the graft within the bone tunnels — sufficient initial fixation strength and stiffness are required to withstand early rehabilitation loads without excessive slippage, while the fixation itself must not compromise the graft during implantation.

A range of fixation strategies is available, spanning aperture compression (interference screws), suspensory cortical fixation, transfixation (cross-pins), suture anchors, and staples, reviewed in detail in Chapter 2. Each method involves a distinct mechanical trade-off between fixation strength, graft preservation, and surgical complexity, and none has emerged as unambiguously superior across all outcome measures. Of particular relevance to the present work is a limitation specific to interference screw fixation, currently the

most widely used method in orthopaedic sports medicine: the screw is inserted alongside an already-tensioned graft, and this insertion action mechanically opposes the applied tension, a recognised source of graft laceration and of pretension loss that can manifest clinically as early postoperative laxity. Other methods carry their own characteristic vulnerabilities — cyclic elongation in suspensory loop systems, pin migration in cross-pin transfixation, bone matrix yielding in suture anchor constructs — discussed at length in Section 2.2.

This thesis is motivated by a novel fixation concept, developed to address the specific limitation of interference screw fixation described above, by decoupling the mechanics of graft insertion from those of graft anchoring. Rather than generating fixation through radial compression applied during assembly, the concept under investigation — LiFix — anchors the graft through an array of angled internal spikes that permit low-resistance insertion in one direction while resisting motion in the reverse direction, without requiring an action that opposes graft tensioning.

Evaluating a novel fixation concept of this kind poses a practical challenge: physical prototyping and mechanical testing alone are costly and slow to iterate, and provide limited insight into the internal stress and strain fields that govern failure. Finite element analysis has been increasingly used to address this gap for established fixation methods, offering a means to predict stress distribution, contact behaviour, and load–displacement response prior to, or in support of, experimental testing (Section 2.4). However, published finite element studies of ligament fixation devices are consistently formulated in the already-assembled, seated configuration: the graft and implant are positioned in their final geometry before the analysis begins, and the assembly manoeuvre itself is not modelled. For an interference screw, whose insertion and fixation mechanisms are largely independent actions, this simplification is reasonable. For a concept such as LiFix, in which insertion and fixation share the same geometric features, it is not: the two cannot be meaningfully separated, and a model that begins from the seated state cannot characterise whether, or how, the device maintains its structural integrity on assembly.

1.2 Goal

The goal of this thesis is to evaluate, through finite element analysis complemented by mechanical testing, the mechanical performance of the LiFix ligament fixation device — including, distinctively, the graft insertion process itself — and to position this performance against established interference screw fixation and the wider biomechanical literature on ACL graft fixation.

This overarching goal is pursued through four more specific objectives: to characterise the mechanical response of the device during graft insertion, including the resistance it presents to assembly and the state of the device at the end of that process; to characterise

its resistance to graft extraction, its stiffness, and its mode of failure under load; to validate these numerical predictions, where possible, against mechanical testing of 3D-printed prototypes; and to identify, on this basis, the design refinements the present geometry would require ahead of further development.

1.3 Methodology

The approach combines computational and experimental methods. A finite element model of the LiFix device and a graft surrogate was developed in Abaqus, comprising sequential simulations of graft insertion and extraction under an anisotropic hyperelastic representation of the graft and finite-sliding frictional contact between graft and implant (Chapter 3). This was complemented by a supplementary damage-based analysis to assess the consequences of local material overload that the base material model cannot otherwise represent (Chapter 6). In parallel, 3D-printed prototypes of the device were mechanically tested under monotonic tensile loading to obtain an independent measure of pull out resistance (Chapter 5). The numerical and experimental results are interpreted jointly, and compared against the biomechanical benchmarks established in the literature for interference screw and other fixation methods covered in Chapter 2.

1.4 Structure

This thesis is organised as follows. Chapter 2 reviews the anatomical context of the ACL, the established fixation methods used in its reconstruction, and prior finite element studies of fixation devices. Chapter 3 describes the development of the finite element model, including the device and graft geometry, material representations, and simulation setup. Chapter 4 presents the numerical results obtained from the insertion and extraction simulations. Chapter 5 describes the mechanical testing of the 3D-printed prototypes and its results. Chapter 6 discusses and interprets these results jointly, situating them against the biomechanical literature and drawing out the resulting implications for the device's design. Chapter 7 reports a preliminary refinement of the spike geometry, informed by the findings of Chapter 6. Chapter 8 presents the conclusions of this work, and Chapter 9 outlines directions for future development.

Chapter 2

State of the Art

2.1 Anatomical context

The novel fixation mechanism developed in this work was conceptualised with a versatile structural architecture suitable for broader ligamentoplasty applications. This thesis will focus explicitly on ACL reconstruction. This strategic narrowing of scope is dictated by both clinical realities and mechanical pragmatism. From a literature standpoint, the ACL represents the most extensively documented model in sports medicine and orthopaedic biomechanics. Decades of clinical outcomes, failure mode analyses, and established benchmark data offer a comparative baseline to rigorously validate a new device.

Furthermore, the macro-anatomical scale of the knee joint and the native ACL complex provides a highly practical environment for engineering validation. Designing and prototyping a novel fixator for smaller, highly constrained articular spaces introduces severe spatial limitations that can mask fundamental mechanical behaviour during early-stage testing. Consequently, the knee joint and the ACL serve as the ideal benchmark environment to refine, test, and perfect the baseline mechanical performance of this novel design before downsizing or adapting its architectural principles to more geometrically restrictive ligamentous repairs.

From a mechanical engineering perspective, evaluating an orthopaedic implant within the tibiofemoral assembly necessitates a fundamental baseline understanding of the host joint's global architecture. The human knee joint (Figure 2.1) is a complex, non-congruent synovial articulation that concurrently satisfies two mutually opposing mechanical requirements: substantial weight-bearing capacity and multi-axial rotational mobility [4]. The weight-bearing core of this system comprises the medial and lateral condylar interfaces between the asymmetric, curved surfaces of the distal femur and the flattened plateaus of the proximal tibia [4]. Passive structural integrity and directional constraint are provided by a dedicated soft-tissue network, within which the ACL serves as the primary mechanical restraint against anterior tibial translation, while secondary stabilisation is provided by the posterior cruciate ligament (PCL), the medial collateral ligament (MCL) and the

lateral collateral ligament (LCL) [4].

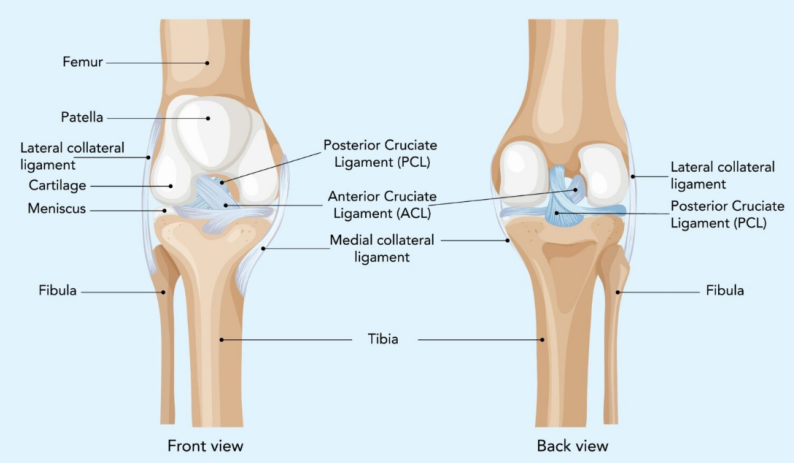


Figure 2.1: Anatomical representation of the human knee joint. Adapted from [5].

The ACL is a dense, intra-articular but extrasynovial band of fibrous connective tissue that extends obliquely from the posterior aspect of the medial wall of the lateral femoral condyle to the anterior intercondylar fossa of the tibia [4]. Macro-anatomically, the native ACL presents an average length ranging between 31 and 38 mm, with a cross-sectional area that varies along its longitudinal axis [4]. Structurally, the ligament is not a uniform homogeneous entity but is composed of tightly packed type-I collagen fibrils aligned parallel to the primary structural load path, interspersed with a specialised proteoglycan matrix that governs its highly non-linear, viscoelastic behaviour.

Functionally, the ACL is divided into two distinct, primary anatomical bundles named according to their relative spatial locations on the tibial footprint: the anteromedial bundle (AMB) and the posterolateral bundle (PLB), as shown in Figure 2.2. These two functional components act in a reciprocal manner to provide consistent structural restraint throughout the entire range of knee kinematics [4].

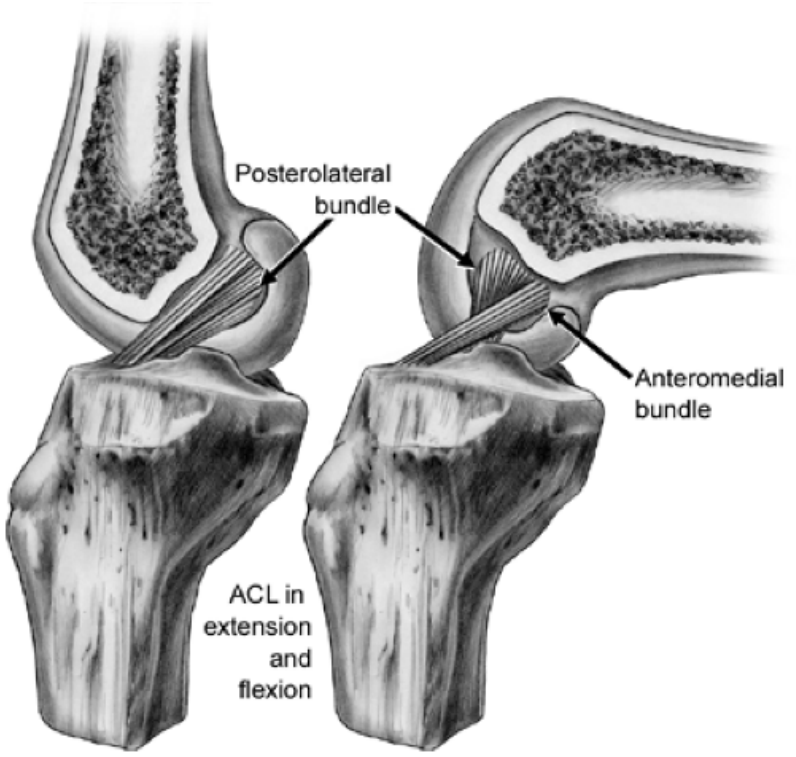


Figure 2.2: Two bundle constitution of the ACL, sourced from [6].

2.2 Fixation Methods

Fixation devices in ligament reconstruction — predominantly in ACL reconstruction — fall into three main categories: compression/interference, suspensory, and hybrid strategies. Each has distinct biomechanical tradeoffs, and finite element analysis is increasingly used to evaluate their performance. To understand the stress fields and load–displacement behaviour computed in numerical simulations, it is necessary to first categorise these devices by their physical anchoring mechanics, insertion methodologies, and structural variants. Therefore, up next is a brief but comprehensive review on some fixation methods for each category of fixation. These were chosen because they are the most prevalent in ACL ligamentoplasty.

2.2.1 Interference screws

Interference screws represent the most widely used fixation method in orthopaedic sports medicine. Operating on the principle of aperture fixation, these devices achieve mechanical stability by establishing direct compression within the bone tunnel, physically jamming the soft-tissue or bone-block graft against the host osseous wall [4], as it can be seen in Figure 2.3. By securing the graft right at the joint line (aperture), this mechanism minimises the unconstrained length of the graft within the tunnel, effectively eliminating axial graft motion and minimising localised tunnel widening [7][8].



Figure 2.3: Interference screw fixation of the ACL, sourced from [9].

From a material standpoint, interference screws are broadly divided into metallic and bioabsorbable variants [10]:

- **Metallic Screws:** Typically manufactured from titanium alloys, these screws are historically considered the "gold standard" for bone-patellar tendon-bone (BPTB) grafts, covered in the next subsection. They offer exceptional torsional and shear resistance during insertion and provide highly predictable, immediate rigid fixation. Their primary clinical drawbacks include permanent artifacts on follow-up magnetic resonance imaging (MRI) and the frequent necessity for a secondary surgical removal in symptomatic patients or during revision scenarios.
- **Bioabsorbable Screws:** Developed to mitigate the long-term presence of permanent hardware, these screws are fabricated from polymers such as poly-L-lactic acid (PLLA) or composite biomaterials containing osteoconductive ceramics like tricalcium phosphate (TCP). While they gradually degrade to allow bone ingrowth, they exhibit a higher incidence of intraoperative breakage due to lower structural toughness, and their degradation profiles can occasionally trigger localised aseptic inflammatory reactions or incomplete bone remodelling within the tunnel space.

In terms of architectural geometry, these screws feature specialised thread profiles designed to maximise pull-out strength while minimising structural laceration of the delicate

soft-tissue graft fibres during insertion. However, in soft-tissue hamstring graft reconstructions, the concentrated compression and shear stresses generated at the screw-graft-bone junction represent a common mechanical failure zone, often leading to localised graft cutting, tissue slippage, or stress concentrations that are highly visible in finite element contact formulations [10].

Across randomised trials and meta-analyses, knee function and laxity were broadly similar. Biomechanically, some test systems still find little difference in acute fixation strength between the two materials: one porcine ACL study reported no difference in stiffness or ultimate failure load between metallic and bioabsorbable screws [11].

In finite element work, screw material clearly changes the local stress field under load [12].

2.2.2 Bone-Patellar-Tendon-Bone graft

BPTB autografts represent a distinct structural classification in reconstruction mechanics due to the inclusion of solid cortical-cancellous bone blocks at both ends of the soft-tissue tendon construct.

When secured via interference screws, the primary fixation mode transitions from tendon-on-bone friction to a rigid bone-to-bone interface within the osseous tunnels [13], as shown in Figure 2.4. This geometric configuration permits a highly efficient mechanical interlocking mechanism, as the metallic or polymeric screw threads bite directly into the parallel bone blocks, compressing them firmly against the host tunnel wall [11]. This aperture compression minimises early construct micromotion, providing exceptional initial pull-out strength and structural stiffness that closely mirrors the native ligament's viscoelastic profile [13].



Figure 2.4: BPTB fixation with interference screw, sourced from [15].

However, optimising the load distribution across this interface demands precise spatial alignment during implant insertion. To prevent premature mechanical failure, the interference screw must be driven perfectly parallel to the longitudinal axis of the bone block. Divergence between the screw axis and the bone block reduces the active thread engagement area, leading to localised stress concentrations and a severe drop in ultimate torque resistance during insertion [13].

The host bone tunnel wall must also possess sufficient local mineral density to withstand the radial expansion forces exerted by the screw. If the tunnel wall undergoes mechanical yielding or fracturing during insertion, the structural construct loses its compressive pre-load, resulting in catastrophic graft slippage under cyclic tensile loads [14].

2.2.3 Suspensory Cortical Fixation

Suspensory cortical fixation uses a remote tensile anchoring mechanism. Instead of filling the bone tunnel with an interference screw to clamp the graft locally, suspensory systems hang the graft loop from the dense outer cortical shell of the bone using a low-profile metallic button. This method eliminates the risk of graft laceration caused by screw threads and is highly favoured for soft-tissue hamstring constructs. However, from a structural mechanics perspective, the engineering design of the loop connection introduces distinct stability trade-offs [16][17][18].

2.2.3.1 Fixed-Loop Suspensory Systems

Fixed-loop devices feature a continuous, continuous-loop woven polyester or ultra-high-molecular-weight polyethylene (UHMWPE) suture loop manufactured to a strict, predetermined length.

Because the loop cannot change size, its mechanical profile is characterised by high ultimate tensile strength and moderate structural material deformation under peak cyclic loads [18].

However, this creates a major geometric constraint: the surgeon must drill the bone tunnel to an exact depth to allow the button to fully exit the cortical bone, flip flat against the cortex, and simultaneously ensure the graft occupies the active joint space.

More importantly, fixed loops increase the effective unconstrained length of the graft construct. Because the graft is anchored far from the joint line at the cortical exit rather than right at the tunnel aperture, the entire length of the suture loop and the intra-tunnel graft acts as a dynamic spring [18].

2.2.3.2 Adjustable-Loop Suspensory Systems

To eliminate the rigid geometric requirements and micro-movements of fixed loops, adjustable-loop suspensory devices utilise a dynamic, self-locking loop configuration based on a friction-hitch or splice design, shown in Figure 2.5. This mechanism allows the loop length

to be post-operatively tensioned and shortened after the button has flipped on the cortex, completely drawing the graft up to fill the entire length of the bone tunnel [16][17][19].

While adjustable loops optimise graft-tunnel placement and shorten the unconstrained construct length to mitigate the bungee effect, they introduce a distinct mechanical vulnerability: loop slippage under dynamic loading. The self-locking knots rely heavily on the frictional coefficients of the woven UHMWPE strands. Under high peak tensile forces or repetitive cyclic loading experienced during aggressive knee motion, microscopic slipping within the internal splice mechanism can occur [20].

This mechanical creep increases the length of the loop, leading to construct elongation, reduced structural stiffness, and subsequent graft laxity. For this reason, retensioning, knot tying, and rehabilitation protocol are a common practice.

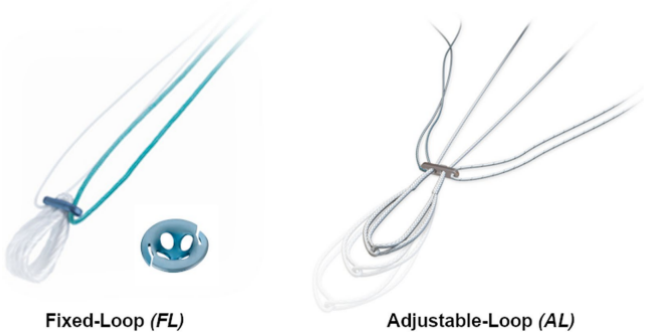


Figure 2.5: Fixed-loop and Adjustable-Loop devices, sourced from [21].

2.2.4 Cross-Pins

Cross-pin fixation (also referred to as transfixation) represents a highly specialised mechanical subset of the suspensory method. Instead of suspending the graft from a remote button resting on the outer cortical shell, cross-pin systems utilise one or two horizontal pins, normally engineered from either metallic alloys or advanced bio-absorbable polymers, driven transversely across the longitudinal femoral bone tunnel, as represented in Figure 2.6, where a part of the surgical procedure is made evident. The soft-tissue or bone graft loop is passed directly over the horizontal pin body, suspending it inside the tunnel, seen in Figure 2.7. This fixation splits the absolute tensile load of the graft across two distinct anchoring points where the horizontal pin exits the medial and lateral walls of the bone tunnel. This dual-cortex bridge design distributes shear and bending moments efficiently into the surrounding cancellous and cortical bone matrix [22].

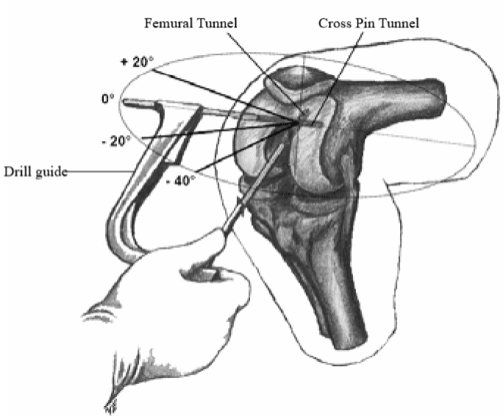


Figure 2.6: Alignment of the Cross Pins in the fixation procedure, adapted from [25].

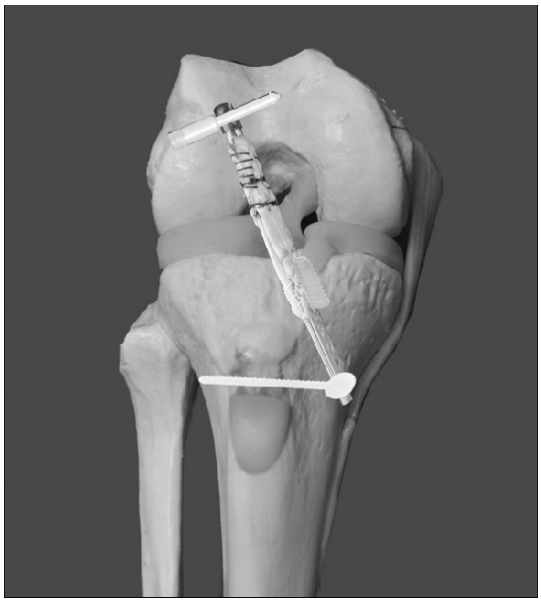


Figure 2.7: Cross Pins Fixation visualisation, sourced from [26].

By shifting the suspension axis closer to the intra-articular joint line compared to remote cortical buttons, transfixation devices reduce the effective unconstrained length of the graft construct [23]. This in turn may decrease the effect of the Windshield-Wiper (sagittal/coronal micromotion where the graft sways transversely against the tunnel walls) and Bungee Effects (longitudinal micromotion where the graft shifts axially up and down within the bone tunnel during flexion-extension cycles) [24].

Despite their high mechanical stiffness [23][27] and favourable spatial proximity to the joint space, transfixation systems exhibit specific structural failure risks:

- Structural Pin Bending and Shear Yielding: Under extreme cyclical loading or acute traumatic overload, the horizontal pin is subjected to pure three-point bending and transverse shear stress. If the peak tensile force exceeds the ultimate material threshold, it can undergo plastic deformation or fracture, leading to sudden graft construct displacement [28].

- Host Cancellous Bone Condensation: Because the cross-pin sits perpendicular to the graft tension line, the downward pull can crush or compress low-density cancellous bone directly underneath the pin's exit points. This localised bone yielding leads to dynamic pin migration, introducing structural construct elongation and joint laxity [29].

- Surgical Insertion Fracture Risks: The requirement to drill a secondary, transverse intersecting guide tunnel across the primary femoral tunnel introduces local stress concentrations in the femoral condyle. Imprecise positioning or excessive insertion torque can result in localised fracturing of the thin posterior cortical wall of the femur [30].

2.2.5 Suture Anchors

Suture anchors represent a specialised, low-profile variant of the suspensory method. They represent improved early biomechanical stability in selected settings, with the strongest support coming from supplemental tibial fixation for BPTB grafts, onlay fixation for medial patellofemoral ligament (MPFL) reconstruction, and repair of tibial avulsion-type lesions. Their application in ACL reconstruction is primarily targeted toward soft-tissue graft socket fixation, pediatric ACL repairs, or as a secondary reinforcement mechanism to supplement primary tibial or femoral fixation [31][32].

The system relies on inserting a threaded or barbed anchor body into the bone matrix, with high-strength sutures extending from the anchor eyelet to secure the graft tissue, as can be seen in Figure 2.8.

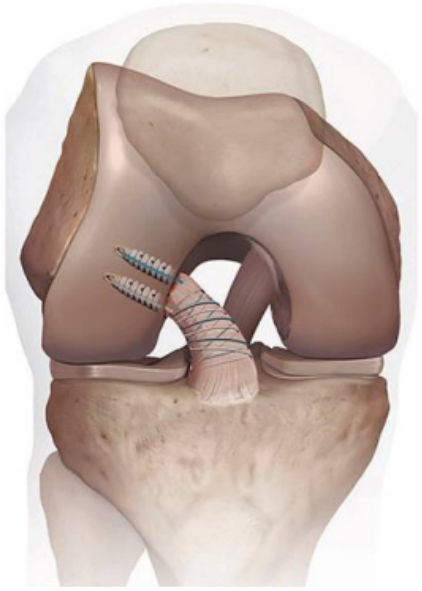


Figure 2.8: Suture anchor fixation of the ACL, sourced from [33].

There is a design split between conventional suture-anchor constructs and all-suture anchors. Comparing all-suture anchors with larger interference implants it is found that all-suture anchors had comparable cyclic elongation to interference fixation on both the femoral and patellar sides, while also requiring less bone removal. This may reduce patellar fracture risk and simplify fixation in the setting of open femoral growth plates. That makes all-suture anchors especially attractive where bone preservation matters, such as pediatric or small-bone applications, but not obviously superior for raw load-bearing capacity [34].

From a mechanical standpoint, suture anchors act as a focal point of suspension. The absolute tensile load experienced by the joint is transmitted directly from the graft, through the high-strength suture strands, and into the core eyelet of the anchor embedded within the cancellous or cortical bone [34]. Because the anchor body sits flush with

or slightly below the osseous aperture, it brings the effective fixation axis closer to the intra-articular space than remote cortical buttons. However, because the connection depends entirely on the compliance of the intervening suture lines, the construct behaves like a highly localised suspension system. This configuration limits macroscopic transverse movement but remains vulnerable to microscopic longitudinal elongation under repetitive, cyclical loads if the suture material undergoes creeping or knot elongation [35].

Suture anchor constructs are prone to specific, localised structural failure modes due to their distinct mechanical interfaces:

- Anchor Pull-Out / Bone Matrix Yielding: The primary failure mode in low-density or osteopenic cancellous bone is the complete structural dislodgement of the anchor body. If the localised shear stresses exceed the holding capacity of the surrounding trabecular bone, the anchor strips through the osseous matrix, resulting in immediate construct failure [36].
- Suture Eyelet Cutting and Mechanical Abrasion: During dynamic loading, the high-strength suture strands experience friction as they slide through the anchor's eyelet. Sharp edges on metallic anchors or tight radii on polymer anchors can act as stress risers, causing progressive structural fraying and acute material failure of the suture strands [37].
- Suture Creep and Knot Slippage: Even if the anchor body remains rigidly fixed in the bone, the construct can experience progressive elongation under cyclic loading. This occurs due to material "creep" (permanent deformation under constant stress) within the ultra-high-molecular-weight polyethylene braids or subtle structural tightening and slippage of the locking knots securing the graft tissue [38].

Overall, this type of fixation can be competitive when used as supplemental/hybrid fixation, being a site and geometry specific standalone option. Figure 2.9 shows a hybrid application of this type of fixation.

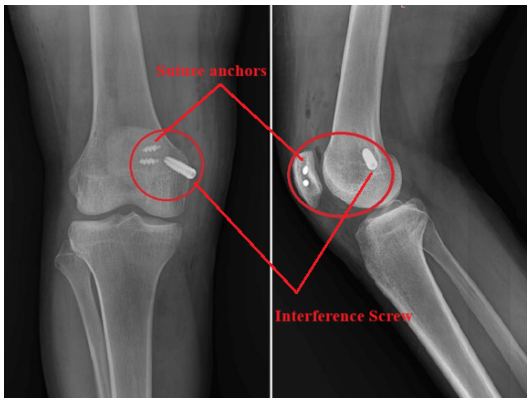


Figure 2.9: Post-operative X-ray showing patellar suture anchors and interference screw, adapted from [39].

2.2.6 Staples

Staples represent a classic, surface-level application of the compression method. Rather than generating compression internally within the bone tunnel (like an interference screw), staples provide local, external compression by clamping the graft tissue directly against the outer cortical shell of the host bone [40] [41]. In contemporary ACL surgery, staples are predominantly utilised on the tibial side, acting either as a primary low-cost option for peripheral ligament reconstruction or as a supplementary backup fixation mechanism to reinforce an interference screw or suspensory device when a graft-tunnel mismatch occurs [42], thus enabling a hybrid fixation apparatus, made evident in Figure 2.10.

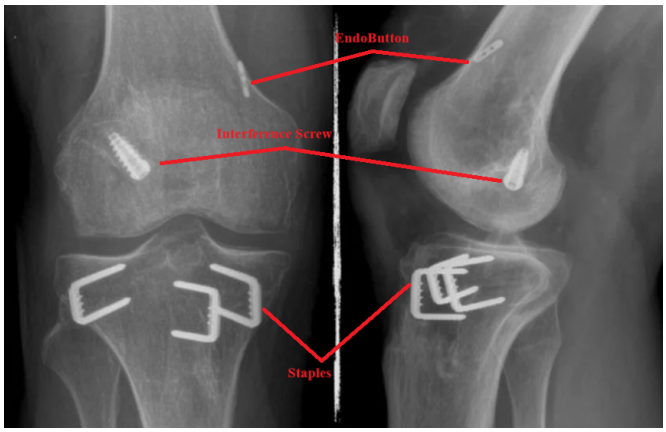


Figure 2.10: Radiographs of a post operative knee with three staples, interference screw and endobutton, adapted from [43].

Basic staples feature smooth prongs that anchor directly into the cortex. However, modern designs incorporate downward-facing spikes or teeth on the underside of the cross-bar and along the prongs. These spikes mechanically bite into the soft-tissue graft strands, preventing the tissue from slipping laterally out from under the implant bridge under load. There are multi-prong configurations, for example 2-prong profiles or wider 4-prong matrices, which increase the overall geometric footprint to distribute compressive forces across a broader surface area of the tendon graft.

Because staples reside entirely on top of the outer cortical surface, they create a raised mechanical profile beneath the overlying soft tissue and skin. On the proximal medial tibia, this prominent hardware frequently causes localised bursitis, hardware-related pain during knee flexion, or skin irritation, often necessitating a secondary surgical procedure for hardware removal after biological integration has occurred [44][45].

2.3 Comparison between methods

As shown, each method offers specific advantages and disadvantages of fixation and each injury should be analysed and treated with that in mind.

Nevertheless, there is a comparison to be made about certain parameters of fixation. Namely, maximum pull out force, allowable slippage, fixation stiffness and mode of failure, as it can be seen in Table 2.1.

Table 2.1: Biomechanical Comparison Matrix of Ligament Fixation Methods

	Interference Screw	**BPTB Screw**	**Suspensory**	**Cross Pins**	**Sutures**	**Staples**
Maximum Failure Load	602–632 N [46] [47]	535–805 N [48] [49]	864–1444 N (adjustable); 1313 ± 258 N (fixed) [16]	737 ± 140 N [50]	282 ± 82 N (alone, MPFL reconstruction) [51]; 330 N (hybrid BPTB) [52]; 918 ± 58 N (hybrid bioscrew) [53]	588 N (alone) [41]; 619 ± 9 N (hybrid bioscrew) [53]
Cyclic Slippage	2.48–2.82 mm at 50–250 N for 1000 cycles [47] [46]	0.32 mm at 110 N [48] up to 9.2 mm at failure [54].	Ranges from 3.7 mm (fixed) 7.7 mm (adjustable) 2000 cycles at 400 N [16]	6 mm at 0–150 N for 1000 cycles [55]	5.4–6.0 mm at 10–50 N for 1000 cycles [56]	—
Construct Stiffness	101–152 N/mm [46]	168 ± 42 N/mm [57]	170 N/mm (adjustable); 187 N/mm (fixed) [58]	184 N/mm [55]	98 N/mm [52]	344.81 ± 44.97 N/mm [53]
Common failure modes	Graft slippage/pullout; laceration	Bone block fracture	Loop elongation/slippage (adjustable); Loop rupture; Cortical pull-through (fixed)	Pin malposition / migration; Laceration	Suture rupture; Graft pullout	Laceration; loosening

For comparison, a native ACL has an ultimate tensile strength of 2195 ± 427 N and a stiffness of 306 ± 80 N/mm [59]. It is capable of extending its length up to 15% in normal activities [60], and 30% in tensile testing [61].

Figure 2.11 shows a graph illustrating the Maximum Failure Load of all the methods mentioned.

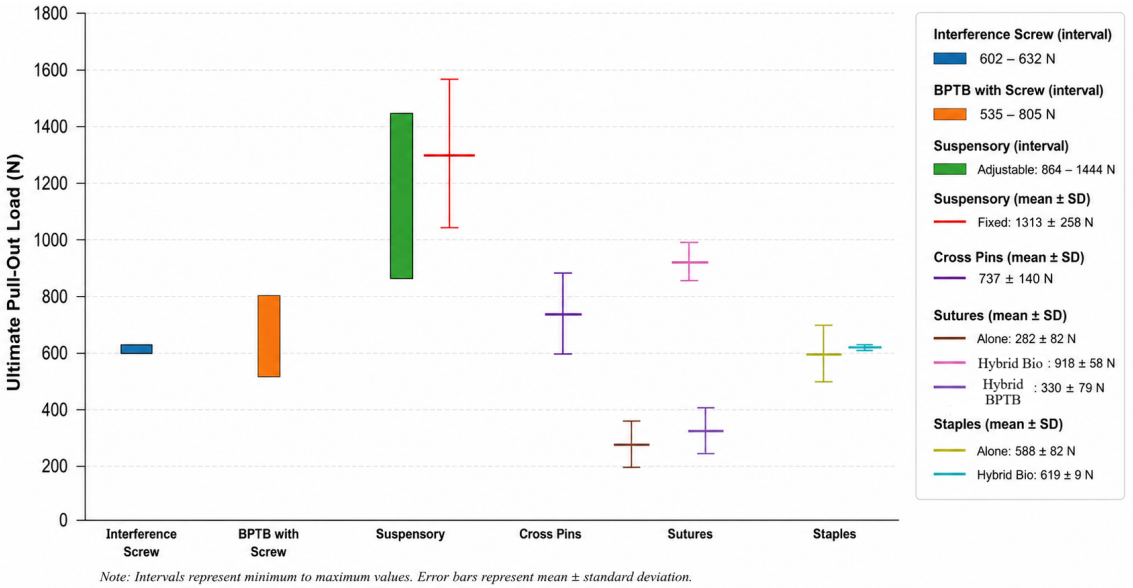


Figure 2.11: Comparison between methods of Maximum Failure Load

2.4 Finite element analysis studies on fixation devices

For soft-tissue interference screws, Chizari et al. [62] built a computed tomography (CT)-based model of tibial screw fixation and compared the numerical results with porcine mechanical tests; they used a hyperelastic graft model and examined rigidity under single-cycle and cyclic loading, with the model predicting stress, strain, and displacement in the tunnel wall. Abdullah et al. [12] then used finite element (FE) to compare screw materials under a 200 N tensile load; all versions stayed below 40 MPa von Mises stress and below 0.06 mm displacement, with stiffer materials showing higher stress variation. The broader FE reviews conclude that these models are useful for optimising tunnel position, graft pretension, and screw design, but they also report that most published models still simplify soft tissues with isotropic linear elastic assumptions [63].

For BPTB interference screw fixation, the FE-specific evidence is thinner than for soft-tissue grafts. Barcia et al. [64], who simulated ACL reconstruction with a tibial interference screw in porcine samples, reported that the choice of trabecular bone constitutive model did not greatly change the simulation outcome.

Suspensory fixation has the strongest mix of biomechanical and computational attention after interference screws. O'Brien et al. [65] showed that manual tensioning missed deployment errors in about a quarter of cases, including soft-tissue interposition and improperly flipped buttons, which is exactly the sort of issue a model can help anticipate. In biomechanical comparisons, the larger construct literature shows fixed-loop and button

devices can be strong, but they are more vulnerable to cyclic elongation than aperture fixation; the meta-analysis and randomised controlled trial (RCT)-level papers in the search set also suggest clinical outcomes are usually similar despite small biomechanical differences [66][67]. These FE papers also reinforce that graft pretension, radius, and fixation angle can lower relative knee displacement and laxity, which matters directly for suspensory constructs.

Cross-pin fixation is the most convincing case in the FE papers for "optimum stability" at the femoral side. Zainal Abidin et al. [68] used a patient-specific knee model with a 100 N anterior tibial load and compared cross-pin, interference screw, and cortical button fixation; cross-pin came out best in terms of femoral-site stress and strain. That finding fits the broader FE pattern that peak stresses shift toward the fixation aperture or tunnel edge depending on tunnel position and drilling technique [62].

Hybrid fixation is where the biomechanical gains are clearest, but the FE literature is uneven, with most biomechanical papers reporting stronger initial fixation and many clinical studies showing less anteroposterior (AP) laxity. Saltzman et al. [69], for example, modelled a hybrid transtibial drilling technique and found intermediate tunnel length, bending angle, contact force, and graft stress relative to transtibial and anteromedial portal techniques [66].

Staple hybrid fixation or suture-anchor hybrid fixation was sparse in this search.

Across the FE literature, validation is the recurring strength. Models are cross-checked against cadaveric kinematics, robotic loading, or experimental graft force data. Papers report strong agreement with cadaveric measurements, models showing small deviations from experiment across static, quasi-static, and dynamic loading. In more recent years, Open Knee data has been used for validation and then running what-if simulations that link graft pretension, graft radius, and fixation angle to knee laxity, etc. That is the most useful FE theme in this area: the models are best at ranking design choices and identifying failure-prone geometries, not at replacing bench testing for a specific implant.

Chapter 3

Methods

The initial device concept and system dimensions (Chapter 1) were translated into a parametric model in SolidWorks (Section 3.1), which was then imported into Abaqus (Section 3.2) for pre-processing — material properties, contact interactions, loading, and mesh discretisation, detailed in Sections 3.2.1 through 3.2.5, with the mesh convergence study reported in Section 3.2.5. From this common baseline, two simulation configurations were defined: a damage-free two-step analysis combining the insertion and pull out actions, whose results are presented in Chapter 4, and a separate insertion-only analysis incorporating a ductile damage criterion, presented in Section 4.5.

A flowchart of the method process is represented in Figure 3.1.

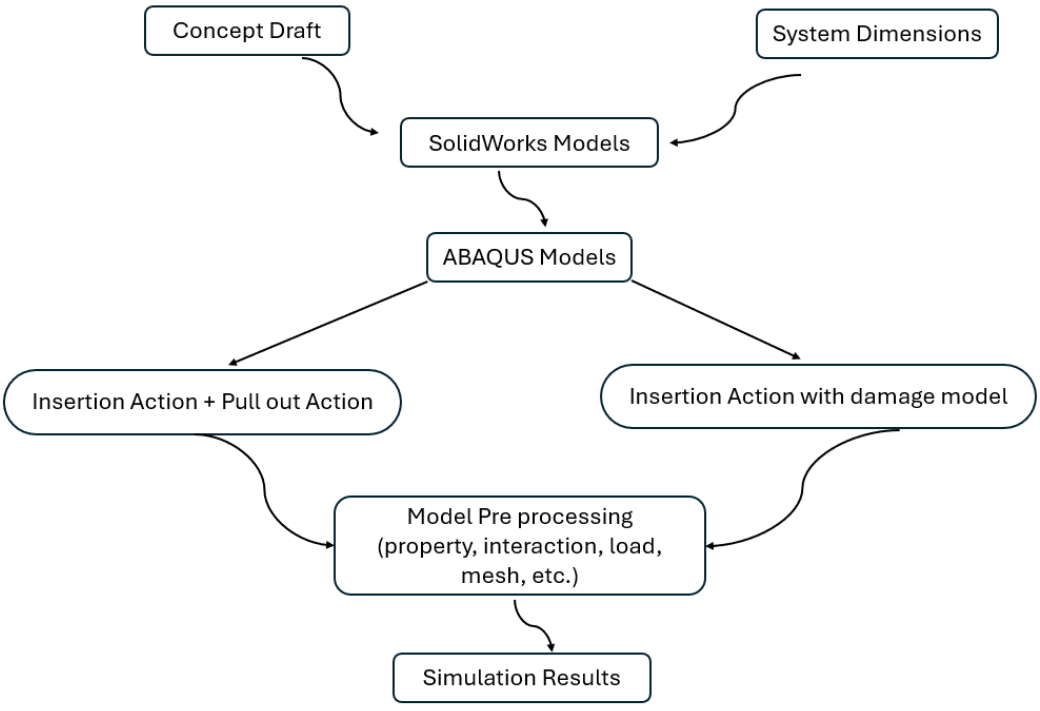


Figure 3.1: Method flowchart

3.1 SolidWorks Environment

A model of the novel fixation device concept was created in SolidWorks, keeping in mind the guidelines provided by Dr. Nuno Camelo and the dimension requirements.

Dr. Nuno's concept tackles the problems of typical interference screw fixation, where the screw insertion counters the tensioning of said ligament, creating laxity.

It achieves this by using a "tunnel" with angled spikes on the wall, allowing insertion, but locking the graft against pull out motions.

The design has to accommodate the new tendon graft, typically a 4 strand hamstring tendon. Studies point to the optimal graft diameter for load bearing and avoiding post surgery complications [70]. According to Alkhalaf et al. (2021), patients with an ACL graft diameter beneath 8 mm were 7.2 times more likely to require a revision [71]. This sets the internal diameter to 9 mm, enough to introduce an 8 mm graft, with a needed tolerance to contain the interaction between the spikes and the ligament graft. These values respect the need for the tunnel coverage ratio to be >70% or the tunnel-tendon gap to be <1 mm, as advised in a tibial ACL reconstruction paper by Flury et al. [72]. Although this focus on the biological consequences of the windshield wiper effect on a bone matrix, it is still relevant in this case, as the fixator will gradually give way to bone material through osteointegration. The wall thickness was set at 1.5 mm, making the external diameter 12 mm.

The spikes were created using a Wrap/Loft function, accounting for 4 layers of 6 angled spikes, totaling 24 spikes.

A thread was applied in the external wall of the fixator. One of the profiles used in this was the SP415-M-8, since it is a wide rounded profile, capable of distributing Load in a bone matrix more evenly, similar to the standard bio-compatible interference screws. Another profile was created, this one with titanium, self tapping screws in mind, with a ISO M thread.

The fixator body can, and in the case of PLLA usage should, incorporate small holes to facilitate osteointegration. Pore or hole diameters below approximately 15 µm tend to promote fibrous rather than osseous tissue ingrowth, while the widely reported optimum for bone ingrowth into porous or fenestrated implants lies between 100 and 400 µm, largely independent of the base material [73]. For discrete holes machined into an otherwise solid implant body, rather than an interconnected porous coating, a finite element parametric study of a bionic cannulated screw for femoral neck fixation found that a hole diameter equal to approximately 10% of the implant's diameter gave the most favourable stress distribution among the values tested (5%, 10%, 15%, and 20%) [74]. Applied to the present device's external diameter of 12 mm, this criterion yields a hole diameter of approximately 1.2 mm.

Finally, a "lip" on the top of the fixator to provide extra load distribution on the dense outer cortical layer of the bone.

Bellow, in Figure 3.2, the LiFix Model is presented (without the osteointegration holes, since these are not load relevant and would cause meshing difficulties, and with SP415-M-8 thread). This was the model used in the finite element method (FEM) analysis.

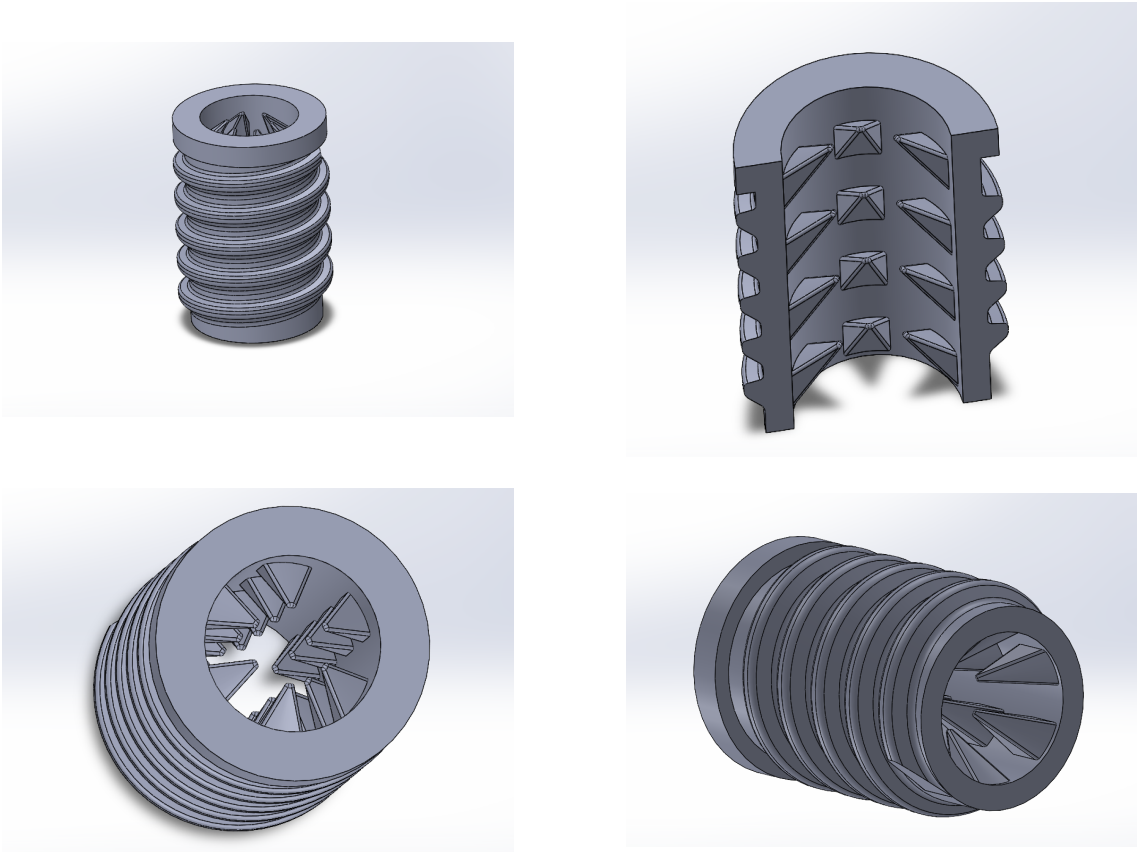


Figure 3.2: LiFix SolidWorks Model

3.2 Abaqus Environment

3.2.1 Tendon geometry

A tendon was created by using ABAQUS sketch functionalities. It is a simple rendition of a tendon graft, consisting of a 8 mm in diameter (validated in the previous section), 70 mm long cylinder, with fillet edges, as it can be seen in Figure 3.3. This length is consistent with the literature [75][76][77][78], and is required to span three key anatomical zones inside the knee:

- Femoral Tunnel (20–25 mm)
- Intra-Articular Space (25–30 mm): The middle portion of the graft spans the open joint space, physically replacing the torn ACL.
- Tibial Tunnel (20–30 mm)

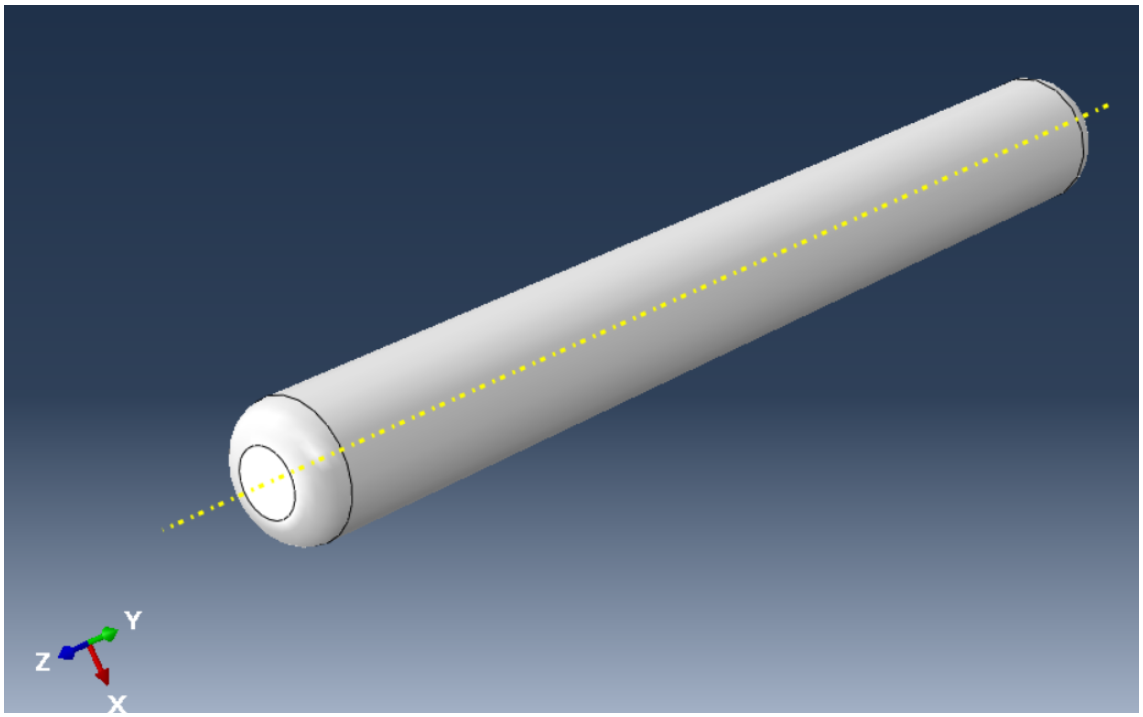


Figure 3.3: Tendon graft geometry

3.2.2 Materials

The tendon was set as a hyperelastic anisotropic Holzapfel material, or Holzapfel-Gasser-Ogden (HGO) model. The parameters are as follows:

- C_{10}: Matrix stiffness
- k_1: Stress-scaling factor for the collagen fibres.
- k_2: Non-linear hardening factor for the collagen fibres.
- κ: Fibre dispersion factor.

The material parameters adopted in the present finite element model were obtained from the study by Sadeqi et al. [79], whose optimised Holzapfel–Gasser–Ogden parameters for the native anterior cruciate ligament (ACL) showed strong agreement with experimental data (correlation coefficient of 0.977). These parameters were applied here as a proxy for the hamstring tendon graft used clinically to replace the native ligament; both are collagenous soft tissues with broadly similar anisotropic, non-linear behaviour, but they are not identical, and no material-specific HGO calibration for hamstring tendon was identified in the literature. The parameter values are summarised in Table 3.1.

Table 3.1: Parameter values for the tendon HGO model

C10 (MPa)	D (MPa^{-1})	k1 (MPa)	k2	κ
1.95	0.00683	22.1	471.255	0.0048

The material density was set to 1.3×10^{-9} t/mm^3 [80][81].

A material orientation was created and applied to simulate the parallel fibres of the tendon on the Z-axis.

The material chosen for the fixator was PLLA, a bio-compatible, bio-absorbable composite of the polylactic acid (PLA) family.

It has a Young Modulus of 2700 MPa and a Poisson ratio of 0.3 [82] [83] [84].

In terms of plastic behaviour, a Stress-Strain Curve was extracted from the material database Ansys EduPack, with the values expressed in Table 3.2.

Table 3.2: PLLA plastic stress–strain curve values (isotropic hardening)

Point	Yield Stress (MPa)	Plastic Strain
1	55	0
2	58.5	0.01
3	62	0.03
4	59	0.05
5	57	0.08

The material density for PLLA was also set to 1.3×10^{-9} t/mm^3 [85][86].

3.2.3 Step and Boundary Conditions

This model is comprised of two Dynamic, Explicit steps, both spanning 0.1 s to ensure computational efficiency. The first one carries out the tendon insertion, while the second one is the pull out. Both steps have adopted a target time increment of 1×10^{-7} s for fixed mass scaling, applied once at the start of each step. This value was selected to keep the analysis computationally tractable given the mesh density required to resolve contact at the spike–graft interface, while remaining small enough that the model's inertial response remained realistic; the ratio of kinetic to internal energy was monitored to confirm the quasi-static validity of this choice. It remained below approximately 3% throughout Step 1 and through the peak-load region of Step 2, up to $t \approx 0.19$ s, confirming the quasi-static validity of the loading rate for the results reported in this thesis. In the final ≈5% of Step 2, the ratio rose to a maximum of approximately 34%; this coincides with complete disengagement of the tendon from the fixator, after which the graft moves as a free body under the residual imposed velocity, with internal energy no longer accumulating. This region lies beyond the peak load, stiffness, and softening behaviour reported in this thesis and does not affect their validity. The results can be seen in the Appendix.

As for boundary conditions (BCs), in both steps the fixator is pinned by the outer thread. In the insertion step, a displacement of 25 mm was applied in one end of the tendon, in order for it to reach the end of the 20 mm fixator (the fixator and the tendon were placed in position in the assembly module). In the pull out step, a velocity BC of 500 mm/s was applied at the other end of the tendon via a smooth-step amplitude, likewise selected for computational efficiency rather than to represent physiological loading rates:

it allows the extraction stroke to be completed within a tractable simulation time in Abaqus/Explicit, at the cost of an instantaneous velocity substantially higher than the 1 mm/s used in the mechanical tests of Chapter 5. The implications of this rate mismatch are discussed in Section 6.5.

3.2.4 Interaction

A Surface to Surface contact (Explicit) was chosen, with the master surface being the whole tendon side and the slave surface being the hole and spikes in the fixator. The mechanical constraint formulation was by the Penalty Method. A value of 0.4 was configured for the friction coefficient of the tangential behaviour. This relatively high value is supported, though not directly validated, by multiple sources addressing different aspects of the problem [87][88][89]. Dohr et al. [87] report frictional behaviour of PLLA against biological tissue in a cochlear implant context; Ramadan et al. [88] characterise the tribological properties of additively manufactured PLA under dry conditions; and Zhao, Amadio, and An [89] report tendon friction against a lubricated biological gliding surface, an interface expected to yield a lower coefficient than the present dry contact.

Normal contact was also set to Hard contact behaviour.

3.2.5 Mesh

Tetrahedral elements were chosen for their flexible geometry, which makes the meshing process possible for highly complex and irregular bodies, such as the fixator. A linear formulation (C3D4, Continuum 3D 4-node tetrahedral) was adopted over the second-order alternatives (C3D10, C3D10M) generally recommended in the Abaqus documentation for accuracy [90]. This choice reflects a deliberate trade-off rather than a default: second-order tetrahedral elements substantially increase both the number of degrees of freedom per element and overall solution cost, a critical constraint given the already considerable runtime of the present model across insertion, extraction, and damage-inclusive variants; where second-order tetrahedra are supported in complex contact scenarios such as the sequential graft–spike interface modelled here, they are further restricted to surface-to-surface contact discretisation [90]. The known consequence of this choice, volumetric locking in the nearly incompressible tendon material, is identified as a candidate for future refinement using C3D10M elements, at least locally at the spike root (Chapter 9).

To identify a suitable mesh for further analyses, a convergence study was conducted by mon- itoring the desired field output, in this case reaction force in the 3-direction (Z-axis) (RF3) in one end of the tendon, across progressively refined meshes. This ensured that the finite element discretisation yields consistent Maximum Pull out Load results while preserving computational efficiency.

It is needed to ensure the entire assembly's convergence and not simply a part. On the other end, there are Part Sets that need special attention. For example, due to the

thread geometry, the lowest seed it meshes to is 1.5 mm, but since it is of virtually no importance to this analysis, this Set was fixed in all simulations to a 1.5 mm mesh through seed edging. On the other hand, the spike set was critical to the interaction spike-tendon, so a finer mesh was used through seed edging, with a 1 to 2.5 ratio comparatively to the global mesh of the fixator and of the tendon. This method ensures the Assembly mesh convergence study is valid.

The results are shown in Table 3.3 and Figure 3.4.

Table 3.3: Mesh convergence study: reaction force (pull out) as a function of mesh refinement

Seed size (global; spikes) [mm]	**Number of elements**	**Reaction force [N]**
5.0; 2.0	14 463	260
3.0; 1.2	21 866	326
2.2; 0.88	30 149	450
2.0; 0.8	36 237	549
1.5; 0.6	51 366	625
1.25; 0.5	72 160	549
1.0; 0.4	103 283	581
0.9; 0.36	132 278	579
0.75; 0.3	187 579	579

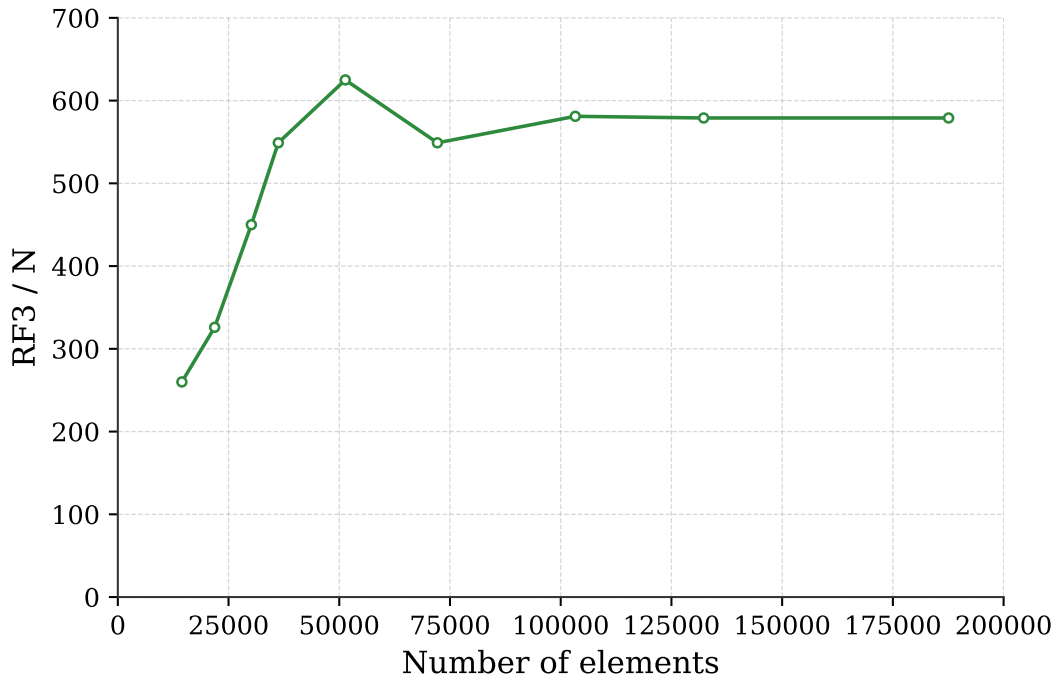


Figure 3.4: Mesh convergence study

The results show convergence at approximately 103 283 elements (and 24 629 nodes), with the error between this and the most refined mesh value being equal to 0.345%. The non-monotonic trend visible between 36 237 and 72 160 elements is attributed to the sharp-edged spike geometry interacting with the explicit contact algorithm: as the mesh is refined, the discretised contact area changes in a non-smooth manner before stabilising, a behaviour previously reported for contact-dominated explicit problems with sharp or pointed features. This plateau was confirmed with a further refinement to 187 579 elements, which produced no change in the reaction force (579 N, identical to the result at 132 278 elements), supporting the mesh density adopted for subsequent analyses.

Bellow, the final mesh is shown in Figure 3.5.

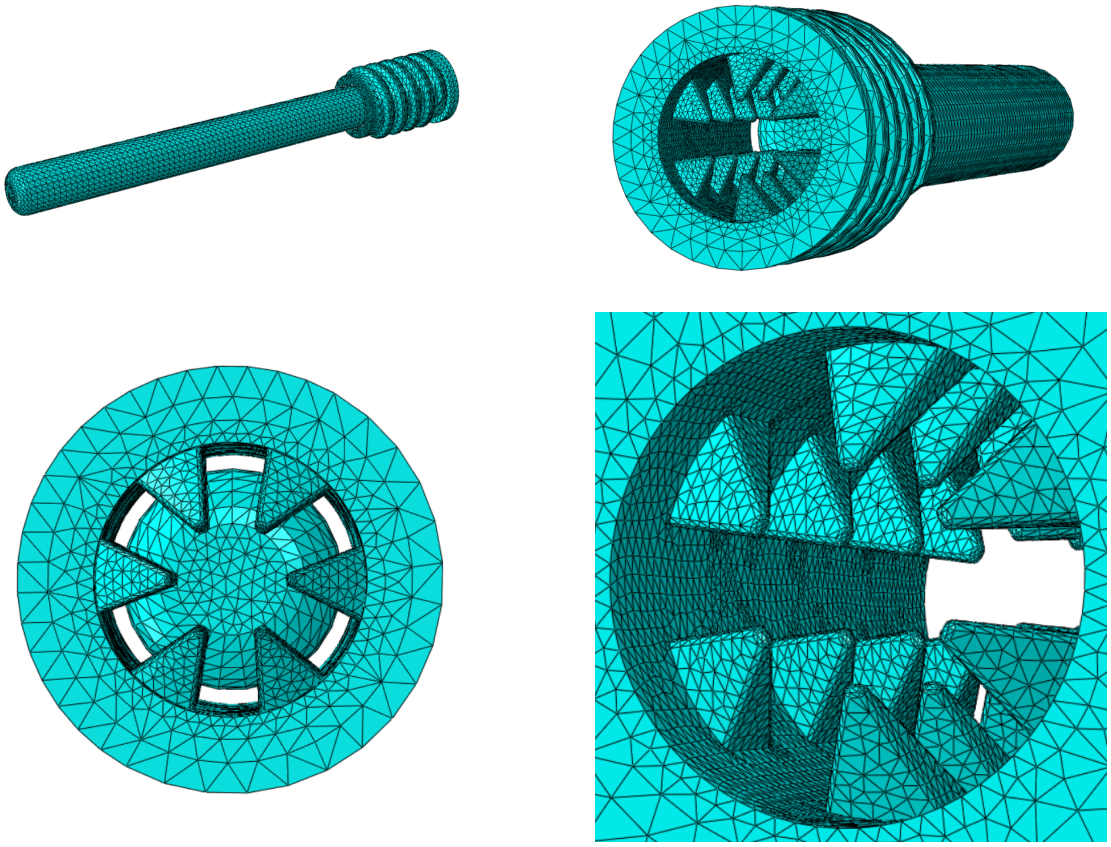


Figure 3.5: Final mesh of the fixator system

Chapter 4

Results

4.1 Insertion results

Figure 4.1 shows the insertion force (RF3, summed over the loaded face node set) as a function of time over Step 1.

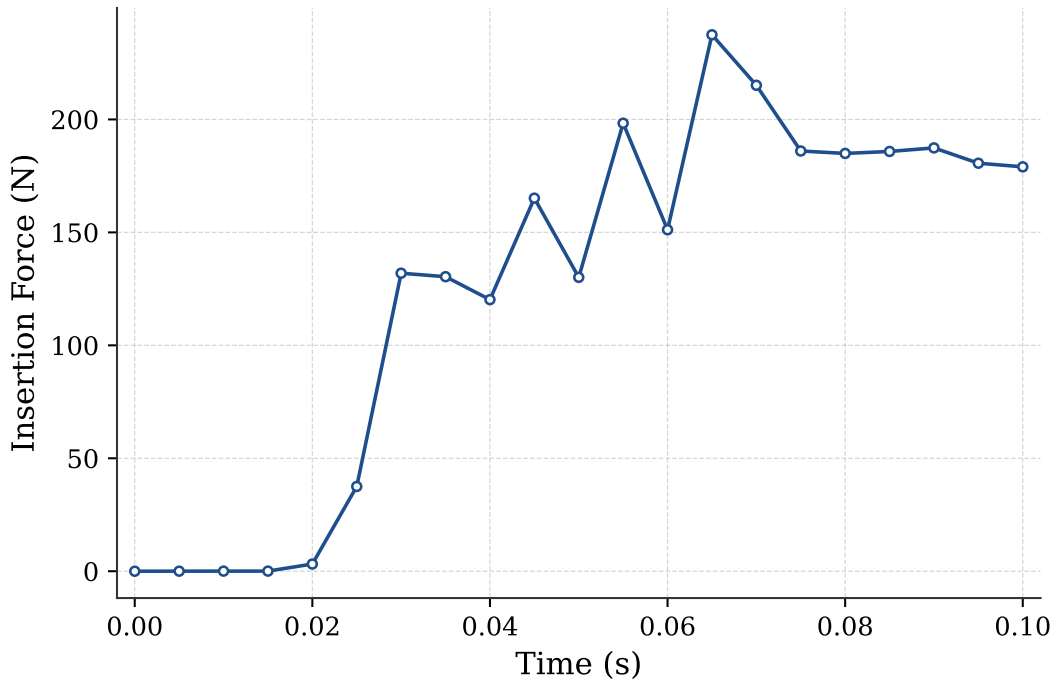


Figure 4.1: Insertion Force as a function of time across Step 1

Figure 4.2 shows the same response as a function of displacement.

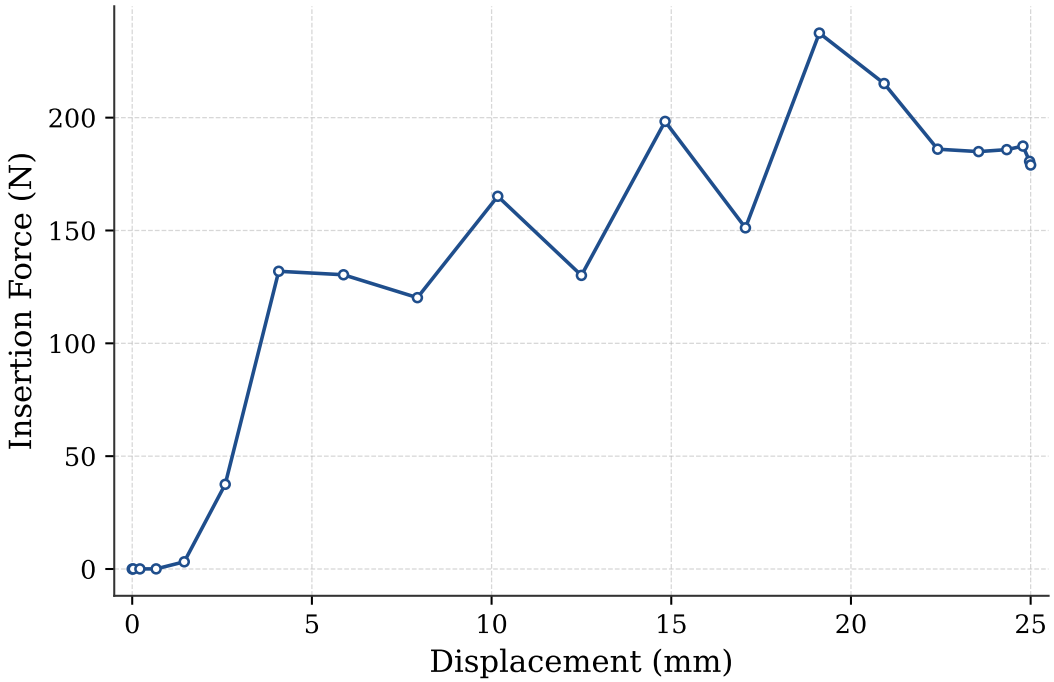


Figure 4.2: Insertion Force as a function of Displacement across Step 1

Three regimes can be distinguished. During the first stage of graft advance, the reaction force remains negligible, as the leading edge of the graft travels through the unobstructed portion of the device lumen. The force then rises steeply to approximately 130 N as the first spike row is engaged. Beyond this point the response rises in a series of discrete peaks, each higher than the last (approximately 132, 165, 198, and 237 N), as the remaining three spike rows engage in sequence, before stabilising in a plateau of approximately 180 N that is maintained until the end of the step.

4.2 Pull out results

Figure 4.3 shows the pull out force–displacement response, across Step 2.

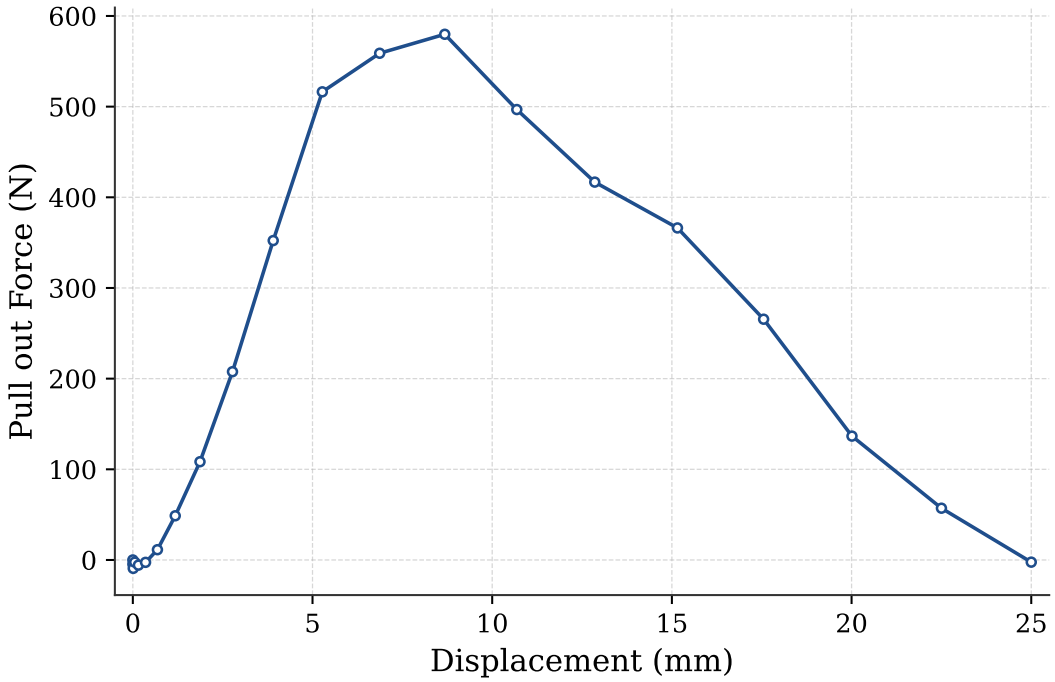


Figure 4.3: Pull out Force as a function of Displacement across Step 2

Figure 4.4 shows the same response as a function of time.

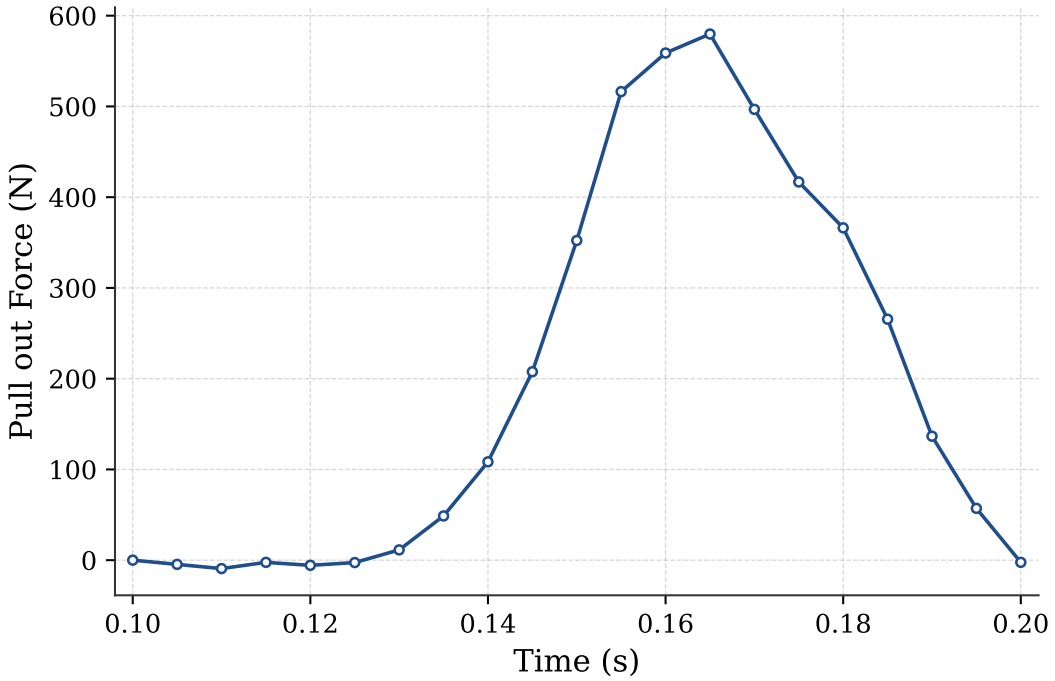


Figure 4.4: Pull out Force as a function of time across Step 2

A toe region extends to approximately 0.5 mm, in which the reaction force remains

below 50 N, followed by a near-linear region up to approximately 4.6 mm, over which a stiffness of approximately 111.8 N/mm was obtained by linear regression over six points sampled within this range ($R^2 = 0.994$; Appendix A). Beyond this point the curve softens progressively, reaching a peak load of 581 N at approximately 8 mm of displacement.

4.3 Fixator Stress and Strain fields

Figure 4.5 and Figure 4.6 show the von Mises stress distribution in the fixator at the end of graft insertion (Step 1, t = 0.1 s) while Figure 4.7 and 4.8 show it at the end of the extraction step (Step 2, t = 0.2 s), respectively.

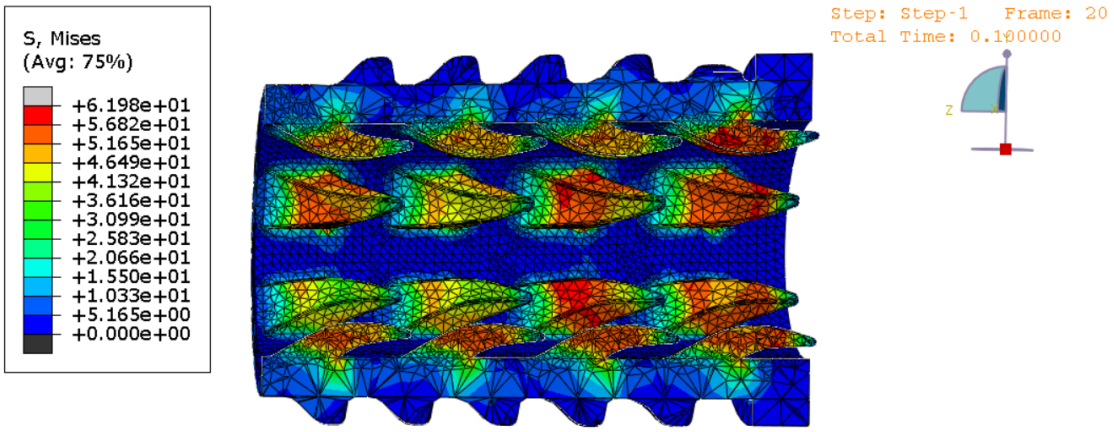


Figure 4.5: Fixator von Mises Stress distribution at t = 0.1 s

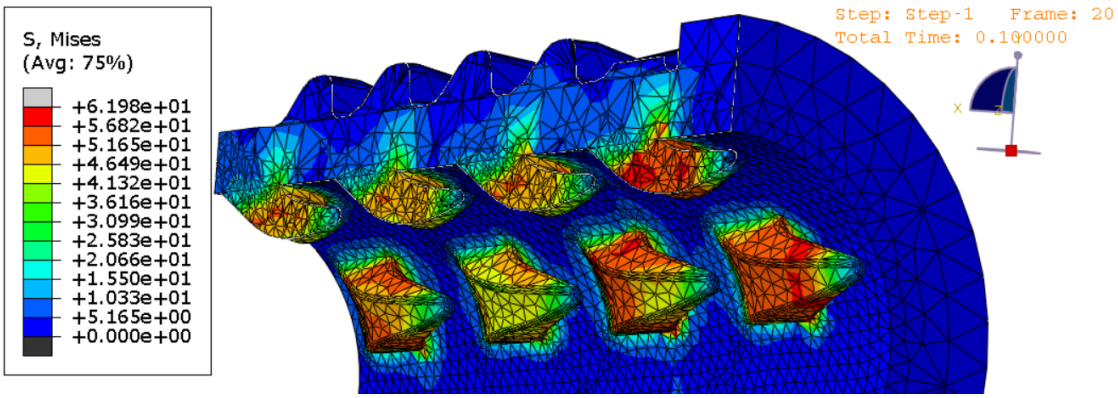


Figure 4.6: Fixator von Mises Stress distribution at t = 0.1 s — spike detail

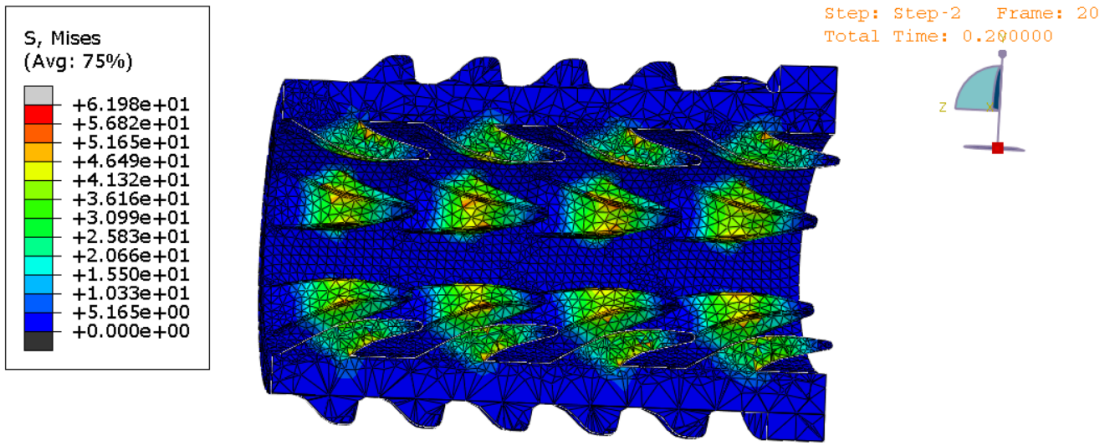


Figure 4.7: Fixator von Mises Stress distribution at t = 0.2 s

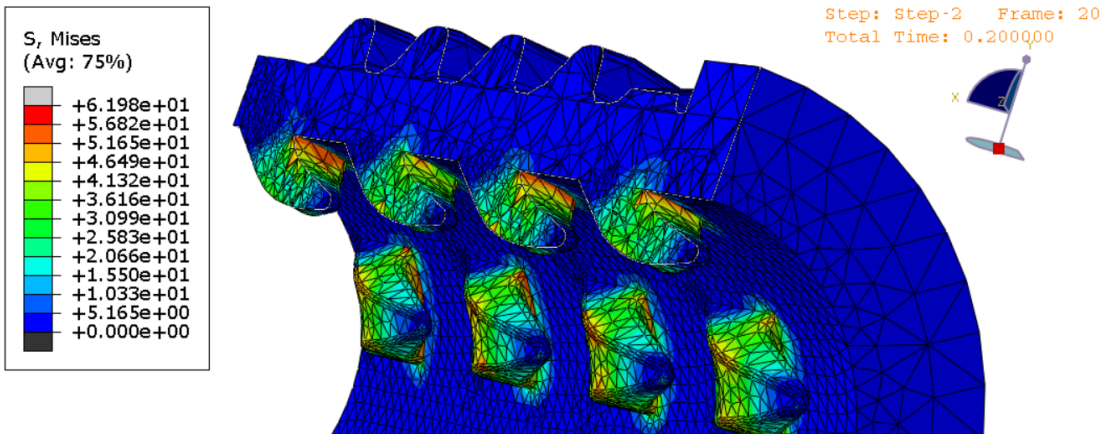


Figure 4.8: Fixator von Mises Stress distribution at t = 0.2 s — spike detail

Figure 4.9 shows plastic strain (PE) Max Principal in the fixator at the end of graft insertion. Peak values of up to approximately 38% seen in the raw field output were confined to isolated elements. Away from this artefact, the field reached a representative value of approximately 28%, distributed through a substantial fraction of the spike thickness rather than confined to a single element, as seen in Figure 4.10. Figure 4.11 shows equivalent plastic strain (PEEQ) at the same instant, reaching approximately 31%.

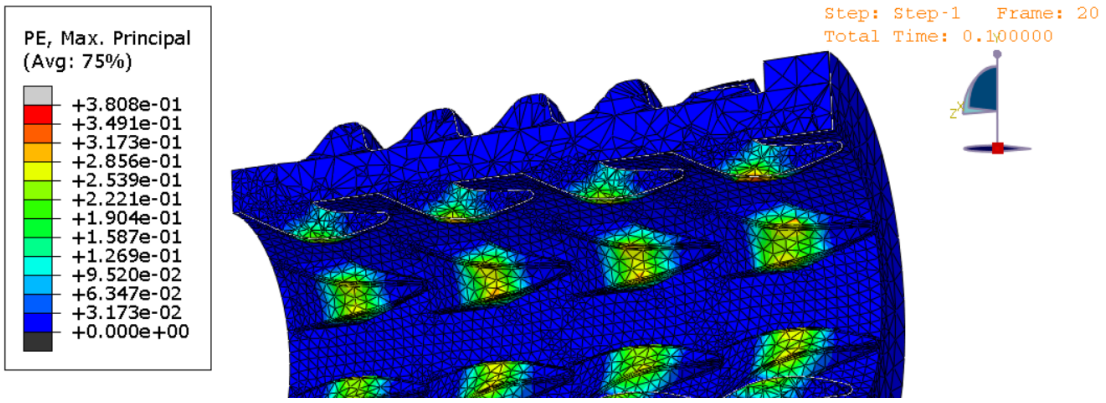


Figure 4.9: Fixator PE Max Principal distribution at t = 0.1 s

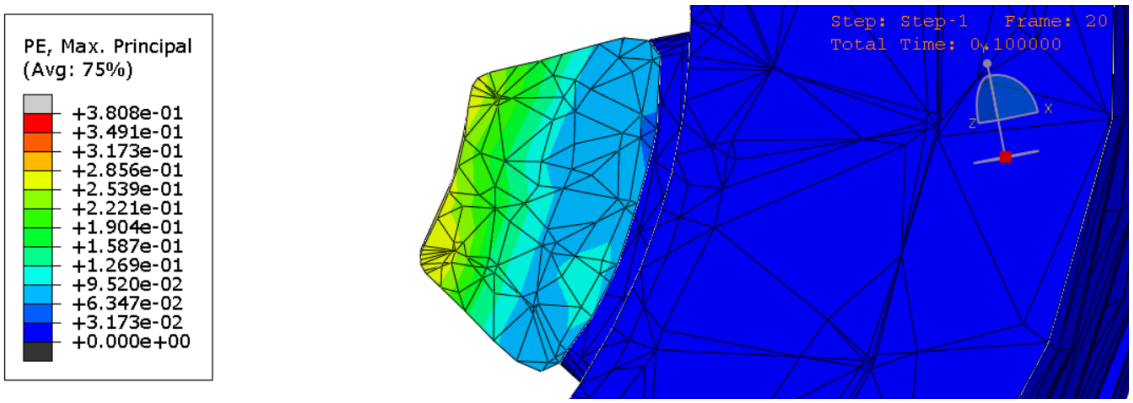


Figure 4.10: Fixator PE Max Principal distribution at t = 0.1 s — Cross sectional detail

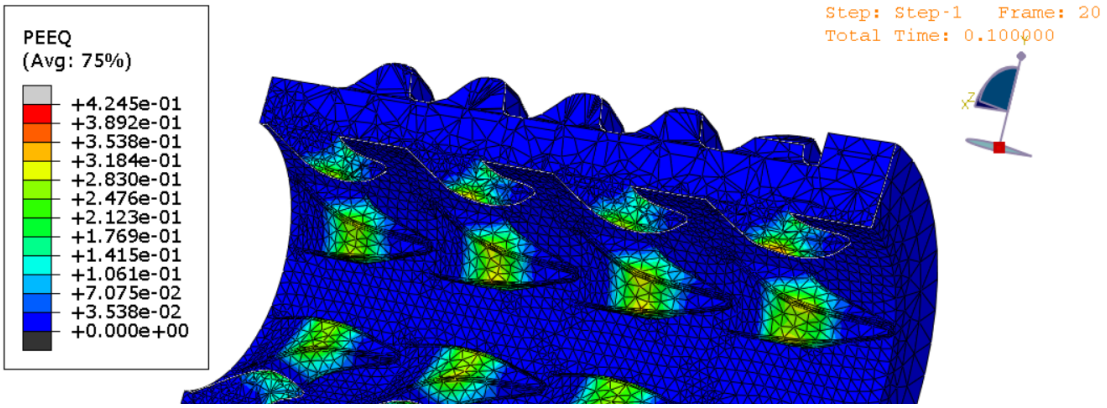


Figure 4.11: Fixator PEEQ distribution at t = 0.1 s

Figure 4.12 and Figure 4.13 show the same two fields at the end of extraction;

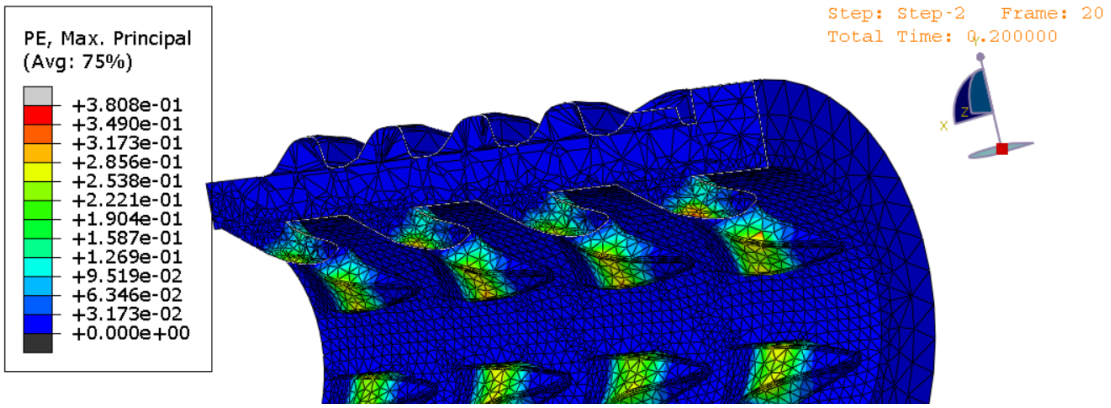


Figure 4.12: Fixator PE Max Principal distribution at t = 0.2 s

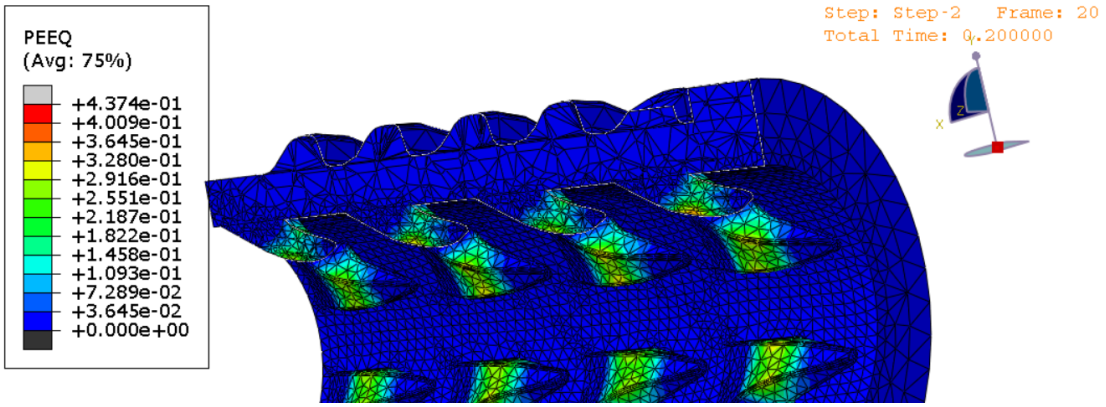


Figure 4.13: Fixator PEEQ distribution at t = 0.2 s

Peak magnitudes are comparable to those at the end of insertion, with the location of the peak shifted along the spike geometry rather than increased in severity.

4.4 Graft focused results

The von Mises stress distribution in the tendon at the frame of peak pull out load (t = 0.165 s) is shown in Figure 4.14.

Figure 4.15 shows the global system's stress field at the same frame.

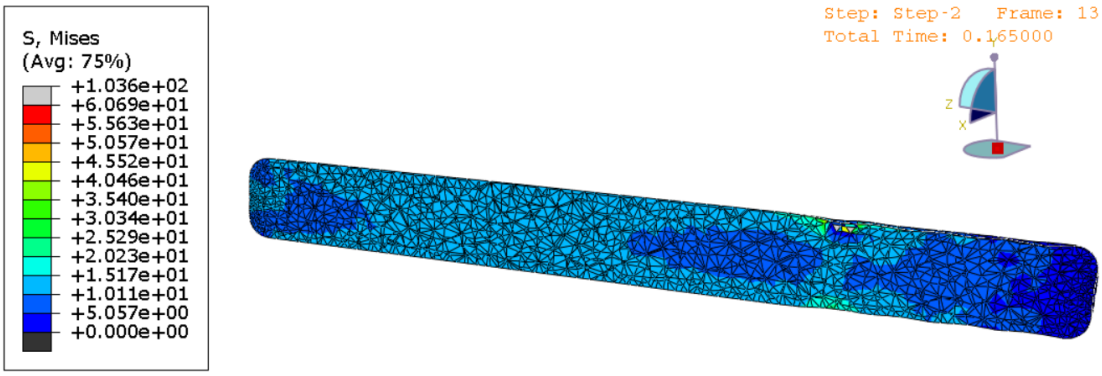


Figure 4.14: Graft von Mises Stress distribution at t = 0.165 s

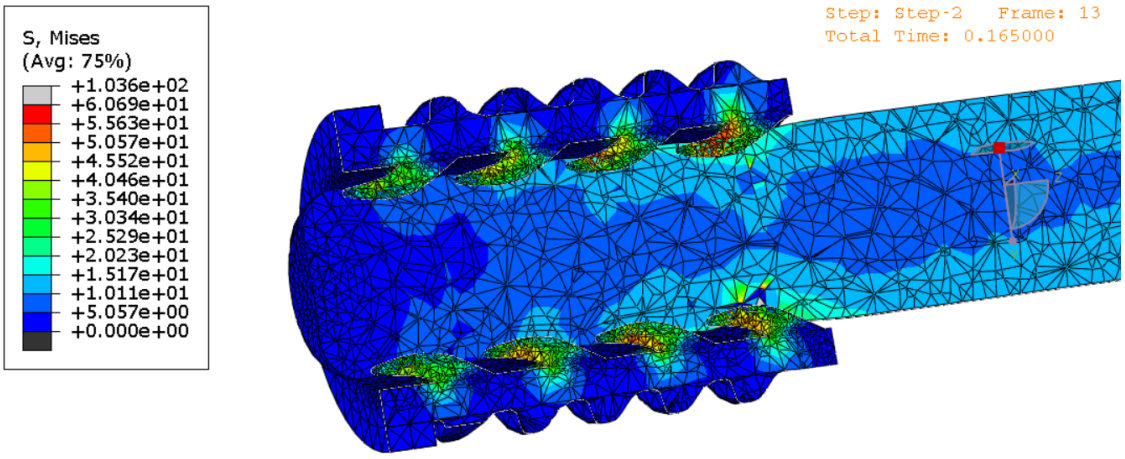


Figure 4.15: Global system von Mises Stress distribution at t = 0.165 s

Stress values are shared across multiple elements in the contact zone, in the range of approximately 27 to 63 MPa; an isolated single-element value of 112.5 MPa at the graft–spike contact boundary was excluded as a mesh artefact.

The tendon displacement in the 3-direction (Z-axis) (U3) was decomposed using three reference nodes at the frame of peak pull out load: the pulled face, a point immediately before the fixator, and a point immediately after it, shown in Figure 4.16.

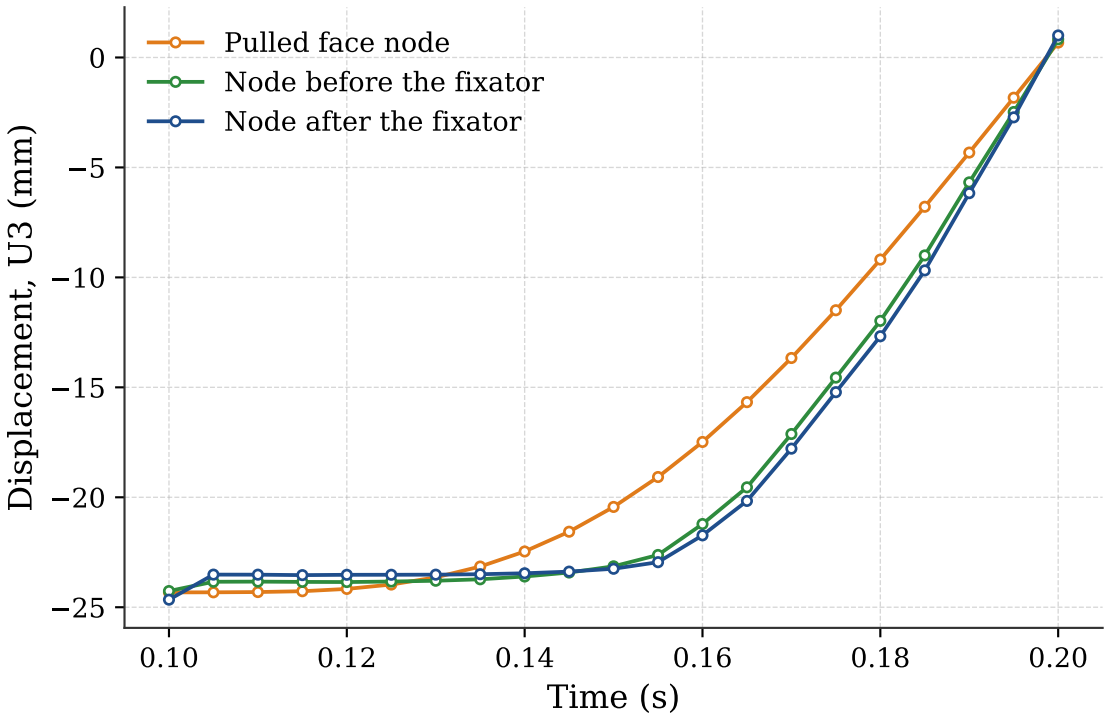


Figure 4.16: Displacement as a function of time across Step 2 of 3 nodes — pulled face node (orange), node before the fixator (green) and node after the fixator (blue)

The graft segment between the pulled face and the point before the fixator showed a cumulative elongation of approximately 4 mm; the point immediately after the fixator displaced by approximately 3 mm specifically during Step 2. These two values do not sum to the total pulled-face displacement at peak load (8 mm), reflecting the different time bases used (cumulative from the start of the analysis for the former, Step-2-specific for the latter) and an unquantified contribution from the approximately 20 mm segment of tendon inside the fixator channel.

4.5 Damage inclusive insertion results

To assess the physical consequence of the plastic strain levels previously reported, which exceed the reported elongation-at-break of PLLA, a ductile damage model was applied to the insertion simulation (Step 1). Damage initiation follows a triaxiality-dependent criterion, after which stiffness degrades progressively according to a displacement-based evolution law, with the affected element removed once the damage variable reaches its maximum permitted value. Two fracture strain values in tension were evaluated: a conservative estimate of 0.03 and an upper-bound estimate of 0.08, spanning the elongation-at-break range reported for PLLA (Table 5.1).

Under both values, fracture of all four spike rows was predicted by the end of Step 1, prior to any extraction load. Figure 4.17 shows the resulting fixator geometry for the

conservative case (fracture strain 0.03); fracture is localised at the tip and mid-height of each spike.

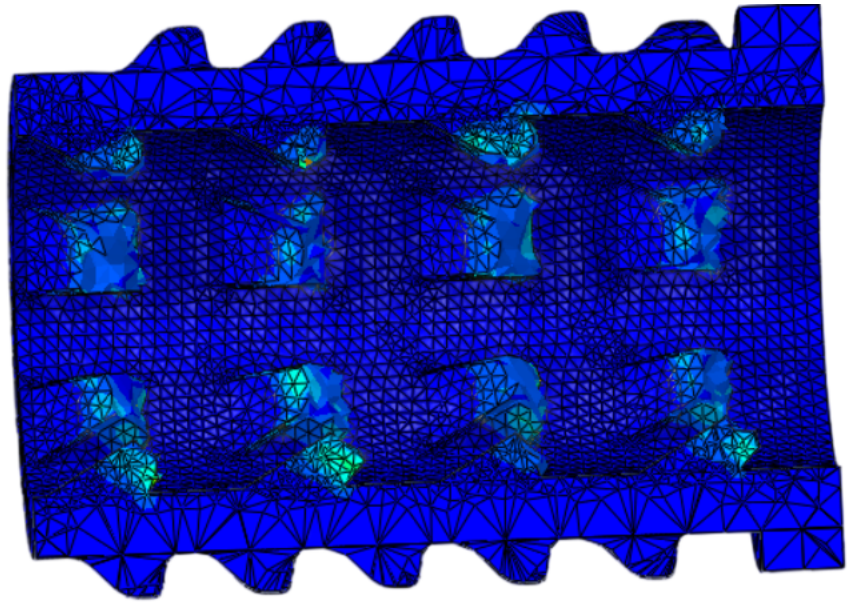


Figure 4.17: resulting fixator geometry for the conservative case (fracture strain 0.03)

Figure 4.18 shows the equivalent result for the upper-bound case with fracture strain set to 0.08;

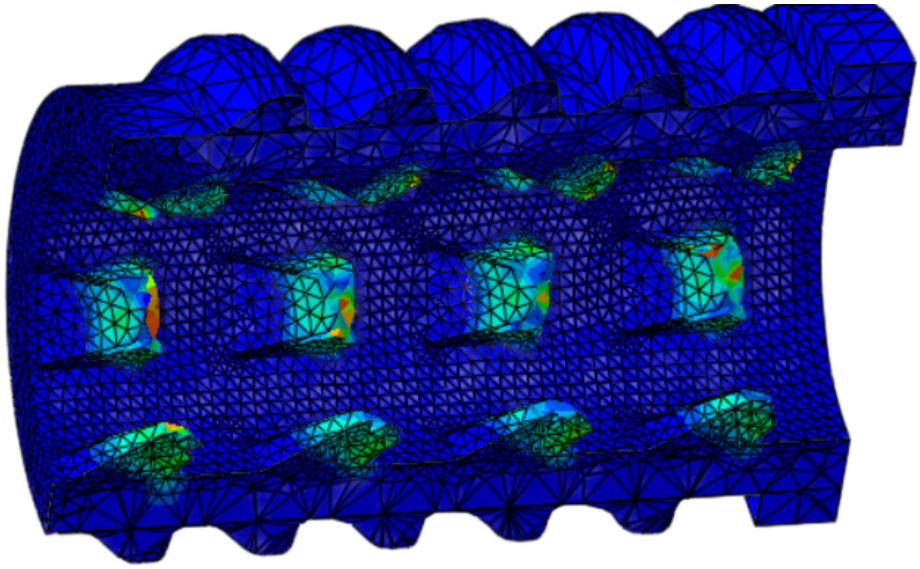


Figure 4.18: resulting fixator geometry for the upper-bound case (fracture strain 0.08)

The fracture location is shifted slightly further along the insertion direction relative to the conservative case, but complete fracture of all spike rows is again obtained.

Insertion force remained close to the damage-free model force.

Chapter 5

Mechanical Test

As an addition to the computational analysis, mechanical test efforts were made to further validate and test the novel fixation device.

5.1 Materials

Three fixation devices were 3D-printed, with previously discussed dimensions, using PLA — a material similar to PLLA — at 100% infill and a layer height of 0.1 mm (Z-axis resolution). The main differences between these materials are expressed in Table 5.1.

Table 5.1: Comprehensive Material Properties: PLA vs PLLA

Property	**PLA**	**PLLA**
Density (g/cm³)	1.21–1.25	1.24–1.30
Young's Modulus (GPa)	0.35–3.83	2.7–4.14
Poisson's Ratio	0.30	0.30
Tensile Strength (MPa)	21–82	15.5–150
Elongation at Break (%)	2.5–7	3.0–10.0
Glass Transition (Tg, °C)	45–60	55–65
Melting Temperature (Tm, °C)	150–177	170–200
Bioabsorbable	Yes (FDA-approved)	Yes (slower degradation)
Biocompatibility	Good (FDA-approved)	Good (FDA-approved)

Two devices were identical, having a SP415 thread, while the third had an ISO M thread (Test 2). This way, thread reliability could also be tested, without compromising the pull out results.

A nylon rope was used to simulate the fresh tendon graft. This rope was made up of twisted strands which were in turn made of twisted yarns, composed of twisted fibres.

The properties of this type of rope are explicit in Table 5.2.

Table 5.2: Nylon rope properties used as graft surrogate

Property	Value
Construction	Twisted/laid, 3-strand*
Nominal diameter	≈8 mm
Material	Nylon 6 (PA6)
Density	1.14–1.15 g/cm^3
Tensile strength	70–85 MPa
Tensile modulus	≈3000 MPa
Elongation at break	20–50%
Typical rope breaking load (8 mm)	8–12 kN†

*Assumed from visual inspection, not confirmed against a manufacturer datasheet. †Reference value for 8 mm nylon 66 rope; not measured for the specific product used. Bulk material values (density through elongation) correspond to generic unreinforced PA6 rather than to the finished rope product.

5.2 Methods

The three devices were prepared by introducing the yarns/fibres individually through the device's hole, carefully not to damage the spike structure. This process was repeated until the assembled rope was ≈8 mm in diameter and filled the entire hole.

Then the fixator was clamped on the base of a *MultiTest-dV Motorised* force tester machine, while the end of the rope coincident to the opposite of the direction of the spikes was clamped to the moving part. Figure 5.1 shows said machine and Figure 5.2 said configuration.



Figure 5.1: MultiTest-dV Motorised force tester machine



Figure 5.2: Experimental tests configuration

A displacement of 1 mm/s was applied and load–displacement graphs were obtained.

5.3 Parameter of interest

The main parameter of interest is Maximum Pull out Load, since the apparatus cannot accurately provide slippage values. This is because the rope configuration is not re-applicable through devices and the obtained displacement value is made up of mostly irrelevant parcels, shown in equation 5.1.

$$\Delta_{\text{total}} = \Delta_{\text{rope,elastic}} + \Delta_{\text{rope,structural}} + \Delta_{\text{fixator}} + \Delta_{\text{clamp}} + \Delta_{\text{machineclamp}} \tag{5.1}$$

where:

Δ_{total} - Total measured displacement.

$\Delta_{\text{rope,elastic}}$ - Elastic deformation of the nylon rope.

$\Delta_{\text{rope,structural}}$ - Structural deformation of the rope due to strand straightening, tightening, and rearrangement.

Δ_{device} - Displacement due to the fixation device (slippage, tooth indentation, and progressive failure).

Δ_{clamp} - Displacement due to clamp compliance or slippage.

Δ_{machine} - Testing machine clamp compliance.

For these reasons, displacement and slippage values obtained from this apparatus are not treated as a reliable measure of device behaviour in this work; the parameter of interest is accordingly restricted to Maximum Pull-out Load, which is unaffected by this decomposition problem.

5.4 Results

Figures 5.3, 5.4, and 5.5 show the load–displacement response obtained for the three tested specimens. All three curves exhibit an initial region of low load followed by a rising, generally non-monotonic segment, before reaching a peak load and subsequently declining.

Test 1 (Figure 5.3) shows small sawtooth oscillation superimposed on the rising portion of the curve up to approximately 18 mm, followed by an abrupt near-vertical load drop and immediate recovery at that displacement. The curve then continues to rise smoothly to a peak load of 580 N at approximately 26 mm, followed by a gradual decline. This decline is consistent with clamp slippage rather than progressive device failure, though whether slippage began before or after the recorded peak could not be established with certainty.

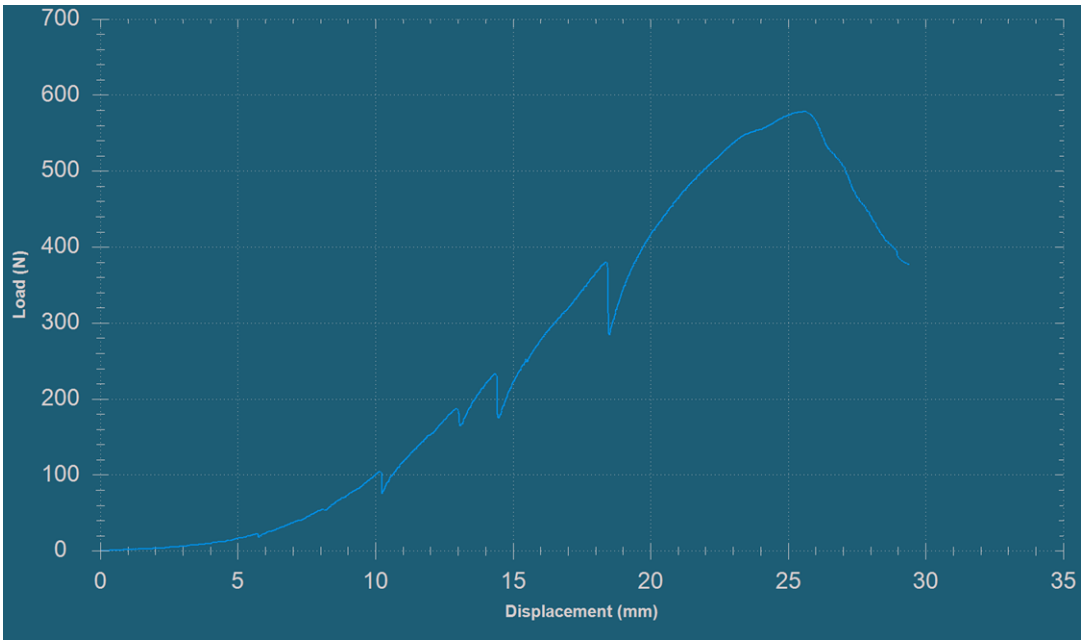


Figure 5.3: Test 1

Test 2 (Figure 5.4) rises more gradually with wavy plateau, followed by an abrupt near-vertical load drop and immediate recovery and subsequent non-monotonic response, reaching a peak load of 755 N.

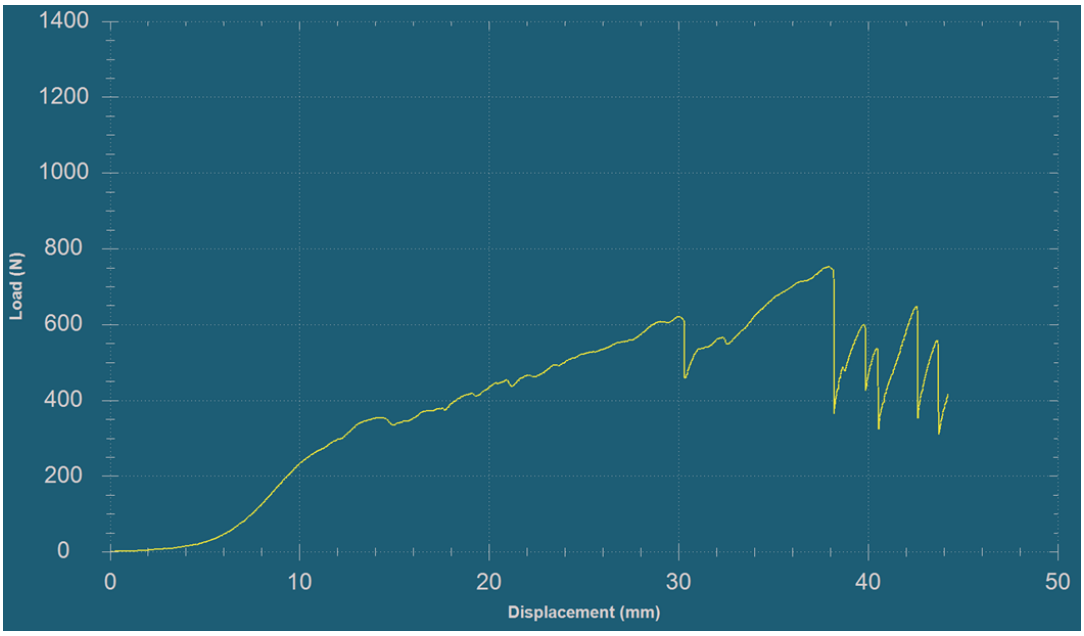


Figure 5.4: Test 2

Test 3 (Figure 5.5) rises with a mild oscillation superimposed throughout, reaching a peak load of 840 N at approximately 38–40 mm, followed by a pronounced sawtooth

sequence of discrete load drops and partial recoveries extending to the end of the recorded displacement range.

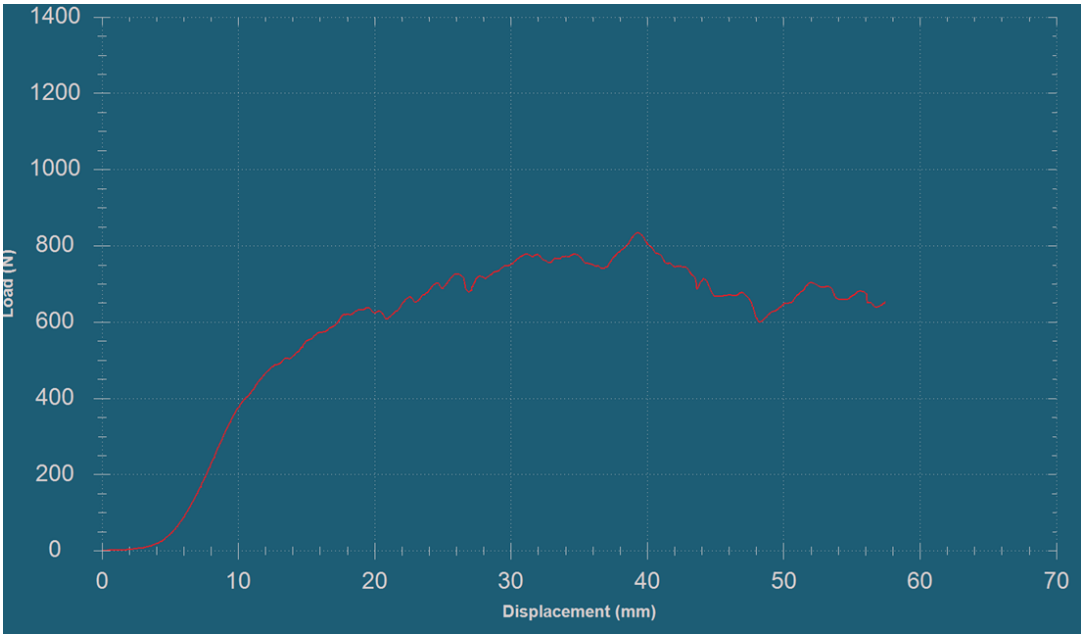


Figure 5.5: Test 3

The descriptive statistics of the three peak values are summarised in Table 5.3.

Table 5.3: Descriptive statistics of the measured values

Values (N)			Mean (N)	Population Standard Deviation (N)
580	755	840	725	≈ 108

Visual inspection of the three prototypes after testing showed the spike tips fractured while the spike bases remained intact, with the severity of fracture varying across the 24 spikes.

Regarding the thread type, the ISO M thread showed more damage, demonstrating the greater suitability of wide threads such as the SP415 in this context.

Chapter 6

Discussion

6.1 Overview

This work set out to evaluate, by finite element analysis, the time-zero fixation performance of LiFix, a novel intra-tunnel ligament fixation device whose anchoring principle relies on angled internal spikes rather than on radial compression of the graft. The numerical model reproduced two sequential events — graft insertion and graft pull out — and was complemented by single-cycle tensile tests on 3D-printed prototypes. This chapter interprets the computed stress, strain and load–displacement fields, confronts the numerical prediction with the experimental measurements, and positions both against the biomechanical benchmarks reported for interference screw fixation.

6.2 Numeric model interpretation

6.2.1 Insertion mechanics

The clinical rationale behind the LiFix concept is the decoupling of graft insertion from graft fixation. In interference screw fixation, the anchoring force is generated by an action — driving a threaded body into the tunnel alongside the graft — that acts against the tension previously applied to the graft, and which is itself a recognised source of graft laceration and of the loss of pretension that manifests clinically as early laxity. The spike-based architecture evaluated here was conceived to invert that relationship: the graft is drawn through the device with the angled spikes deflecting in the direction of travel and is subsequently retained by the same features acting in the opposite direction. Verifying that this asymmetry is real, and quantifying it, is therefore the first question the numerical model must answer.

Insertion response

Three regimes can be identified from Figure 4.1. During the first advance of the graft, the reaction force remains negligible, as the leading edge of the graft travels through the unobstructed portion of the device lumen. The force then rises steeply to approximately 130 N as the first spike row is engaged. Beyond this point the response rises in a series of discrete peaks, each higher than the last (approximately 132, 165, 198, and 237 N), as the remaining three spike rows engage in sequence, before stabilising in a plateau of approximately 180 N that is maintained until the end of the step.

The non-monotonic segment is consistent with the sequential engagement of the four spike rows: each row, upon contact with the advancing graft, produces a local increase in resistance that is partially relieved as the spikes deflect and the graft surface accommodates around them.

The plateau reached once all rows are engaged and the peak force are the mechanically significant features of this curve. Once engaged, each row continues to contribute frictional resistance as the graft slides past it, and this is reflected in the baseline force rising from approximately 130 N, after the first row is engaged, to a plateau of approximately 180 N once all four are. The individual engagement events show comparable costs for the second and third rows (approximately 87 N and 93 N, respectively, measured from the preceding local minimum), rising to approximately 118 N for the fourth row (Figure 4.2); the sustained resistance also increases with the number of engaged rows.

From a surgical standpoint, the transient peaks encountered as each spike row engages — up to approximately 237 N — should be read against reported values for the tension a surgeon can manually apply through a traction suture during ACL graft handling: mean maximal pull forces around 134 N (range 73–182 N), with typical intraoperative loads generally remaining below 90 N [91]. The peak insertion resistance predicted here exceeds even the upper end of what manual traction can reliably deliver; the subsequent plateau of approximately 180 N, though itself close to this upper bound, is reached only after all four rows have engaged and does not represent the maximum resistance a surgeon must overcome during the insertion stroke. This raises a practical caveat: graft insertion in the present concept may require either an insertion aid (e.g. a mechanical puller or a wider traction loop distributing load across more suture material) or a reduction of the insertion resistance through geometric refinement of the spikes, rather than being assumed compatible with unassisted manual passage.

Insertion-Extraction Asymmetry

Taking the insertion plateau as the reference value, and the peak pull out load of 581 N obtained in the subsequent step, the construct exhibits an insertion–extraction asymmetry ratio of approximately 3.2. Referred to the maximum insertion force rather than to the

plateau, the ratio is approximately 2.5. In either case the device requires substantially more force to be extracted than to be assembled, which confirms the directional behaviour that motivated the geometry.

The magnitude of this ratio deserves comment. An asymmetry of approximately three is modest in comparison with what a purely ratcheting mechanism would achieve and reflects the fact that a significant fraction of the insertion resistance is frictional rather than geometric: the coefficient of friction adopted (0.4) applies equally in both directions, and only the interference component of the resistance is direction dependent. The functional argument for the device, however, does not rest only on the magnitude of the ratio, but on the axial insertion action, collinear with the direction of graft tensioning, in contrast to interference screw fixation, whose rotational insertion is a recognised source of pretension loss. The present device therefore removes the insertion–tensioning conflict altogether, independently of the specific value of the asymmetry ratio.

State of the Fixator after Insertion

At the end of the insertion step, before any extraction load had been applied, the plastic strain field within the spikes already reached magnitudes — approximately 28% (PE Max Principal) and 31% (PEEQ) in logarithmic plastic strain — well in excess of the 3–10% engineering elongation at break reported for PLLA (Table 5.1). This comparison is approximate: PE Max Principal is a logarithmic strain measure evaluated at a local point within a bending gradient, whereas elongation at break is an engineering strain averaged over a uniformly loaded tensile specimen at macroscopic failure. It nonetheless motivates a more rigorous, spatially- and triaxiality-resolved assessment, presented below via a ductile damage model with a local, logarithmic-strain fracture criterion — the basis on which the fracture prediction in this section actually rests.

Cross-sectional inspection of this zone (Figure 4.10) showed the strain to be distributed through a substantial fraction of the spike thickness. The field exhibits a diametral gradient, decaying from the traction face towards the neutral axis, consistent with a bending mechanism rather than with a contact-related meshing artefact.

Because the elastic-plastic material model used throughout this work does not include a fracture criterion, it cannot represent the physical consequence of this overload: elements are allowed to accumulate plastic strain without bound, even where the material would, in reality, have already fractured. To assess this consequence directly, a supplementary simulation incorporating a ductile damage model was run, calibrated at the conservative end of the elongation-at-break range reported for PLLA (fracture strain 0.03 in tension). This simulation predicted fracture of all spike tips by the end of the insertion step, localised at the tip and mid-height of each spike. This location coincides with the fracture pattern observed in the mechanically tested prototypes (Section 5.4), where spike tips were found

fractured while the spike bases remained intact — a correspondence that lends geometric, not merely quantitative, support to the failure mechanism predicted by the model.

To assess whether this outcome depended on the specific value adopted for the damage-initiation criterion, the simulation was repeated using the upper end of the reported PLLA ductility range (fracture strain 0.08, more than double the conservative estimate). Complete fracture of all spike rows was again predicted, with the fracture location shifted slightly further along the insertion direction — consistent with a modestly more ductile material sustaining a longer plastic excursion before the local fracture criterion is met, but not preventing failure. The predicted onset of spike fracture during graft insertion is therefore not an artefact of the specific material parameter adopted, but a robust feature of the model across the range of ductility reported for PLLA.

Insertion force was not substantially affected by this loss of geometry in either case, remaining close to the plateau obtained in the damage-free model (Section 6.2.1). Although the two treatments remove spike resistance through different numerical mechanisms — element deletion in the damage model, extreme plastic distortion and loss of effective contact stiffness in the damage-free model — both converge on the same functional outcome: spikes that no longer meaningfully resist the advancing graft. The agreement in insertion force between the two is therefore expected given this shared endpoint, rather than independent evidence of a separate physical mechanism, and the underlying reason insertion force proves insensitive to spike degradation in the first place remains unestablished.

Methodological Contribution

Beyond its role in characterising the present device, the insertion simulation addresses a gap in the finite element literature on ligament fixation. Published models of fixation devices are consistently formulated in the assembled state: the graft and the implant are positioned in their final configuration and the analysis begins from there. Chen et al. [92] modelled the graft–screw interface with a tied constraint, which by construction precludes any relative motion and therefore any representation of either insertion or slippage; Risvas et al. [66] operate at the joint scale, where the fixation interface is assumed ideal; and the component-level studies of Abdullah et al.[12] and Chizari et al. [62], although concerned with the implant itself, likewise begin from the seated configuration.

The consequence is that the assembly manoeuvre — which for the present concept is not incidental but constitutive of the fixation mechanism — has not previously been the object of numerical analysis in this class of device. Simulating it explicitly, with finite-sliding frictional contact and an anisotropic hyperelastic graft, permits the insertion and extraction responses to be obtained from a single continuous model and their ratio to be quantified directly, rather than inferred. It also means that the state of the device at the onset of loading is a computed result rather than an assumption, which is a precondition for interpreting the plastic strains discussed in Section 6.2.1.

6.2.2 Pull out

Extraction response

The extraction step was analysed starting from the geometry obtained at the end of graft insertion in the damage-free model: no elements were removed, but the material had already accumulated substantial plastic strain from the insertion loading (PEEQ approximately 31%, PE Max Principal approximately 28%; Section 6.2.1). This differs from the starting condition of the mechanical tests reported in Chapter 5, where the graft surrogate was threaded through the device fibre by fibre without any simulated insertion load, leaving the specimens mechanically unloaded prior to testing (Section 5.2). Neither condition reproduces the spike fracture predicted by the damage-inclusive insertion model (Section 6.2.1), but they diverge from it differently: the numerical model carries forward the accumulated plastic strain of insertion without representing its ultimate consequence, while the experimental protocol excludes any insertion-induced mechanical state at all. This means that neither result should be read as representative of the device following a traction-based surgical insertion.

The computed load–displacement response is shown in Figure 4.3. Three regimes can be distinguished. A toe region extends to approximately 0.5 mm of displacement, during which the reaction force remains below 50 N; this corresponds to take-up of the graft and re-orientation of collagen fibres within the HGO material model, rather than to engagement of the fixation mechanism itself. Beyond this point the response enters a near-linear regime, over which a stiffness of approximately 111.8 N/mm was obtained by linear regression. Beyond approximately 4.6 mm of displacement the curve softens progressively, with tangent stiffness falling to approximately 18 N/mm, before reaching a peak load of 581 N at approximately 8 mm.

Failure mode and residual capacity

The absence of a sudden load drop after the peak — the curve decays gradually rather than collapsing — indicates progressive rather than catastrophic failure. Within the damage-free model, this reflects the graft sliding past successive spike rows as each disengages in turn, with the remaining rows continuing to carry a fraction of the load. Section 6.2.1 showed that, physically, this progressive character is also consistent with sequential spike tip fracture rather than simultaneous collapse of all anchoring features: mechanically tested prototypes exhibited fractured tips with intact bases, and the corresponding load–displacement curves (Section 5.4) showed discrete drops followed by renewed load increase rather than a single failure event, attributed to the residual spike base retaining compressive engagement with the graft after the tip is lost.

Reconciliation with mechanical testing

The peak load obtained numerically (581 N) falls below the experimental mean (725 ± 108 N, n = 3, individual values 840/580/755 N; Table 5.3) by approximately 20%. Both results share the same idealised starting point — an intact spike geometry — so the divergence is attributable to what occurs from that point onward rather than to the initial condition: in the numerical model, the intact geometry is retained and overloaded well beyond the material's tensile failure strain, whereas in the physical tests spike tips fracture progressively and load is redistributed to the residual bases and to friction along the exposed lumen. This order-of-magnitude agreement should therefore not be interpreted as validation of a shared failure mechanism beyond the shared starting condition.

Several further factors are expected to contribute to the residual gap. The prototypes were printed in PLA rather than PLLA, and the two materials, while comparable, occupy overlapping but distinct property ranges (Table 5.1); the graft surrogate used experimentally was a structured nylon rope, built from twisted yarns and fibres that can interlock mechanically with the spikes, whereas the numerical model represents the graft as a continuous HGO cylinder, which cannot reproduce this interlocking and is likely to understate the load the construct can carry. The loading rate also differs by roughly two orders of magnitude between the two (500 mm/s, smooth-step, in the numerical model against 1 mm/s experimentally), which may be relevant given the rate-sensitivity typical of polymers and soft tissue. BCs differ as well: the numerical model constrains the fixator rigidly through its outer thread, whereas the experimental measurement includes clamp and testing-machine compliance, folded into the total measured displacement (Eq. 5.1) but not separable from it. Finally, with n = 3, the reported standard deviation should be read as descriptive of the observed sample rather than as a basis for inference regarding the true variability of the construct.

6.2.3 Graft response

At the peak pull out load (t = 0.165 in Step 2), U3 was extracted from three reference nodes on the tendon: the pulled face, a point immediately before the fixator, and a point immediately after it (Figure 4.16) The segment between the pulled face and the point before the fixator showed a cumulative elongation of approximately 4 mm; the point immediately after the fixator displaced by approximately 3 mm before failure. These two quantities do not sum to the confirmed total displacement of the pulled face during Step 2 (8 mm), because an unquantified contribution from stretching of the approximately 20 mm tendon segment inside the fixator channel, between the two interface reference points, is not captured by either measurement. The residual is small relative to the total and is not attributed to numerical error.

Referred to a free tendon length of approximately 45 mm, the 4 mm elongation corresponds to an engineering strain of approximately 9%, falling between the two benchmarks

established for the native ACL in Section 2.3 — approximately 15% under normal activity and approximately 30% at tensile failure. These two benchmarks are not directly comparable to one another, as they represent different loading regimes (submaximal physiological loading versus loading to mechanical failure) and were established using different reference-length methodologies; the present comparison is therefore indicative of order of magnitude only. The tendon surrogate therefore operates within a physiologically plausible strain range at the point of device failure, supporting the earlier observation that the construct's overall compliance is dominated by the graft rather than by the fixation device. The 3 mm interface slip is of the same order of magnitude as the cyclic slippage reported for interference screw fixation (2.48–2.82 mm at 50–250 N over 1000 cycles [47][46]), though the present value was obtained under monotonic loading to failure and the two are not directly equivalent.

Stress and contact pressure in the graft

Von Mises stress within the tendon ranged from approximately 27 to 45 MPa during insertion, and from approximately 27 to 63 MPa at the pull out peak, values shared across multiple elements in the contact zone rather than isolated to single-node artefacts. Contact pressure (CPRESS) showed markedly different temporal signatures between the two loading events. During insertion, each spike row produced a brief transient peak as the graft front first engaged it — 19.7–22.6 MPa across the four rows — relaxing within the same frame to a lower steady value of 10.5–15.1 MPa once the row was seated. This row-by-row transient pattern coincides directly with the oscillatory segment of the insertion force curve discussed in Section 6.2.1, providing contact-level confirmation of the sequential row-engagement mechanism inferred there from the global force response alone. During extraction, by contrast, CPRESS built progressively rather than in discrete transients, rising from approximately 14.2 MPa to approximately 17.6 MPa as the load approached its peak — consistent with sustained rather than transient loading of the contact interface at the point of device failure.

Comparable laceration thresholds for the present HGO material representation are not established in the literature, precluding a direct safety assessment. Referred qualitatively to Chen et al. [92] who reported graft stresses of 5.0–59.3 MPa concentrated at the screw–graft junction under a physiological joint-level load of 134 N plus applied moments, the present peak (63 MPa, obtained at a component-level failure load of 581 N) falls within the same order of magnitude despite the substantially higher load level. Combined with the absence of any localised, isolated stress concentration in the graft — the elevated values here are distributed across the contact zone rather than focused at a single junction, as reported for the interference screw case — this indicates the stress magnitudes are of comparable order despite the differences in loading scale and contact formulation between the two models. The absence of a comparable localised concentration in the graft, relative

to interference screw fixation, should be read as a favourable indication rather than as a quantitative safety margin, since the hyperelastic graft representation includes no damage criterion and no validated laceration threshold exists for it (Section 6.5).

6.3 Comparison with the literature

6.3.1 Biomechanical positioning against established fixation methods

The numerical and experimental results obtained for LiFix alongside the biomechanical benchmarks assembled in Table 2.1 for interference screw fixation are expressed in Table 6.1.

Table 6.1: Biomechanical comparison of LiFix (numerical and experimental) against interference screw fixation

	Interference Screw	**LiFix — FE**	**LiFix — Experimental**
Maximum Failure Load	602–632 N [46] [47]	581 N	725 ± 108 N ($n = 3$)
Slippage	2.48–2.82 mm at 50–250 N for 1000 cycles [47] [46]	3 mm (interface only, monotonic)*	not isolable from total displacement (Eq. 5.1)*
Construct Stiffness	101–152 N/mm [46]	≈111.8 N/mm	n/d
Common failure modes	Graft slippage/pullout; laceration	progressive graft slip past disengaging rows (damage-free model)	Sequential spike tip fracture;

*Obtained under monotonic loading to a single failure event; not directly comparable to the cyclic protocols (1000 cycles) underlying the interference screw benchmark.

Figure 6.1 shows the previous comparison between methods of Maximum Failure Load, benchmarking the FE model result and experimental tests results against them.

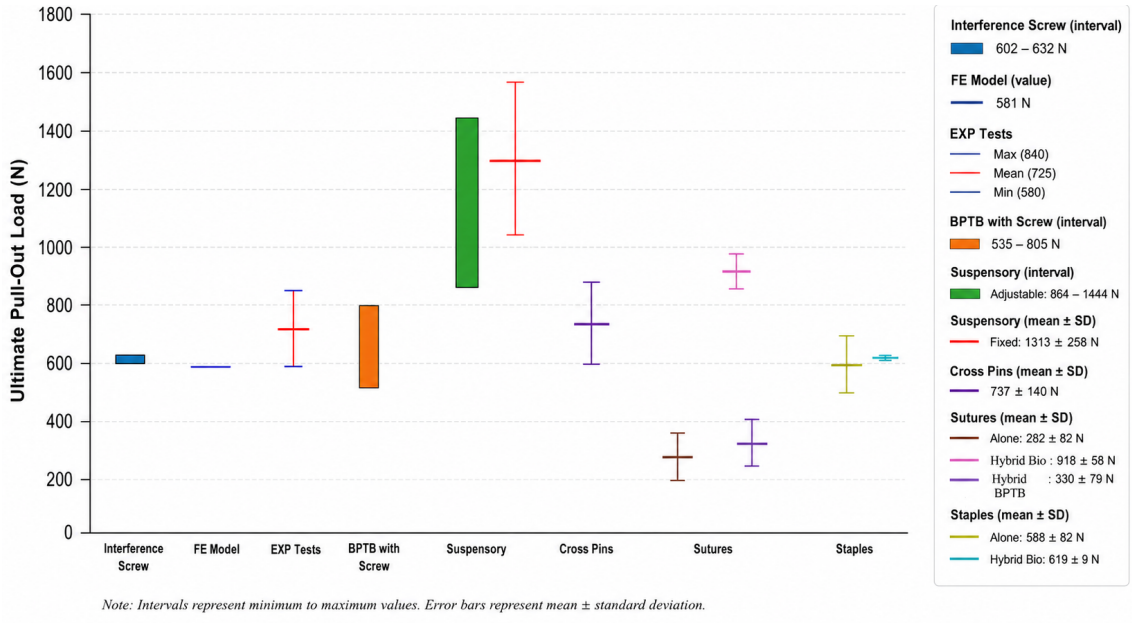


Figure 6.1: FE model and experimental tests benchmark against previous method comparison

Both the numerical peak load (581 N) and the experimental mean (725 N) fall within, or immediately adjacent to, the range reported for interference screw fixation (602–632 N [46][47]; 535–805 N for BPTB with screw [48][49]). The experimental value sits close to the cross-pin benchmark (737 ± 140 N [50]), above staple fixation (588 N [41]), and below both suspensory fixation (864–1444 N [16]) and the native ACL (2195 ± 427 N [59]). The numerically obtained stiffness, approximately 111.8 N/mm, falls at the lower end of the interference screw range (101–152 N/mm [46]) and below the cross-pin and suspensory benchmarks, consistent with the observation (Section 6.2.3) that construct compliance is dominated by the free graft length rather than by the fixation device itself.

Read against the loads associated with daily activity — approximately 169 N during level walking and approximately 445 N when descending stairs, the highest of the activities of daily living reported [93] — both the numerical and experimental peak loads exceed this upper bound by a factor of approximately 1.3 and 1.6 respectively, indicating that the construct can withstand loads above those of common daily activities, though this does not extend to higher-demand activities outside the reported benchmarks.

Two qualifications limit the strength of this positioning. First, no cyclic loading protocol was applied to either the numerical or the experimental construct; the slippage value reported in Table 6.1 is a monotonic, single-pass measurement and is not directly comparable to the 1000–2000 cycle protocols underlying the literature benchmarks, several of which show substantial construct elongation specifically as a consequence of repeated loading rather than of a single pull to failure. Second, both results — as established in Sections 6.2.1 through 6.2.3 — represent the device in an idealised, undamaged state that neither the insertion simulation nor the mechanical test protocol was shown to actually

produce; the values in Table 6.1 should accordingly be read as an upper bound on time-zero performance rather than as a prediction of in-service behaviour.

6.3.2 Methodological comparison with the finite element literature

Beyond this comparative positioning, the present model differs from previously published finite element studies of ACL fixation in ways that bear directly on the interpretation of the results above.

Graft representation and contact formulation. Chen et al. [92], comparing all-inside and interference screw fixation at the joint scale under a tensile load of 134 N and a bending moment of 5 N · m, modelled the ligament as an isotropic linear elastic material and represented the screw–graft interface with a tied constraint. Under these assumptions, the graft stress in their interference screw model fluctuated between 5.0 and 59.3 MPa, concentrated at the screw–graft junction — the location of stress concentration is, by construction of the tied constraint, fixed at this single interface and cannot migrate, nor can any relative sliding or slippage between graft and implant be represented. The present model, by contrast, represents the graft as an anisotropic hyperelastic material with explicit fibre orientation (the HGO formulation, Section 3.2.2) and couples it to the fixator through finite-sliding frictional contact. This allows both the graft stress distribution and the load–displacement response to emerge from the simulation rather than being constrained by the contact formulation, and is the reason the present model can report an interface slip (Section 6.2.3) and a progressive, rather than instantaneous, extraction response (Section 6.2.2) — neither of which a tied-constraint formulation could produce regardless of the material properties used. Notably, despite this more restrictive contact treatment, the graft stress range reported by Chen et al. for interference screw fixation (5.0–59.3 MPa) is of the same order of magnitude as that obtained here (27–63 MPa, Section 6.2.3), which lends plausibility to the present result despite the difference in loading scale (component-level failure load of 581 N against a joint-level physiological load of 134 N).

Location of stress concentration

A further distinction concerns where load-bearing structures are stressed most severely. In the interference screw model of Chen et al., the graft itself carries the highest stress, concentrated at the screw–graft junction — the graft, not the implant, is the component placed most at risk. In the present model, the equivalent concentration occurs in the fixator, at the spike root (Section 6.2.1), while the graft stress remains distributed across the contact zone without a comparable localised peak (Section 6.2.3). This is a favourable indication from a clinical standpoint, though not a validated safety margin (Section 6.5): the implant is a replaceable, purpose-built component, whereas the graft is autologous tissue with no equivalent margin for damage.

Joint-scale versus component-scale modelling

Risvas et al. [66], operating an automated finite-element pipeline validated against Open Knee(s) data, examined how graft pretension, graft radius, and fixation angle influence knee laxity and relative joint displacement, under the assumption of an ideal, non-slipping fixation interface. Their model answers a different question from the one addressed here: given a fixation that holds, how does the surgical construction affect joint kinematics? The present model instead asks whether, and how, the fixation interface itself holds. Neither approach substitutes the other, and the two operate at scales that are in principle composable: the present component-level characterisation of interface stiffness and slip could, in future work, be supplied as a BC to a joint-level model of the kind developed by Risvas et al., in place of the ideal interface such models currently assume.

Component-level benchmarks

Chizari et al. [62], whose CT-based model of tibial interference screw fixation was validated against porcine mechanical testing under both single-cycle and cyclic loading, established the precedent for the combined numerical–experimental strategy adopted in the present work (Chapter 5), though without addressing graft insertion.

Zainal Abidin et al. [68], comparing cross-pin, interference screw, and cortical button fixation under a 100 N anterior tibial load in a patient-specific knee model, found cross-pin fixation to produce the most favourable femoral-side stress and strain distribution among the three methods compared. This is a useful reference point given that the experimental mean obtained here (725 N) falls close to the cross-pin biomechanical benchmark in Table 6.1 (737 ± 140 N [50]): the present device may be understood as approaching cross-pin-level fixation strength without requiring the transverse secondary tunnel, and its associated fracture risk to the femoral condyle (Section 2.2.4), that cross-pin fixation demands.

What the insertion simulation adds

None of the studies discussed above — nor, to the author's knowledge, any other published finite element model of ACL fixation devices — simulates the graft insertion process itself; all begin from the assembled, seated configuration. For interference screw fixation this is a reasonable simplification, since the screw and the graft are placed sequentially rather than through a single continuous motion of the graft relative to the implant. For the present concept, however, insertion and fixation share the same geometric feature — the spikes — and are therefore mechanically coupled in a way that the seated-configuration approach cannot capture. The insertion simulation reported in Section 6.2.1, and its extension to a damage-inclusive treatment, represent the first attempt in this literature to model that coupling explicitly, and the finding that spike fracture may originate during

insertion rather than solely under service loading (Section 6.2.1) is a result this class of model, by construction, could not have produced.

6.3.3 Summary of contribution relative to prior work

Positioned against this literature, the present work contributes: an insertion simulation methodologically absent from prior component- and joint-level FE studies of ligament fixation; an anisotropic hyperelastic graft representation coupled to the implant through frictional contact rather than a tied constraint, enabling slip and progressive failure to emerge as results rather than being precluded by the model formulation; and a combined numerical–damage–experimental characterisation in which the location, though not the load-bearing capacity, of device failure is independently corroborated across three distinct methods (Sections 6.2.1, 6.3). The biomechanical performance achieved — comparable to interference screw and cross-pin fixation at time-zero, under an idealised, undamaged geometry — is offered as a first characterisation of feasibility, not as a claim of superiority over established methods, given the limitations enumerated in Section 6.5.

6.4 Design Implications

The results discussed in Section 6.2 point to a small number of concrete design changes, several of which follow directly from findings that were not anticipated when the geometry was first specified in Section 3.1.

Spike geometry is the priority, not a secondary refinement. Section 6.2.1 established that spike tip fracture is predicted to occur during graft insertion itself, before any extraction load is applied, and that this finding is robust across the full range of ductility reported for PLLA (fracture strain 0.03–0.08). This prioritises the design problem: the spikes must first survive assembly, independently of their performance under service load. The strain field responsible (PE Max Principal reaching approximately 28% at the traction face of the spike, Section 6.2.1) is concentrated in the spike's middle section. A reduction in the spike's height-to-base aspect ratio, would lower the peak bending strain for a given deflection without necessarily reducing the interference depth responsible for the extraction resistance characterised in Section 6.2.2. Because the fixator body and thread remain well below the material's yield stress throughout both loading steps (10 MPa), this refinement has structural margin to draw on without penalising the rest of the geometry.

Insertion resistance may exceed unassisted manual capability. Section 6.2.1 showed the peak transient insertion resistance (approximately 237 N) to clearly exceed the upper end of the tension a surgeon can reliably apply through a traction suture (73–182 N, typically below 90 N in practice [91]); the subsequent plateau (approximately 180 N) remains close to this upper bound as well. This is a practical, not merely biomechanical, constraint: as currently dimensioned, the device may not be insertable by manual traction alone. Two independent design responses follow. The first is geometric — reducing the

number of engaged spike rows, the spike engagement angle, or the friction coefficient at the graft–spike interface (e.g. through surface finish) would lower the plateau directly. The second is instrumental — providing a dedicated insertion aid, such as a mechanical puller or a traction loop distributing load across a wider span of suture material, would remove the constraint without altering the anchoring geometry itself.

Load distribution across spike rows is uneven and merits a graded geometry. The mechanically tested prototypes exhibited variable degrees of fracture across the 24 spikes — some intact, others reduced to a small fraction of their original height (Section 5.4; observation reported in the present discussion, Section 6.2.1) — indicating that the four rows do not share load equally. This is consistent with the row-by-row contact pressure signature obtained numerically during insertion (Section 6.2.3), where each row registers a comparable but not identical transient peak. A geometry in which spike dimensions, angle, or fillet radius vary systematically by row — reinforcing the rows shown to carry disproportionate load, or equalising engagement across all four — would use the available material more efficiently than the present uniform design.

Material substitution is a fallback, not the first lever. Section 6.2.1 established that spike fracture under tension is a robust prediction across the ductility range reported for PLLA. Geometric refinement of the spike root (above) is accordingly the primary lever available within the present material system. Should geometric refinement prove insufficient, the titanium, self-tapping thread variant already modelled in SolidWorks (Section 3.1) remains available as a fallback, at the cost of bioabsorption and with the known drawbacks of permanent metallic hardware — MRI artefact and the frequent need for secondary removal — documented for interference screws in Section 2.2.1.

Structural margin supports the addition of osteointegration features. Stress in the fixator body and thread remained substantially below yield throughout both loading steps (10 MPa), in contrast to the spike roots. This margin supports the introduction of the osteointegration holes anticipated but left undimensioned in Section 3.1, and may also permit a modest reduction in wall thickness, without engaging the same failure mode identified at the spikes.

External diameter remains a design cost to be weighed explicitly. At 12 mm, the device occupies substantially more bone stock than the 8–10 mm typical of interference screw systems (Section 2.2.1). The biomechanical performance characterised in Section 6.3.1 does not offset this cost automatically. It is raised here as a trade-off the design must continue to justify, rather than as a finding this thesis resolves. A reduction in wall thickness, informed by the structural margin noted above, is the most direct route to narrowing this gap without revisiting the internal channel diameter fixed by the graft sizing requirement (Section 3.1).

6.5 Limitations and Assumptions

The interpretation offered throughout this chapter is qualified by a number of modelling and experimental simplifications, several of which were identified in the course of the analysis itself rather than anticipated at the outset. They are presented here broadly in order of expected impact on the conclusions drawn, and, where possible, with an indication of the direction in which each is likely to bias the results.

Idealised starting geometry shared by all validation routes

Section 6.2.1 showed spike tip fracture to be a robust prediction during graft insertion itself, across the full range of PLLA ductility considered. Neither the pull out simulation (Section 6.2.2) nor the mechanical testing protocol (Section 5.2, where specimens were threaded fibre by fibre specifically to avoid damaging the spikes) reproduces this insertion-induced degradation; both characterise the device in an idealised, undamaged state. The extraction performance reported in this thesis — numerically and experimentally — should accordingly be read as an upper bound on time-zero fixation strength rather than as a prediction of the device as it would perform following a traction-based surgical insertion. This is considered the most consequential limitation of the work, precisely because it was not an a priori assumption but a finding that emerged during the analysis.

Absence of a fracture criterion in the primary extraction model

The load–displacement response and the 581 N peak load reported in Section 6.2.2 were obtained from an elastic-plastic material model without damage, in which elements accumulate plastic strain without bound even where the material would, in reality, have already fractured. The order-of-magnitude agreement with the experimental mean (Section 6.2.2) was shown to reflect two distinct load paths converging on a comparable value — an intact, overloaded geometry in the model, against progressive spike fracture with load redistributed to residual bases in the physical specimens — rather than a shared failure mechanism, and should not be over-interpreted as validating the extraction model's internal representation of failure.

Ductile damage parameters estimated, not measured

The supplementary damage simulations (Section 6.2.1) relied on a fracture strain of 0.03–0.08 in tension, derived from the engineering elongation-at-break range reported for bulk PLLA (Table 5.1) rather than measured for the specific additively manufactured material used in this device. The shear and compression branches of the triaxiality-dependent initiation criterion (0.06 and 0.35 respectively) are weaker still: the shear value is an order-of-magnitude extrapolation from the tensile datum, and the compression value

is supported only qualitatively, by the general trend toward greater ductility under compressive triaxiality reported for semicrystalline PLLA elsewhere in the literature, not by a value specific to this material or process. The damage evolution parameter (displacement at failure) was likewise estimated rather than calibrated. The robustness check performed — repeating the tensile initiation value at the upper end of the reported ductility range — supports the qualitative conclusion that spike fracture occurs regardless of the specific value chosen, but does not extend to the quantitative load or strain at which it occurs.

Bone is not represented

The fixator is constrained by its outer thread as an idealised rigid anchorage, representing neither the compliance nor the failure modes of the surrounding bone — trabecular yielding, thread pull-out, or tunnel wall fracture — identified in Chapter 2 as relevant failure mechanisms for other fixation methods. This simplification isolates the graft–fixator interface for characterisation.

Loading is quasi-static in intent but not uniformly so in practice

Both steps use a Dynamic Explicit formulation with a smooth-step velocity amplitude and target time increment of 1×10^{-7} s for fixed mass scaling (Section 3.2.3), producing an instantaneous velocity that varies continuously through each step and peaks at approximately 500 mm/s in extraction — two to three orders of magnitude above the 1 mm/s used in the mechanical tests of Chapter 5. Neither the PLLA plasticity model nor the tendon's HGO formulation includes rate dependence, so any true viscoelastic or rate-sensitive response of either material is absent from the simulation, and the numerical and experimental results are not obtained under equivalent loading rates.

The graft is a simplified surrogate

The tendon is represented as a single homogeneous, anisotropic hyperelastic cylinder, rather than the multi-strand hamstring construct it represents; no preconditioning cycles were applied, and the HGO formulation is hyperelastic rather than viscoelastic. The material cannot reproduce the mechanical interlocking between individual strands and the spikes that is possible with a structured surrogate. The constitutive parameters themselves were calibrated against native ACL tissue (Section 3.2.2) rather than against hamstring tendon specifically, since no equivalent HGO calibration for hamstring tendon was identified in the literature; this is a further approximation, distinct from the geometric simplification described above.

Friction coefficient not measured for this system

A value of 0.4 was adopted from the literature on additively manufactured polymer surfaces, applied identically in both loading directions and without a sensitivity study. Any anisotropy introduced by the printed layer structure of the physical spikes is not represented.

No validated laceration threshold for the graft material representation

The stress and contact pressure values reported for the tendon (Section 6.2.3) were compared to the literature only in qualitative, order-of-magnitude terms; no criterion establishing a safe stress or pressure limit for the HGO formulation is available, and the absence of a comparable localised concentration relative to interference screw fixation should be read as a favourable indication rather than as a quantitative safety margin.

Local field convergence not separately verified

The mesh convergence study (Section 3.2.5) was performed on a global output (the pull out reaction force), which was confirmed to plateau at 132 278 elements and remained unchanged upon further refinement to 187 579 elements — a substantial degree of refinement given the computational resources available for this work. This does not guarantee equivalent convergence of the local strain fields (PEEQ, PE Max Principal) used to support the fracture interpretation in Sections 6.2.1 and 6.2.3, as localised plastic strain concentrations can in principle exhibit different mesh sensitivity than a global reaction force. Single-element or small-cluster outliers, defined here as no more than five elements exhibiting values substantially higher than their immediate neighbours, were identified by direct inspection and excluded from all reported values on a case-by-case basis, applying this criterion consistently across both the original and refined geometries (Chapters 4 and 7). A formal, quantitative mesh sensitivity study at the spike mid height or tip was not conducted.

Experimental validation limitations

With three specimens, the reported standard deviation (Table 5.3) is descriptive of the observed sample and does not support statistical inference. The prototypes were printed in PLA rather than PLLA; the two materials occupy overlapping but distinct property ranges (Table 5.1). The graft surrogate was a structured nylon rope, built from twisted yarns and fibres capable of mechanical interlocking with the spikes, in contrast to the continuous cylinder used numerically. Clamp and testing-machine compliance are folded into the total measured displacement (Eq. 5.1) and could not be separated from the device's own contribution. Additionally, the substantially lower peak load recorded for Test 1 (580 N, against 755 N and 840 N for the other two specimens) coincided with

visible clamp slippage; it cannot be established with certainty whether this affected the recorded peak itself or only the post-peak decline, introducing an additional source of uncertainty into the reported mean and standard deviation (Table 5.3).

No cyclic loading

All results represent a single monotonic loading history to failure; the slippage values compared against the cyclic literature benchmarks in Section 6.3.1 are not obtained under equivalent conditions and should be read as indicative of order of magnitude only, not as evidence of long-term construct stability under repeated loading.

Chained insertion-to-extraction simulation not achieved

Attempts to continue the damage-inclusive insertion model (Section 6.2.1) directly into the extraction step were limited by numerical instability associated with severe element distortion following spike fracture, which collapsed the stable time increment. Resolving this coupling is identified as a priority extension of the present model.

Chapter 7

Preliminary Spike Geometry Refinement

7.1 Design Changes

The spikes are the priority target for geometric refinement. Both the elastic-plastic and damage-inclusive models in Section 6.2.1 located the responsible plastic strain at the tip and mid-height of the spike and the present refinement targets that region. The spikes now protrude less into the fixator lumen than in the original design, reducing the deflection demanded of them as the graft advances. Moreover, the spike's leading engagement face, previously flat, was curved, so that contact area develops as the graft advances past each row rather than engaging almost instantaneously. This also produced a spike tip that is slightly wider and less pointed than before. The mesh density used for the original geometry (Section 3.2.5) was carried over to this model rather than reconverged from scratch; this simplification is discussed in Section 7.3. Figure 7.1 and Figure 7.2 show these alterations.

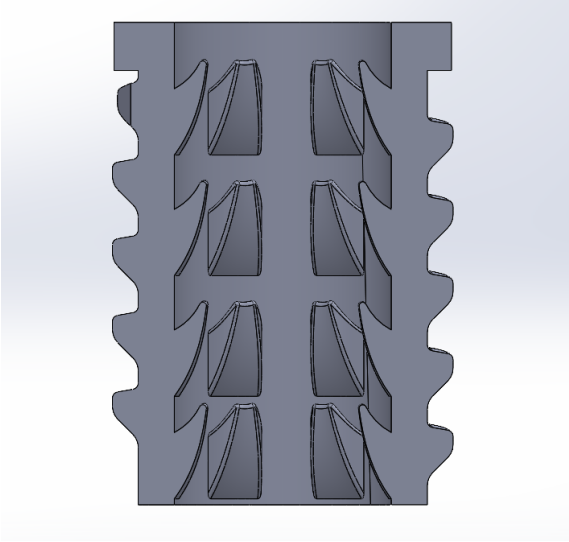


Figure 7.1: Refined spike geometry, showing the curved engagement face across all four spike rows

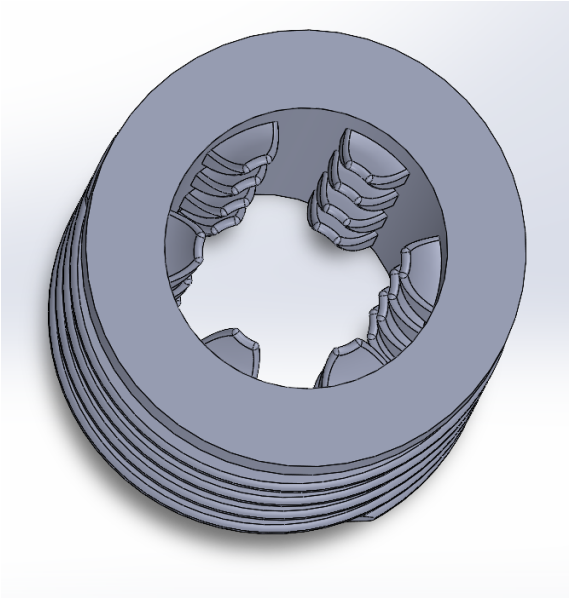


Figure 7.2: Refined spike geometry, showing the wider spike tip and reduced spike protrusion

7.2 Results

Both PEEQ and PE Max Principal at the end of the insertion step (Step 1, t = 0.1 s) were substantially lower in the refined geometry than in the original: peak values of the order of 30–38% seen in the raw field output were confined to isolated elements at the graft–spike contact boundary, confirmed by cross-sectional inspection of the affected spikes, consistent with the mesh artefacts identified elsewhere in this thesis (Sections 6.2.1, 6.2.3). Away

from these artefacts, both fields remained below approximately 5% throughout the spike geometry.

The refined geometry was also evaluated under the damage-inclusive insertion model described in Section 6.2.1, using the same fracture strain values (0.03 and 0.08 in tension) established there. Unlike the original geometry, where both values predicted complete fracture of all spike rows, neither value produced spike fracture in the refined geometry: no elements reached the damage-initiation criterion during insertion, consistent with the low, artefact-free strain field described above.

Figure 7.3 shows the pull out force response as a function of time; a peak load of 650 N was reached at $t \approx 0.17$ s, exceeding the 581 N obtained for the original geometry.

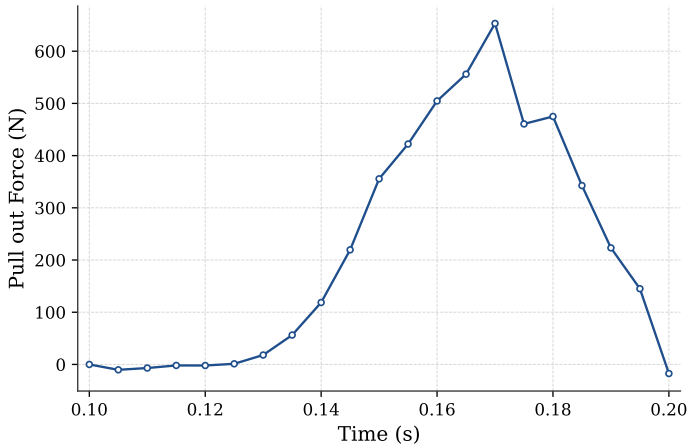


Figure 7.3: Refined geometry: pull out force as a function of time

Figure 7.4 shows PE Max Principal in the refined geometry at the end of the insertion step (Step 1, t = 0.1 s), for direct comparison with the original geometry (Section 4.3). The field remains below approximately 5% across the spike geometry, away from isolated single-element artefacts at the graft–spike contact boundary consistent with those identified elsewhere in this thesis (Sections 6.2.1, 6.2.3).

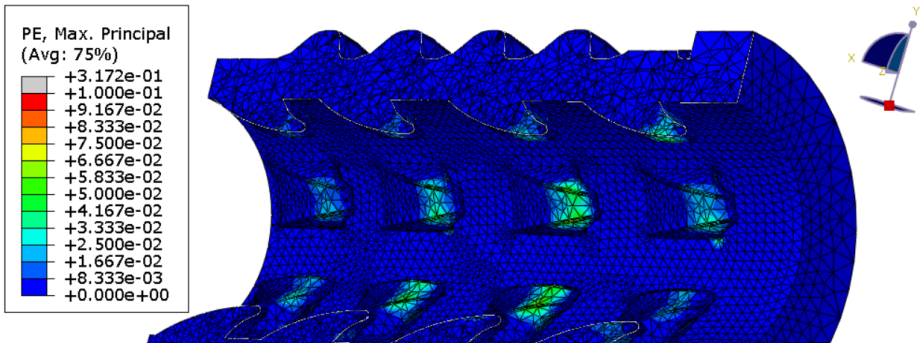


Figure 7.4: Refined geometry: PE Max Principal at the end of insertion (Step 1, t = 0.1 s), cross-sectional detail

Figure 7.5 shows the resulting spike geometry under the damage-inclusive insertion model (Section 6.2.1, fracture strain 0.08 in tension); no elements reached the damage-initiation criterion, and the geometry remains intact.

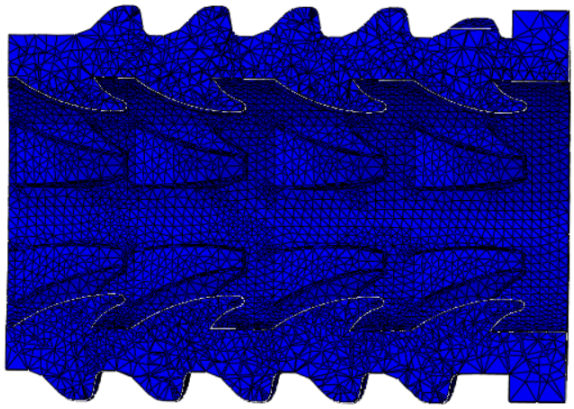


Figure 7.5: Refined geometry under the damage-inclusive insertion model (fracture strain 0.08): spike geometry remains intact

Table 7.1 compares the finite element response of the original and refined geometries.

Table 7.1: Comparison between the original and refined spike geometries

	Original	**Refined**
Pull out peak load	581 N	650 N
PEEQ, end of insertion (Step 1)	≈31%	≈5%
PE Max Principal, end of insertion (Step 1)	≈28%	≈5%
Damage-inclusive insertion outcome	complete fracture, all rows	no fracture predicted

7.3 Discussion

The reduction in insertion-phase plastic strain observed for the refined geometry is consistent with the failure mechanism established in Section 6.2.1, where spike fracture was attributed to bending-dominated deformation at the tip and mid-height of the spike. Reducing spike protrusion shortens the effective lever arm over which this bending occurs, while curving the engagement face distributes contact load progressively rather than concentrating it at a single, near-instantaneous point of contact. Together, these changes appear to have shifted the spike's response away from the bending-dominated regime responsible for the fracture behaviour characterised throughout this thesis, rather than merely reducing its severity.

This result does not alter the characterisation of the original geometry presented in Chapter 6: spike fracture during insertion remains a robust prediction for that design,

across the ductility range considered for PLLA. What the present chapter adds is a preliminary, concrete demonstration that the design lever identified as the priority in Section 6.4 — refinement of the spike itself — is capable of addressing this failure mode, while simultaneously improving extraction resistance rather than trading it away. The pull out response of the refined geometry (Figure 7.3) retains the progressive, non-catastrophic failure character described in Section 6.2.2, with load recovering after discrete drops near the peak rather than collapsing outright.

This chapter's findings are preliminary in scope and carry limitations distinct from those enumerated in Section 6.5. The mesh density validated for the original geometry (Section 3.2.5) was retained here rather than independently reconverged, and local mesh sensitivity at the refined spike geometry was not separately verified. The damage-initiation parameters applied (Section 6.2.1) were likewise reused without re-evaluating the characteristic element length at the refined spike geometry, which the displacement-based damage evolution law depends on. No attempt was made to couple this insertion-phase result to a damage-inclusive extraction simulation, for the same numerical reasons discussed in Section 6.5, and the refined geometry has not been evaluated experimentally. Only one refinement was tested; this chapter reports a single design point rather than a systematic exploration of the design space, and the true sensitivity of the outcome to the specific magnitude of each geometric change remains unknown.

Chapter 8

Conclusion

This thesis set out to evaluate the mechanical performance of LiFix, a novel intra-tunnel ligament fixation device whose anchoring principle relies on angled internal spikes rather than on the radial compression used by interference screws. The evaluation combined finite element analysis — including, distinctively, an explicit simulation of graft insertion — with mechanical testing of 3D-printed prototypes, and was pursued through four specific objectives stated in Section 1.2. The findings are summarised below against each in turn.

The insertion force was found to stabilise in a plateau of approximately 180 N, with transient peaks of up to approximately 237 N as the four spike rows engage sequentially — a mechanism confirmed independently at the level of the global force response and of the local contact pressure signature (Sections 6.2.1, 6.2.3). This resistance lies at or above the upper end of what a surgeon can reliably apply through manual traction, a practical constraint on the current geometry rather than a purely biomechanical one. More significantly, the central finding of this work emerged from this stage of the analysis rather than from extraction: plastic strain within the spikes, reaching approximately 28% at the spike tip and mid-height, was found to substantially exceed the engineering elongation-at-break reported for PLLA — an approximate but consistent comparison, given the different strain measures and loading conditions involved — already at the end of insertion, before any extraction load is applied. A supplementary damage-inclusive simulation, robust across the full range of ductility reported for the material, predicted fracture of all four spike rows during insertion itself. This is a genuine limitation of the present geometry, not an artefact of the numerical treatment. Fracture at the tip and mid-height, as predicted by the damage-inclusive model and observed in the mechanically tested prototypes, leaves the spike base largely intact; the pull out tests show that this residual base retains meaningful compressive engagement with the graft, with load recovering after each fracture event rather than collapsing. Whether the same holds in aggregate when all four rows have already fractured during insertion, rather than progressively during extraction alongside spikes that remain intact, was not directly tested: this would require either the chained insertion-to-extraction simulation or a traction-based experimental retest, neither of which

was achieved in this work (Section 6.5). This progressive failure mode contrasts favourably with the more abrupt modes documented for other fixation methods, such as loop rupture in suspensory systems or sudden graft slippage (Section 2.2).

Under the idealised, undamaged geometry characterised numerically and experimentally, the LiFix construct achieved a peak extraction load of 581 N (finite element) and 725 ± 108 N (experimental, $n = 3$) — matching the range reported in the literature for interference screw fixation (602–632 N) and approaching the cross-pin benchmark (737 ± 140 N). At time-zero and with intact spike geometry, the device therefore reaches the same order of magnitude as the clinically dominant fixation method whose specific limitation — insertion mechanically opposing graft tensioning — motivated the present concept in the first place. Construct stiffness, approximately 111.8 N/mm, fell at the lower end of the interference screw range, a result attributable to the compliance of the free graft length rather than to the fixation device itself. Both the numerical and experimental load–displacement responses exhibited progressive rather than catastrophic failure, consistent with the sequential spike engagement and disengagement mechanism described above. This extraction performance is, however, conditional on the device surviving its own assembly — a condition the insertion analysis above shows is not reliably met by the present geometry.

The numerical and experimental peak extraction loads noted above agreed to within approximately 20%, a correspondence that reflects two distinct load paths converging on a comparable value — an intact, overloaded geometry in the damage-free model, against progressive spike fracture with load redistributed to residual bases in the physical specimens — rather than a validated shared failure mechanism. A stronger and independent point of corroboration was obtained from the damage-inclusive simulation: the predicted location of spike fracture, at the tip and mid-height of each spike, matched the fracture pattern observed in the mechanically tested prototypes, a geometric correspondence independent of load magnitude. A further, favourable finding concerns the graft itself: stress within the tendon remained distributed across the contact zone throughout both insertion and extraction, without the localised concentration reported in the literature at the screw–graft junction of interference screw constructs. The present device shows this favourable pattern toward the fixator — a replaceable, purpose-built component — rather than toward the graft, which is autologous tissue with no equivalent margin for damage, though this observation does not constitute a validated safety margin (Section 6.5).

Taken together, these findings identify the spike tip and mid-height as the priority for geometric refinement, ahead of any other design change, since the device must first survive assembly independently of its extraction performance. Insertion resistance may require either geometric reduction or a dedicated insertion instrument, given its proximity to the limits of manual traction. The uneven fracture severity observed across the 24 spikes in the tested prototypes suggests that load is not shared equally between rows, motivating a graded rather than uniform spike geometry. Material substitution was identified as a fallback rather than a first lever, since neither optimised processing nor toughened

PLLA formulations offer a route to substantially higher ductility without compromising the stiffness and degradation characteristics on which the rest of this work depends.

Beyond characterising this specific device, the present work addresses a methodological gap in the finite element literature on ligament fixation. Published models of fixation devices, without exception in the literature reviewed, are formulated in the already-assembled, seated configuration. This simplification is reasonable for interference screws, whose insertion and fixation mechanisms are largely independent actions, but not for a concept such as LiFix, in which both are mediated by the same geometric feature. The insertion simulation developed here, and its extension to a damage-inclusive treatment, represent the first attempt in this literature to model that coupling explicitly — and the finding that spike fracture may originate during insertion rather than solely under service load is a result that a seated-configuration model could not, by construction, have produced. This was made possible by representing the graft as an anisotropic hyperelastic material coupled to the implant through finite-sliding frictional contact, rather than through the tied constraints adopted elsewhere in the literature, which allowed interface slip and progressive failure to emerge from the simulation as results rather than being precluded by the modelling choice.

These results characterise the time-zero feasibility of the LiFix concept under an idealised, undamaged geometry; they do not substitute for cyclic loading validation, for a model incorporating the surrounding bone, or for clinical evidence, and are qualified throughout by the limitations discussed in Section 6.5. Within that scope, the overall picture to emerge from this work is a device whose anchoring mechanism is mechanically competitive once assembled, but whose assembly step, as originally dimensioned, is not yet reliably survived by the material. A preliminary geometric refinement, reported in Chapter 7, suggests this is not a fundamental limitation of the anchoring principle itself: a modest change to spike protrusion and engagement geometry was sufficient to keep insertion-phase plastic strain below the fracture-strain criterion in the damage-inclusive model — avoiding the predicted fracture, though not eliminating plastic deformation of the spikes altogether — while simultaneously improving extraction resistance. This result is preliminary — a single design point, evaluated numerically only, without independent mesh convergence or experimental confirmation — and does not substitute for the validation the original geometry lacks. It does, however, indicate that the central finding of this thesis is a property of the specific geometry tested, rather than of the spike-based anchoring concept as a whole, and it is this distinction, more than the extraction load achieved by either geometry, that most directly shapes the priorities for the device's continued development.

Chapter 9

Future Works

The findings of this thesis point most directly to a redesign of the spike geometry as the necessary first step for any continuation of this work. Because spike tip fracture was shown to occur during graft insertion itself, across the full range of ductility considered for PLLA, none of the extensions discussed below — further simulation, cyclic testing, or bone modelling — would be a productive use of effort until the anchoring geometry survives its own assembly.

Spike geometry redesign

A preliminary refinement targeting the spike geometry, reported in Chapter 7, achieved this: reducing spike protrusion and curving the engagement face kept insertion-phase plastic strain below the fracture-strain criterion under the damage-inclusive model — preventing the predicted fracture, though the spikes still undergo measurable permanent plastic deformation (Table 7.1) — while improving extraction resistance. This result was obtained from a single design point, evaluated without independent mesh convergence, sensitivity analysis, or experimental confirmation. A systematic exploration of this design space — varying protrusion depth, engagement curvature, and row-graded geometry independently rather than as a single combined change — is the most direct extension of the present work, and would establish which parameter is primarily responsible for the observed improvement.

Damage model calibration

The ductile damage parameters adopted in Section 6.2.1 were estimated from the bulk elongation-at-break range reported for PLLA rather than measured for the specific additively manufactured material used in this device. A tensile test programme on printed PLLA coupons, ideally following the same print orientation and layer parameters as the fixator itself, would allow the damage-initiation criterion to be calibrated rather than assumed.

Chained insertion-to-extraction simulation

A currently unresolved limitation is the numerical instability encountered when attempting to continue the damage-inclusive insertion model directly into the extraction step, associated with severe element distortion following spike fracture. Resolving this — through refined section controls, distortion control, or local remeshing at the fracture zone — would allow the extraction response to be characterised starting from the degraded, rather than idealised, post-insertion geometry, closing the gap identified as the most consequential limitation of the present work.

Local mesh sensitivity at the spike root

Local mesh sensitivity at the spike root was not separately verified in this thesis, and the use of C3D4 elements for a nearly incompressible hyperelastic tendon is known to be susceptible to volumetric locking. Repeating the analysis with C3D10M elements, at least in the spike root region, would test whether the reported strain magnitudes are sensitive to this choice.

Friction coefficient sensitivity

The friction coefficient adopted throughout (0.4) was taken from the literature rather than measured for the specific graft surrogate and printed PLLA surface used here. A sensitivity study across a plausible range would establish how strongly the reported insertion and extraction responses depend on this assumption.

Strain-rate sensitivity and viscoelastic material representation

The tendon was represented using the HGO formulation, an anisotropic hyperelastic model that already exceeds the isotropic linear elastic representations adopted in much of the finite element literature on ligament fixation reviewed in this thesis, including that of Chen et al. (Section 6.3.2). Even so, this formulation remains purely hyperelastic and does not capture the viscoelastic, time- and rate-dependent behaviour known to be present in tendinous tissue, nor does the elastic-plastic PLLA model include any rate dependence. Combined with the instantaneous velocity of the smooth-step loading, which varies continuously through each step and reaches values two to three orders of magnitude above the 1 mm/s used experimentally, this leaves open the possibility that part of the divergence between the numerical and experimental results (Section 6.2.2) reflects rate effects that neither model can represent. Repeating the simulations at loading rates closer to the experimental value, and, more ambitiously, incorporating a viscoelastic component into the tendon representation, would allow this contribution to be isolated from the other sources of divergence already discussed.

Traction-based experimental retesting

Because the mechanical tests reported in Chapter 5, like the extraction simulation, characterised the device from an idealised, undamaged starting geometry, repeating the mechanical testing with the graft surrogate drawn through the device under axial traction — rather than threaded fibre by fibre, as in the present protocol — would test the device under the same insertion-induced degradation identified numerically, closing this limitation experimentally rather than leaving it as a declared caveat.

Cyclic loading

No cyclic loading was applied in either the numerical or experimental work; given that several of the biomechanical benchmarks against which this device was compared (Section 6.3.1) are themselves cyclic measurements, a cyclic testing programme — numerical and experimental — would place the present time-zero characterisation on a more directly comparable footing.

Bone representation

The current model excludes the surrounding bone entirely, representing the fixator as rigidly anchored. Incorporating a representative trabecular and cortical bone model would allow failure modes specific to bone-implant interaction, such as thread pull-out or tunnel wall yielding, to be assessed alongside the graft-fixator interface characterised here, and would constitute a necessary step prior to any cadaveric or animal-model validation of the device as a whole.

Graft laceration threshold

No validated threshold for graft laceration exists in the literature for the HGO material representation adopted in this work, a gap general enough that establishing one, whether through dedicated mechanical testing or a focused literature synthesis, would itself constitute a useful and largely unaddressed contribution, given how sparse the available evidence on this specific point appears to be.

Extension to other ligamentoplasty applications

The present work was deliberately scoped to ACL reconstruction, for the clinical and mechanical reasons discussed in Section 2.1, but the underlying spike-based anchoring principle was conceived with a more versatile structural architecture in mind. Having established a baseline mechanical characterisation at the scale of the knee joint, a natural extension of this work is the adaptation of the same anchoring principle to the smaller,

more geometrically constrained ligamentous repairs for which the knee joint was, from the outset, intended as a benchmarking environment.

References

[1] Nathan A Mall, Peter N Chalmers, Mario Moric, Miho J Tanaka, Brian J Cole, Bernard R Jr Bach, and George A Jr Paletta. Incidence and trends of anterior cruciate ligament reconstruction in the united states. *The American Journal of Sports Medicine*, 42(10):2363–2370, 2014. doi: 10.1177/0363546514542796.

[2] Ulrike Wittig, Georg Hauer, Ines Vielgut, Patrick Reinbacher, Andreas Leithner, and Patrick Sadoghi. Application and surgical technique of acl reconstruction using worldwide registry datasets: What can we extract? *Journal of Functional Morphology and Kinesiology*, 7(1):2, 2022. ISSN 2411-5142. doi: 10.3390/jfmk7010002.

[3] Lars-Petter Granan, Magnus Forssblad, Martin Lind, and Lars Engebretsen. The scandinavian acl registries 2004–2007: baseline epidemiology. *Acta Orthopaedica*, 80 (5):563–567, 2009. doi: 10.3109/17453670903350107.

[4] David Jorge Carvalho Fernandes. Finite element analysis of the acl-deficient knee. Master's thesis, Instituto Superior Técnico, Universidade de Lisboa, 2014.

[5] Arthritis Knee Pain Centers. Anatomy of the knee, 2026. URL https://arthritiskneepain.com/wellness-blog/anatomy-of-the-knee/. Accessed: June 9, 2026.

[6] Musculoskeletal Key. Basic science of the knee, 2026. URL https://musculoskeletalkey.com/basic-science-of-the-knee/. Accessed: June 9, 2026.

[7] Rocco Papalia, Sebastiano Vasta, Stefano D'Adamio, A. Giacalone, N. Maffulli, and V. Denaro. Metallic or bioabsorbable interference screw for graft fixation in anterior cruciate ligament (ACL) reconstruction? *British Medical Bulletin*, 109(1): 19–29, 2014. doi: 10.1093/bmb/ldt038. URL https://academic.oup.com/bmb/article-abstract/109/1/19/292514.

[8] Athar Ahemad and Anand B. Anerao. Comparison of tunnel widening between interference screw and suture disc fixation after ACL reconstruction using CT scan. *International Journal of Research in Orthopaedics*, 4(2):266–270, 2018. ISSN 2455-4510. doi: 10.18203/issn.2455-4510.IntJResOrthop20180510. URL https://www.ijoro.org/index.php/ijoro/article/view/653.

[9] Ortho Implants India. Interference screw-2 (product catalog no. 2). Ortho Implants India / Zealmax Innovations Pvt. Ltd., 2026. URL https://orthoimplantsindia.com/product/interference-screw-2/. Accessed: June 19, 2026.

[10] Michael Stalder, Mazda Farshad, Jess G. Snedeker, Dominik C. Meyer, and Bruno Fuchs. Interference screws should be shorter than the hamstring tendon graft in

the bone tunnel for best fixation. *Knee Surgery, Sports Traumatology, Arthroscopy*, 21(8):1783–1788, 2013. ISSN 1433-7347. doi: 10.1007/s00167-012-1957-y. URL https://link.springer.com/article/10.1007/s00167-012-1957-y.

[11] Ari Digiácomo Ocampo Moré, André Luiz Pizzolatti, Eduardo Alberto Fancello, and Carlos Rodrigo de Mello Roesler. Biomechanical performance of metallic and bioabsorbable interference screw for tibial graft fixation in ACL reconstruction. In *ASME Summer Bioengineering Conference*, volume 55614, page V01BT23A011. American Society of Mechanical Engineers, 2013. doi: 10.1115/SBC2013-14492. URL https://asmedigitalcollection.asme.org/SBC/proceedings-pdf/SBC2013/55614/V01BT23A011/4206753/v01bt23a011-sbc2013-14492.pdf.

[12] Abdul Halim Abdullah, Helmi Rashid, Jamaluddin Mahmud, Muhammad Fauzi Othman, and Muhamad Widad Al-Jefri Ibrahim. Effects of screw materials in anterior cruciate ligament reconstruction using finite element analysis. *Procedia Engineering*, 31:720–725, 2012. ISSN 1877-7058. doi: 10.1016/j.proeng.2012.01.1092. URL https://www.sciencedirect.com/science/article/pii/S1877705812027580.

[13] Charles A. Su, Derrick M. Knapik, Nikunj N. Trivedi, Mark F. Megerian, Michael J. Salata, and James E. Voos. Femoral interference screw fixation in ACL reconstruction using bone-patellar tendon-bone grafts. *JBJS Reviews*, 8(1):e0066, 2020. ISSN 2168-6181. doi: 10.2106/JBJS.RVW.19.00066. URL https://journals.lww.com/jbjsreviews/abstract/2020/01000/femoral_interference_screw_fixation_in_acl.12.aspx.

[14] F. Adam, D. Pape, O. Steimer, D. Kohn, and S. Rupp. Biomechanische eigenschaften der interferenzverschraubung beim ersatz des vorderen kreuzbandes mit patellar- und hamstring-transplantaten: Eine experimentelle studie mittels röntgenstereometrieanalyse (RSA). *Der Orthopäde*, 30(9):649–657, 2001. doi: 10.1007/s001320170053. URL https://link.springer.com/article/10.1007/s001320170053.

[15] Wojciech Widuchowski, Małgorzata Widuchowska, Bogdan Koczy, Szymon Dragan, Andrzej Czamara, Wiesław Tomaszewski, and Jerzy Widuchowski. Femoral press-fit fixation in ACL reconstruction using bone-patellar tendon-bone autograft: results at 15 years follow-up. *BMC Musculoskeletal Disorders*, 13(1):115, 2012. ISSN 1471-2474. doi: 10.1186/1471-2474-13-115. URL https://doi.org/10.1186/1471-2474-13-115.

[16] Sarvpreet Singh, Shalin Corporate Shaunak, Sebastian C. K. Shaw, John L. Anderson, and Vipul Mandalia. Adjustable loop femoral cortical suspension devices for anterior cruciate ligament reconstruction: A systematic review. *Indian Journal of Orthopaedics*, 54(4):426–443, 2020. ISSN 0973-6492. doi: 10.1007/s43465-019-00022-4. URL https://link.springer.com/article/10.1007/s43465-019-00022-4.

[17] Mira Dreier, Samuel Bachmaier, Christian Baumgartner, and Jörg Schröttner. Evaluation of adjustable loop suspensory anterior cruciate ligament fixation devices. *Current Directions in Biomedical Engineering*, 5(1):505–508, 2019. ISSN 2364-5504. doi: 10.1515/cdbme-2019-0127. URL https://www.degruyter.com/document/doi/10.1515/cdbme-2019-0127/html.

[18] James Randolph Onggo, Mithun Nambiar, and Vishal Pai. Fixed- versus adjustable-loop devices for femoral fixation in anterior cruciate ligament reconstruction:

A systematic review. *Arthroscopy: The Journal of Arthroscopic & Related Surgery*, 35(8):2484–2498, 2019. ISSN 0749-8063. doi: 10.1016/j.arthro.2019.02.029. URL https://arthroscopyjournals.onlinelibrary.wiley.com/doi/10.1016/j.arthro.2019.02.029.

[19] Benjamin C. Noonan, Joshua S. Dines, Answorth A. Allen, David W. Altchek, and Asheesh Bedi. Biomechanical evaluation of an adjustable loop suspensory anterior cruciate ligament reconstruction fixation device: The value of retensioning and knot tying. *Arthroscopy: The Journal of Arthroscopic & Related Surgery*, 32(8):1650–1659, 2016. ISSN 0749-8063. doi: 10.1016/j.arthro.2016.02.010. URL https://www.arthroscopyjournal.org/article/S0749-8063(16)00155-2/fulltext.

[20] Ryo Iuchi, Tatsuo Mae, Yuta Tachibana, Konsei Shino, Shigeto Nakagawa, Hideki Yoshikawa, and Ken Nakata. Mechanical properties of an adjustable-loop cortical suspension device for anterior cruciate ligament reconstruction. *Orthopaedic Journal of Sports Medicine*, 6(8):2325967118791223, 2018. ISSN 2325-9671. doi: 10.1177/2325967118791223. URL https://journals.sagepub.com/doi/10.1177/2325967118791223.

[21] Sebastian Schützenberger, Florian Keller, Sebastian Grabner, Danijel Kontic, and Christian Fialka. ACL reconstruction with femoral and tibial adjustable versus fixed-loop suspensory fixation: a retrospective cohort study. *Journal of Orthopaedic Surgery and Research*, 17(1):244, 2022. ISSN 1749-799X. doi: 10.1186/s13018-022-03128-y. URL https://doi.org/10.1186/s13018-022-03128-y.

[22] L. N. Rodd, A. Mofidi, E. Sclippa, and M. S. Thompson. Mechanical evaluation of bioabsorbable cross-pins used for femoral fixation in anterior cruciate ligament reconstruction. *Proceedings of the Institution of Mechanical Engineers, Part H: Journal of Engineering in Medicine*, 224(7):879–887, 2010. doi: 10.1243/09544119JEIM728.

[23] Carlos Rodrigo de Mello Roesler, André Luiz Almeida Pizzolatti, Eduardo Fancello, and Ari Digiácomo Ocampo Moré. Biomechanical performance of Bio Cross-Pin and EndoButton for ACL reconstruction at femoral side: a porcine model. *Research on Biomedical Engineering*, 32(1):28–34, 2016. doi: 10.1590/2446-4740.0720.

[24] Scott A Rodeo, Sumito Kawamura, Hyon-Jeong Kim, Christian Dynybil, and Liang Ying. Tendon healing in a bone tunnel differs at the tunnel entrance versus the tunnel exit: an effect of graft-tunnel motion? *The American Journal of Sports Medicine*, 34(11):1790–1800, 2006. doi: 10.1177/0363546506290059.

[25] Timothy McGlaston, Vahid Entezari, Tara Nazarian, and Arun J. Ramappa. The safe zone for cross-pin fixation in anterior cruciate ligament reconstruction using anteromedial portal technique. *The Orthopaedic Journal at Harvard Medical School*, 11:62–67, 2009. URL https://www.orthojournalhms.org/.

[26] Hee-Soo Kyung, Seung-Gil Baek, Byoung-Joo Lee, and Chang-Hwa Lee. Single-Bundle Anterior Cruciate Ligament Reconstruction with Semitendinosus Tendon Using the PINN-ACL CrossPin System: Minimum 4-Year Follow-up. *Knee Surgery & Related Research*, 27(1):43–48, 2015. ISSN 2234-0726. doi: 10.5792/ksrr.2015.27.1.43. URL https://doi.org/10.5792/ksrr.2015.27.1.43.

[27] R. Strehl, D. Jorda, and L. Gotzen. A biomechanical evaluation of the tibial cross-pin fixation of the bone-patellar-tendon-bone graft using biointegrable CB pins: An experimental study in porcine specimens. *Sportverletzung·Sportschaden*, 21(1): 31–36, 2007. ISSN 0932-0555. doi: 10.1055/s-2007-960733. URL https://www.thieme-connect.com/products/ejournals/abstract/10.1055/s-2007-960733.

[28] Gregory E Bellisari, Christopher C Kaeding, and Alan S Litsky. Mechanical evaluation of cross pins used for femoral fixation of hamstring grafts in acl reconstructions. *Orthopedics*, 33(10):722, 2010. doi: 10.3928/01477447-20100826-08.

[29] Sufian S. Ahmad, C. Evren, U. Schanz, S. Kohl, S. Lorenz, and A. Ateschrang. Biomechanical properties of femoral cross-pin fixation in acl reconstruction: bone density dictates pin migration. *Knee Surgery, Sports Traumatology, Arthroscopy*, 21 (4):902–907, 2013. doi: 10.1007/s00167-012-2122-z.

[30] Thore Zantop, A. Weimann, M. Rümmler, J. Hassenpflug, and W. Petersen. Initial fixation strength of two bioabsorbable transfixation devices for femoral fixation of hamstring grafts. *The American Journal of Sports Medicine*, 32(3):641–647, 2004. doi: 10.1177/0363546503261719.

[31] Benjamin M. Amalfi, Nathanial Smith, Jeffrey P. Johnson, Marcio Ribeiro, and Mark D. Miller. The evolution of suture anchor fixation in anterior cruciate ligament reconstruction: A biomechanical and clinical review. *Journal of Orthopaedic Research and Reviews*, 14(2):112–121, 2022. doi: 10.1016/j.jorr.2022.03.004.

[32] Jiaxin Liu, Hongyu Li, Meng Wang, Yiran Wang, Guanxin Guo, and Hangzhou Zhang. Research progress of suture augmentation in anterior cruciate ligament reconstruction. *Chinese Journal of Reparative and Reconstructive Surgery*, 39(4): 504–510, 2025. ISSN 1002-1892. doi: 10.7507/1002-1892.202411032. URL http://www.rrs.org.cn/CN/abstract/abstract10164.shtml.

[33] Christiaan H. W. Heusdens. ACL repair: A game changer or will history repeat itself? A critical appraisal. *Journal of Clinical Medicine*, 10(5):912, 2021. ISSN 2077-0383. doi: 10.3390/jcm10050912. URL https://doi.org/10.3390/jcm10050912.

[34] Benjamin L. Smith, Asheesh Bedi, Jordan L. Liles, Christopher Johnston, and Jonathan C. Riboh. All-Suture Anchor Onlay Fixation for Medial Patellofemoral Ligament Reconstruction: A Biomechanical Comparison of Fixation Constructs. *The American Journal of Sports Medicine*, 52(14):3522–3529, 2024. ISSN 0363-5465. doi: 10.1177/03635465241285324. URL https://pubmed.ncbi.nlm.nih.gov/39583149/.

[35] F. Alan Barber, Mark A. Herbert, and Jeffrey C. Beavis. Suture anchor materials, eyelets, and designs: a biomechanical review. *Arthroscopy: The Journal of Arthroscopic & Related Surgery*, 29(5):934–942, 2013. doi: 10.1016/j.arthro.2013.01.031.

[36] Markus J. Tingart, Mary L. Bouxsein, David Zurakowski, Jon J. P. Warner, and Maria Apreleva. Anchor design and bone mineral density affect the pull-out strength of suture anchors in rotator cuff repair: which anchors are best to use in patients with low bone quality? *The American Journal of Sports Medicine*, 31(3):367–373, 2003. doi: 10.1177/03635465030310030801.

[37] Dominikus C. Meyer, Richard W. Nyffeler, Sandro F. Fucentese, and Christian Gerber. Failure of suture material at suture anchor eyelets. *Arthroscopy: The Journal of Arthroscopic & Related Surgery*, 18(9):1013–1019, 2002. doi: 10.1053/jars.2002.36113.

[38] Jeremy Pfeiffer, Ariel Shani, Aaron Sorkin, Robert Goldstein, and Robert J. Meislin. Biomechanical evaluation of high-strength sutures and knots under cyclic loading. *Journal of Orthopaedic Surgery and Research*, 9(1):42–48, 2014. doi: 10.1186/1749-799X-9-42.

[39] Ashish Keoliya and Swapnil U. Ramteke. A case report on medial patellofemoral ligament reconstruction rehabilitation in a cricket player through targeted agility training. *Cureus*, 16(3):e56002, 2024. ISSN 2168-8184. doi: 10.7759/cureus.56002. URL https://doi.org/10.7759/cureus.56002.

[40] Ömür Oto, Hasan Bombacı, and Ömer Faruk Öztürk. The effect of additional staple in the tibial fixation of anterior cruciate ligament reconstruction: a biomechanical study in sheep tibia. *Joint Diseases and Related Surgery*, 31(3):507–512, 2020. doi: 10.5606/ehc.2020.75165.

[41] T. G. Gerich, A. Cassim, C. Lattermann, H. P. Lobenhoffer, and H. Tscherne. Ausreißkraft der tibialen transplantatfixierung für den ersatz des vorderen kreuzbands. interferenzschrauben vs. staples. *Der Unfallchirurg*, 101(3):204–208, 1998. ISSN 0011-3005. doi: 10.1007/s001130050255. URL https://pubmed.ncbi.nlm.nih.gov/9577217/.

[42] Fadlurrahman Manaf, I Putu Alit Pawana, Kukuh Dwiputra Hernugrahanto, Zainurrahman Kurnia Putra, and Dwikora Novembri Utomo. Button screw versus button staple anchor in single bundle anterior cruciate ligament reconstruction: A comparative study of gait analysis, outcome analysis and cost effectiveness. *Journal of Orthopaedic Reports*, 4(4):100831, 2025. ISSN 2773-157X. doi: 10.1016/j.jorep.2025.100831. URL https://doi.org/10.1016/j.jorep.2025.100831.

[43] Amar Vadhera, Derrick M. Knapik, Safa Gursoy, Daniel Farivar, Nikhil N. Verma, Charles A. Bush-Joseph, and Brian Forsythe. Current concepts in anterior tibial closing wedge osteotomies for anterior cruciate ligament deficient knees. *Current Reviews in Musculoskeletal Medicine*, 14(6):441–451, 2021. ISSN 1935-973X. doi: 10.1007/s12178-021-09729-0. URL https://doi.org/10.1007/s12178-021-09729-0.

[44] Wei Wen Timothy Teo, Ching Sing Nicholas Yeoh, and Teck Huat Andy Wee. Tibial fixation in anterior cruciate ligament reconstruction: Is supplementary staple fixation necessary? *Journal of Orthopaedic Surgery*, 25(1):2309499017690313, 2017. ISSN 2309-4990. doi: 10.1177/2309499017690313. URL https://journals.sagepub.com/doi/10.1177/2309499017690313.

[45] Cem Yıldırım, Mehmet Demirel, Emre Koraman, Osman Görkem Muratoğlu, Fatih Yamak, Süreyya Ergün Bozdağ, and Yavuz Kocabey. The effect of supplementary staple fixation on biomechanical properties of soft tissue graft tibial fixation in anterior cruciate ligament reconstruction. *The Journal of Knee Surgery*, 37(10):736–741, 2024. ISSN 1538-8506. doi: 10.1055/s-0044-1786007. URL https://pubmed.ncbi.nlm.nih.gov/38599605/.

[46] Tinghan Sun and Hangzhou Zhang. Biomechanical comparison of a novel tibial fixation technique versus interference screw fixation for acl reconstruction using soft tissue grafts. *Orthopaedic Journal of Sports Medicine*, 9(8), 2021. doi: 10.1177/23259671211028559.

[47] Siqi Chen, Junyuan Wang, Junhua Yu, Wenxuan Li, Yuhang Lv, and Hangzhou Zhang. Internal brace augmentation in acl reconstruction increases structural strength and stiffness: a biomechanical study in a porcine tibia model. *Scientific Reports*, 15 (1):[article number], 2025. doi: 10.1038/s41598-025-98491-1.

[48] Scott O. Paschal, Mitchell D. Seemann, Richard B. Ashman, Randy N. Allard, and James B. Montgomery. Interference fixation versus postfixation of bone-patellar tendon-bone grafts for anterior cruciate ligament reconstruction: A biomechanical comparative study in porcine knees. *Clinical Orthopaedics and Related Research*, 300:281–287, March 1994. doi: 10.1097/00003086-199403000-00040.

[49] Stefan Rupp, Paul W. Krauss, and Ekkehard W. Fritsch. Fixation strength of a biodegradable interference screw and a press-fit technique in anterior cruciate ligament reconstruction with a bptb graft. *Arthroscopy: The Journal of Arthroscopic & Related Surgery*, 13(1):61–65, February 1997. doi: 10.1016/S0749-8063(97)90210-3.

[50] Christopher S Ahmad, Thomas R Gardner, Megan Groh, Johnny Arnouk, and William N Levine. Mechanical properties of soft tissue femoral fixation devices for anterior cruciate ligament reconstruction. *The American Journal of Sports Medicine*, 32(3):704–710, 2004. doi: 10.1177/0363546503261714.

[51] Brandon J Erickson, Joseph Nguyen, and Beth E Shubin Stein. Isolated medial patellofemoral ligament reconstruction for patellar instability regardless of tibial tubercle–trochlear groove distance and patellar height: outcomes at 1 and 2 years. *The American Journal of Sports Medicine*, 47(6):1331–1337, 2019. doi: 10.1177/0363546519835800.

[52] Daniel J Hurwit, Nahir A Habet, Joshua D Meade, Alexander N Berk, Bradley L Young, Susan Odum, Schangcheng Wang, Michael S Schallmo, James E Fleischli, David P Trofa, and Bryan M Saltzman. Biomechanical comparison of tibial-sided supplemental fixation techniques in bone-patellar tendon-bone anterior cruciate ligament reconstruction. *The Knee*, 41:66–71, 2023. doi: 10.1016/j.knee.2022.12.005.

[53] John J Lee, Karimdad Otarodifard, Bong Jae Jun, Michelle H McGarry, George F Hatch, and Thay Q Lee. Is supplementary fixation necessary in anterior cruciate ligament reconstructions? *The American Journal of Sports Medicine*, 39(2):360–365, 2011. doi: 10.1177/0363546510390434.

[54] Y Kocabey, S Klein, J Nyland, and D Caborn. Tibial fixation comparison of semitendinosus-bone composite allografts fixed with bioabsorbable screws and bone-patella tendon-bone grafts fixed with titanium screws. *Knee Surgery, Sports Traumatology, Arthroscopy*, 12(2):88–93, 2004. doi: 10.1007/s00167-003-0370-y.

[55] Hsain-Chung Shen, Jen-Huei Chang, Chian-Her Lee, Pei-Hung Shen, Tsu-Te Yeh, Chia-Chun Wu, and Chun-Lin Kuo. Biomechanical comparison of cross-pin and endobutton-cl femoral fixation of a flexor tendon graft for anterior cruciate ligament

reconstruction–a porcine femur-graft-tibia complex study. *Journal of Surgical Research*, 161(2):282–287, 2010. doi: 10.1016/j.jss.2009.01.015.

[56] Sean Martin, Samuel I Fuller, Mark T Ehrensberger, Marco Caiola, Elise Martin, and Leslie J Bisson. A biomechanical comparison of patellar fixation techniques in medial patellofemoral ligament reconstruction. *Orthopaedic Journal of Sports Medicine*, 13 (11), 2025. doi: 10.1177/23259671251391769.

[57] Andre Weimann, Thore Zantop, Markus Rümmler, Joachim Hassenpflug, and Wolf Petersen. Primary stability of bone-patellar tendon-bone graft fixation with biodegradable pins. *Arthroscopy: The Journal of Arthroscopic & Related Surgery*, 19 (10):1097–1102, December 2003. doi: 10.1016/j.arthro.2003.10.023.

[58] Patrick A Smith, Marina Piepenbrink, Shelby K Smith, Samuel Bachmaier, Asheesh Bedi, and Coen A Wijdicks. Adjustable- versus fixed-loop devices for femoral fixation in acl reconstruction: an in vitro full-construct biomechanical study of surgical technique–based tibial fixation and graft preparation. *Orthopaedic Journal of Sports Medicine*, 6(4), 2018. doi: 10.1177/2325967118768743.

[59] N J Rowden, D Sher, G J Rogers, and K Schindhelm. Anterior cruciate ligament graft fixation. initial comparison of patellar tendon and semitendinosus autografts in young fresh cadavers. *The American Journal of Sports Medicine*, 25(4):472–478, 1997. doi: 10.1177/036354659702500409.

[60] K A Taylor, H C Cutcliffe, R M Queen, G M Utturkar, C E Spritzer, W E Garrett, and L E DeFrate. In-vivo measurement of acl length and relative strain during walking. *Journal of Biomechanics*, 46(3):478–483, 2013. doi: 10.1016/j.jbiomech.2012.10.031.

[61] N Chandrashekar, H Mansouri, J Slauterbeck, and J Hashemi. Sex-based differences in the tensile properties of the human anterior cruciate ligament. *Journal of Biomechanics*, 39(16):2943–2950, 2006. doi: 10.1016/j.jbiomech.2005.10.031.

[62] Mahmoud Chizari, Bin Wang, Martyn Snow, and Mel Barrett. Experimental and numerical analysis of screw fixation in anterior cruciate ligament reconstruction. In *Current Themes in Engineering Science 2007: Selected Presentations at the World Congress on Engineering*, volume 1045 of *AIP Conference Proceedings*, pages 61–70. AIP, 2008. doi: 10.1063/1.2991351.

[63] O J Simões, A Ramos, J P Oliveira, J C Noronha, and J A Simões. A review on finite element analysis of the anterior cruciate ligament reconstruction. *Open Journal of Orthopedics and Rheumatology*, 6(1):001–011, 2021. doi: 10.17352/ojor.000031.

[64] C Quintana Barcia, C Rodríguez González, C Betegón Biempica, G Álvarez Díaz, and A Maestro. Anterior cruciate ligament reconstruction numeric and experimental analyses: influence of trabecular bone constitutive model. *British Journal of Surgery*, 108(Supplement_3):znab160.014, 2021. doi: 10.1093/bjs/znab160.014.

[65] Daniel F O'Brien, Lilah Fones, Victoria Stoj, Cory Edgar, Katherine Coyner, and Robert A Arciero. Confirming proper button deployment of suspensory fixation during acl reconstruction. *Orthopaedic Journal of Sports Medicine*, 9(1), 2021. doi: 10.1177/2325967120974349.

[66] Konstantinos Risvas, Dimitar Stanev, Lefteris Benos, Konstantinos Filip, Dimitrios Tsaopoulos, and Konstantinos Moustakas. Evaluation of anterior cruciate ligament surgical reconstruction through finite element analysis. *Scientific Reports*, 12:8044, 2022. doi: 10.1038/s41598-022-11601-1.

[67] James H Lubowitz, Randy Schwartzberg, and Pat Smith. Cortical suspensory button versus aperture interference screw fixation for knee anterior cruciate ligament soft-tissue allograft: a prospective, randomized controlled trial. *Arthroscopy: The Journal of Arthroscopic & Related Surgery*, 31(9):1733–1739, 2015. ISSN 0749-8063. doi: 10.1016/j.arthro.2015.03.033.

[68] Nur Afikah Zainal Abidin, Abdul Hadi Abdul Wahab, Rabiatul Adibah Abdul Rahim, Mohammed Rafiq Abdul Kadir, and Muhammad Hanif Ramlee. Biomechanical analysis of three different types of fixators for anterior cruciate ligament reconstruction via finite element method: a patient-specific study. *Medical & Biological Engineering & Computing*, 59:1945–1960, 2021. doi: 10.1007/s11517-021-02419-6.

[69] Bryan M Saltzman, Shangcheng Wang, Nahir A Habet, Ian S Hong, David P Trofa, Joshua D Meade, James E Fleischli, and Dana P Piasecki. The hybrid transtibial technique for femoral tunnel drilling in anterior cruciate ligament reconstruction: a finite element analysis model of graft bending angles and peak graft stresses in comparison with transtibial and anteromedial portal techniques. *Journal of the American Academy of Orthopaedic Surgeons*, 30(18):e1195–e1206, 2022. doi: 10.5435/JAAOS-D-21-00883.

[70] Iskandar Mahdi Alardi. Hamstring graft size for anterior cruciate ligament repair in a sample of iraqi men. *Journal of Medicine and Life*, 16(10):1445–1447, 2023. doi: 10.25122/jml-2023-0071.

[71] Fahad N A Alkhalaf, Sager Hanna, Mohammed Saleh Hattab Alkhaldi, Fares Alenezi, and Aliaa Khaja. Autograft diameter in acl reconstruction: size does matter. *SICOT-J*, 7:16, 2021. doi: 10.1051/sicotj/2021018.

[72] Andreas Flury, Linda Wild, Manuel Waltenspül, Christoph Zindel, Lazaros Vlachopoulos, Florian B Imhoff, and Sandro F Fucentese. Tibial tunnel enlargement is affected by the tunnel diameter-screw ratio in tibial hybrid fixation for hamstring acl reconstruction. *Archives of Orthopaedic and Trauma Surgery*, 143(4):1923–1930, 2023. doi: 10.1007/s00402-022-04408-2.

[73] S. J. Simske, R. A. Ayers, and T. A. Bateman. Porous materials for bone engineering. *Materials Science Forum*, 250:151–182, 1997.

[74] Yunwei Cui, Kai Ding, Hongzhi Lv, Xiaodong Cheng, Zixi Fan, Dacheng Sun, Yifan Zhang, Wei Chen, and Yingze Zhang. Biomechanical optimization of the magnesium alloy bionic cannulated screw for stabilizing femoral neck fractures: a finite element analysis. *Frontiers in Bioengineering and Biotechnology*, 12:1448527, 2024. doi: 10.3389/fbioe.2024.1448527.

[75] Esteban Andres Lobos Centeno, Vincent Martinel, Juan Enrique Cassinelli, Philippe Colombet, and Johannes Barth. Optimizing hamstring tendon graft harvesting technique for anterior cruciate and anterolateral ligament reconstruction. *Arthroscopy Techniques*, 14(4):103311, 2025. doi: 10.1016/j.eats.2024.103311.

[76] Martijn Dietvorst, M C Marieke van der Steen, Marijn van den Besselaar, and Rob P A Janssen. Height is a predictor of hamstring tendon length and ACL graft characteristics in adolescents. *BMC Musculoskeletal Disorders*, 24(1):563, 2023. doi: 10.1186/s12891-023-06705-2.

[77] Bryce Clinger, John Xerogeanes, Julian Feller, Christian Fink, Armin Runer, Dustin Richter, and Daniel Wascher. Quadriceps tendon autograft for anterior cruciate ligament reconstruction: state of the art. *Journal of ISAKOS*, 7(6):162–172, 2022. doi: 10.1016/j.jisako.2022.08.010.

[78] Charles H Brown Jr. Preparation of 5- and 6-strand hamstring tendon grafts for single-bundle hamstring anterior cruciate ligament reconstruction. In Sachin Tapasvi, editor, *Techniques in ACL Surgery*, pages 33–46. Jaypee Brothers Medical Publishers, 1 edition, 2017. ISBN 9789352700363. doi: 10.5005/jp/books/14236_5.

[79] Sara Sadeqi, Rodney Summers, Deniz U Erbulut, and Vijay K Goel. Optimization of material coefficients in the holzapfel-gasser-ogden material model for the main four ligaments of the knee joint-a finite element study. *Applied Mathematics*, 12(12): 1166–1188, 2021. ISSN 2152-7393. doi: 10.4236/am.2021.1212075.

[80] V Podrážka and P Sedmera. Density of bovine collagen. *Acta Biochimica et Biophysica*, 1966. Reported density range: 1.30–1.40 g/cm³ for dry collagen.

[81] J Hashemi, N Chandrashekar, and J Slauterbeck. The mechanical properties of the human patellar tendon are correlated to its mass density and are independent of sex. *Clinical Biomechanics*, 20(6):645–652, 2005. doi: 10.1016/j.clinbiomech.2005.02.008.

[82] Polymers Journal. Table 2: Mechanical properties of plla composites. *Polymers*, 2021. PMCID: PMC8587543. PLLA film with 40 wtYoung's Modulus = 2.7 ± 0.4 GPa.

[83] Cambridge University. *Controlling the alignment and degradation of 3D printed poly-L-lactic acid for redesigned coronary stents.* PhD thesis, University of Cambridge, 2025. Repository: https://www.repository.cam.ac.uk/items/74438a39-617f-44dc-906b-fc464d326439. Young's modulus reported as 2.77 ± 0.28 GPa.

[84] Longzhen Wang, Pengfei Dong, David L Wilson, Hiram G Bezerra, and Linxia Gu. Mechanical performance of PLLA stent. In *Proceedings of the ASME 2018 Design of Medical Devices Conference*, 2018. doi: 10.1115/DMD2018-6957. PMCID: PMC6103219. Young's modulus = 3.3 GPa, Poisson's ratio = 0.3, density = 1.25 g/cm³.

[85] Yung-Yueh Hsu, Joseph D Gresser, Debra J Trantolo, and Donald L Wise. Effect of polymer foam morphology and density on kinetics of in vitro controlled release of isoniazid from compressed foam matrices. *Journal of Biomedical Materials Research*, 35(1):107–116, 1997. doi: 10.1002/(SICI)1097-4636(199704)35:1<107::AID-JBM12>3.0.CO;2-C.

[86] James F Macnamara, Richard Vallery, David Gidley, and Rafael Auras. Density and crystallinity correlations: Enhancing moisture barrier properties in poly(l-lactic acid), poly(d-lactic acid), and stereocomplex-poly(l,d-lactic acid) films. *Journal of Applied Polymer Science*, 2025. doi: 10.1002/app.56986. Open access. Amorphous PLLA densities: 1,230–1,243 kg/m³; semi-crystalline: 1,250–1,257 kg/m³; fully crystalline PLLA: 1,270 kg/m³; 50/50 PLLA/PDLA blend: 1,285 kg/m³.

[87] Dana Dohr, Katharina Wulf, Niels Grabow, Robert Mlynski, and Sebastian P Schraven. A PLLA coating does not affect the insertion pressure or frictional behavior of a CI electrode array at higher insertion speeds. *Materials*, 15(9):3049, 2022. doi: 10.3390/ma15093049.

[88] Mohamed Ahmed Ramadan, Hassan A Sabour, and Eman EL-Shenawy. Tribological properties of 3D printed polymers: PCL, ABS, PLA and Co polyester. *Tribology in Industry*, 45(1):161–167, 2023. doi: 10.24874/ti.1410.11.22.02.

[89] Chunfeng Zhao, Peter C Amadio, and Kai Nan An. Tendon friction, lubrication, and biomechanics of motion. In Jin Bo Tang, editor, *Tendon Surgery of the Hand*, pages 24–34. Elsevier, 2012. ISBN 9781437722307.

[90] Dassault Systèmes. *Abaqus Analysis User's Guide*. Dassault Systèmes Simulia Corp., Providence, RI, USA, 2022. Abaqus 2022.

[91] Jan Theopold, Stefan Schleifenbaum, Alexander Georgi, Michael Schmidt, Ralf Henkelmann, Georg Osterhoff, and Pierre Hepp. The single-suture technique for anterior cruciate ligament graft preparation provides similar stability as a three-suture technique: a biomechanical in vitro study in a porcine model. *Archives of Orthopaedic and Trauma Surgery*, 140(4):511–516, 2020. doi: 10.1007/s00402-020-03350-5.

[92] Xiaodong Chen, Changguo Xue, Kuanxin Li, Kecheng Mu, Cheng Yao, Zhiyan Wang, Hongzhi Chen, and Jun Zhang. Finite element analysis of anterior cruciate ligament reconstruction techniques: A comparison of the mechanical properties of all-inside fixation and traditional fixation. *Frontiers in Bioengineering and Biotechnology*, 12: 1438839, 2024. doi: 10.3389/fbioe.2024.1438839.

[93] J Dargel, M Gotter, K Mader, D Pennig, J Koebke, and R Schmidt-Wiethoff. Biomechanics of the anterior cruciate ligament and implications for surgical reconstruction. *Strategies in Trauma and Limb Reconstruction*, 2(1):1–12, 2007. doi: 10.1007/s11751-007-0016-6.

Appendix

ABAQUS Pull out mesh convergence Graphs

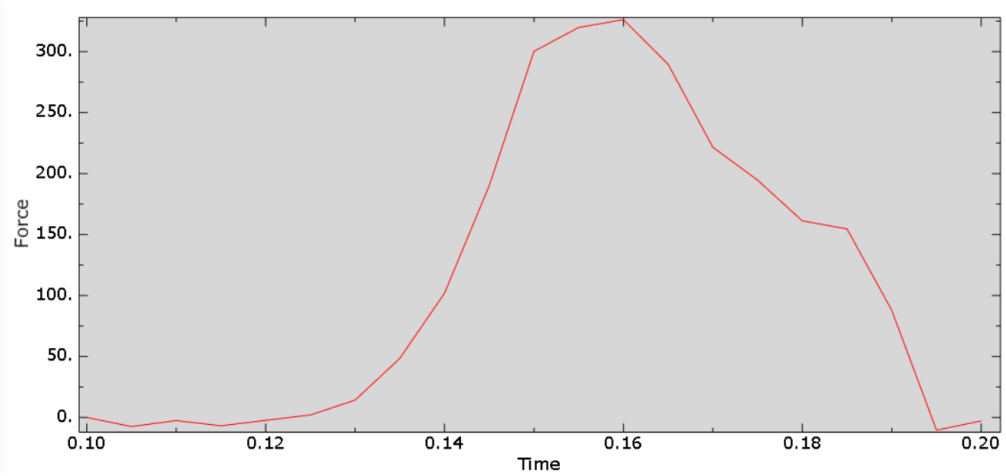


Figure 1

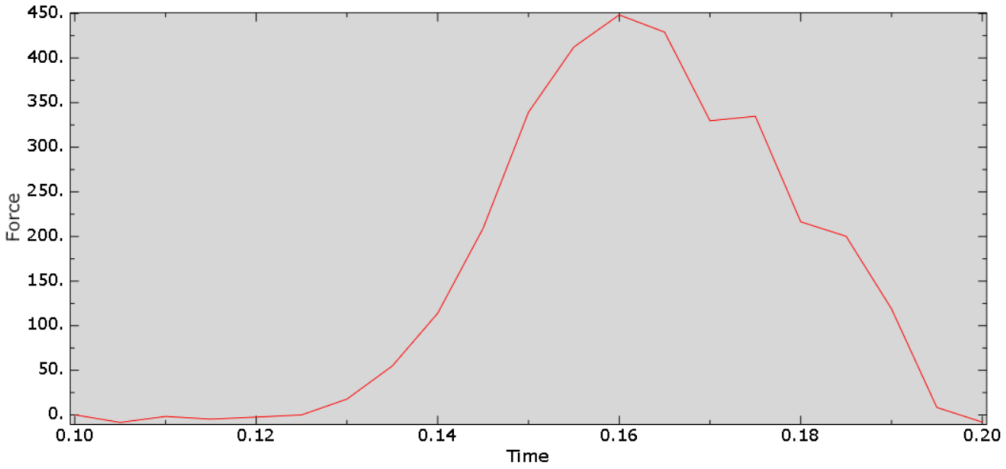


Figure 2

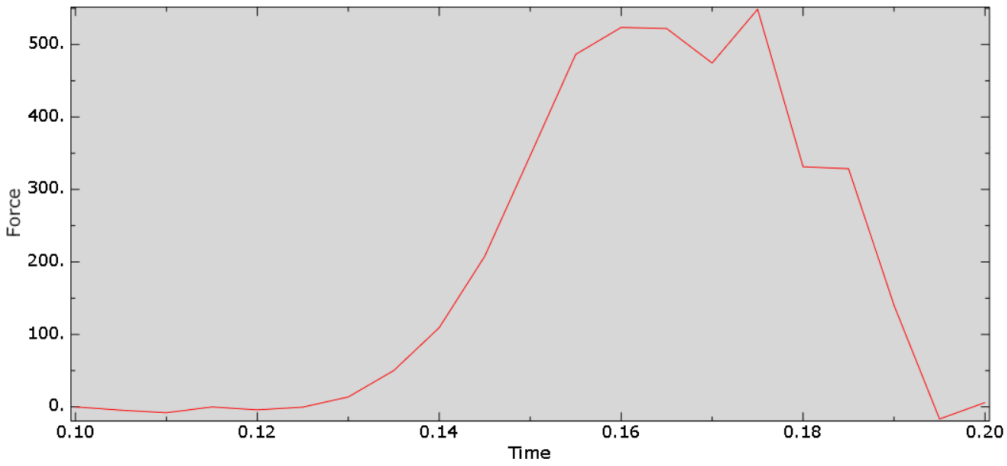


Figure 3

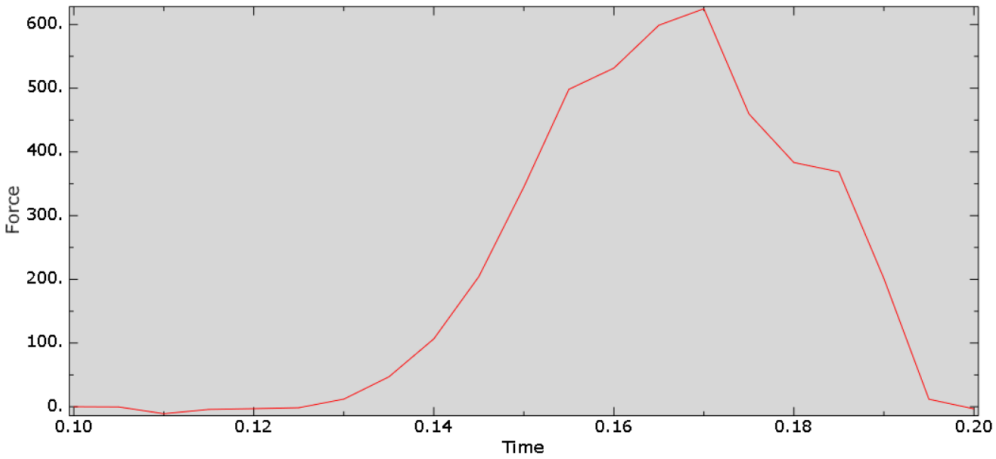


Figure 4

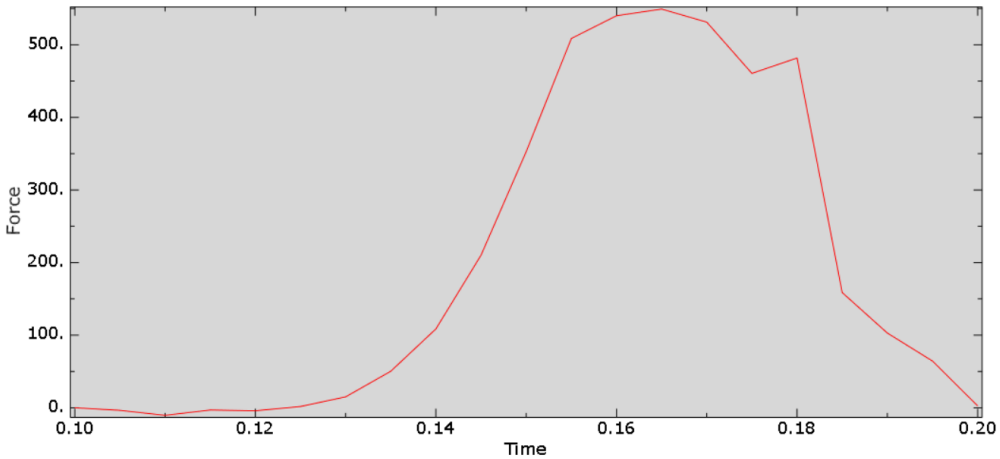


Figure 5

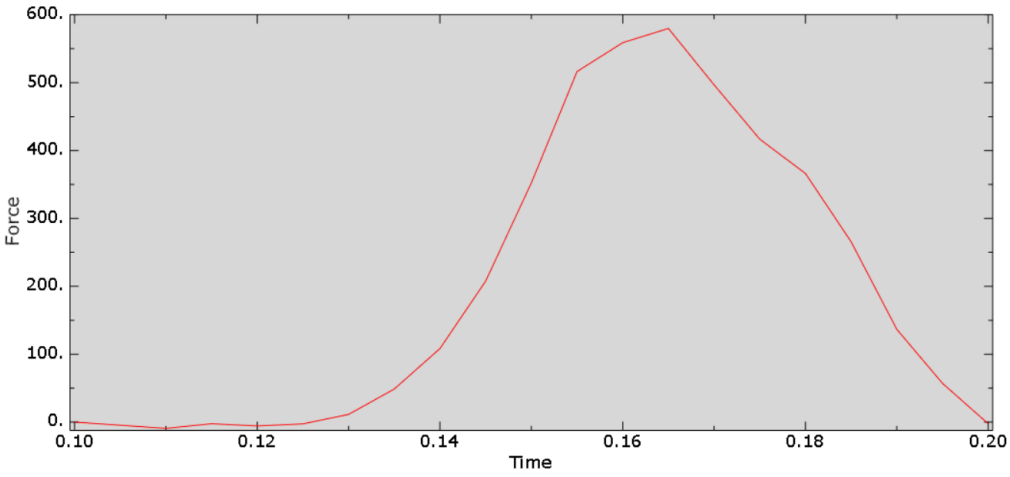


Figure 6

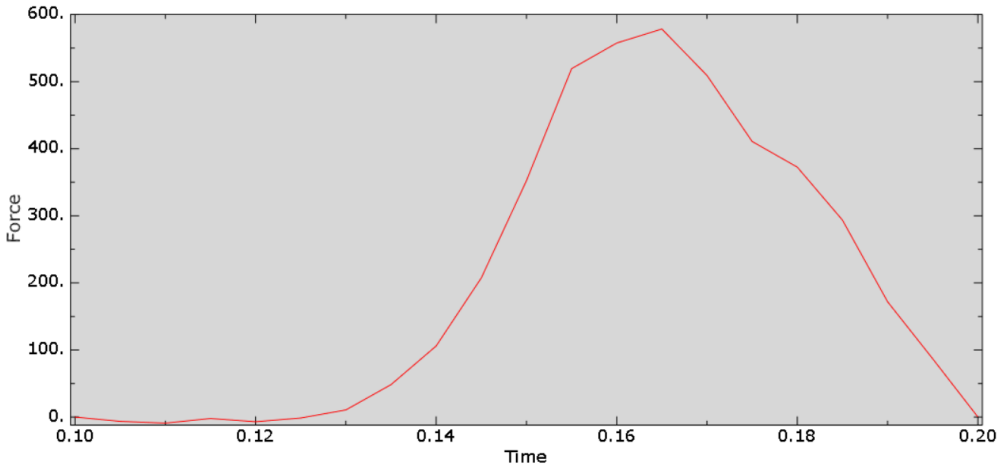


Figure 7

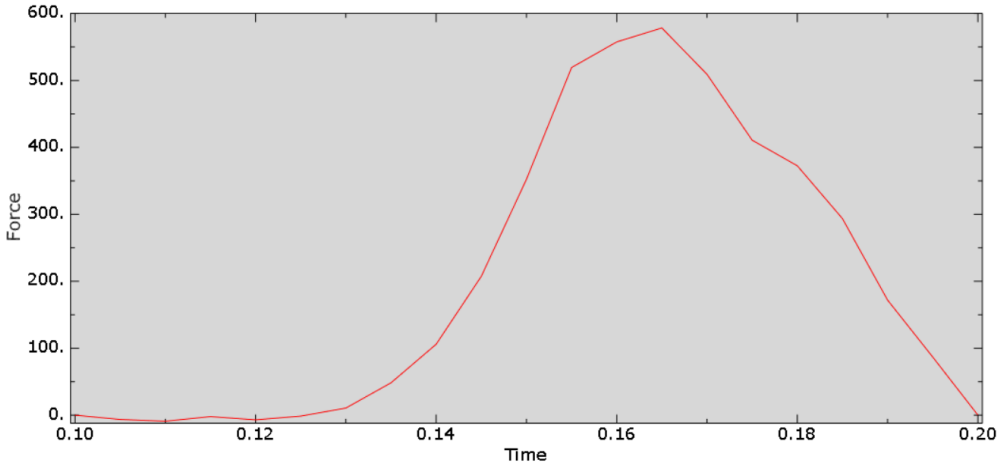


Figure 8

ABAQUS Insertion Force Graph

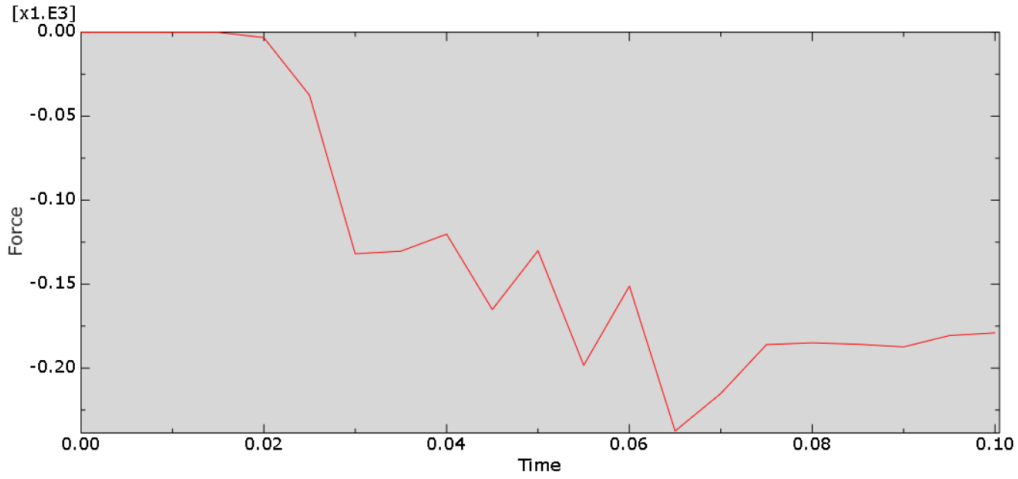


Figure 9

ABAQUS Kinetic and Internal Energy distribution (ALLKE/ALLIE) Across the Insertion and Pull-Out Steps

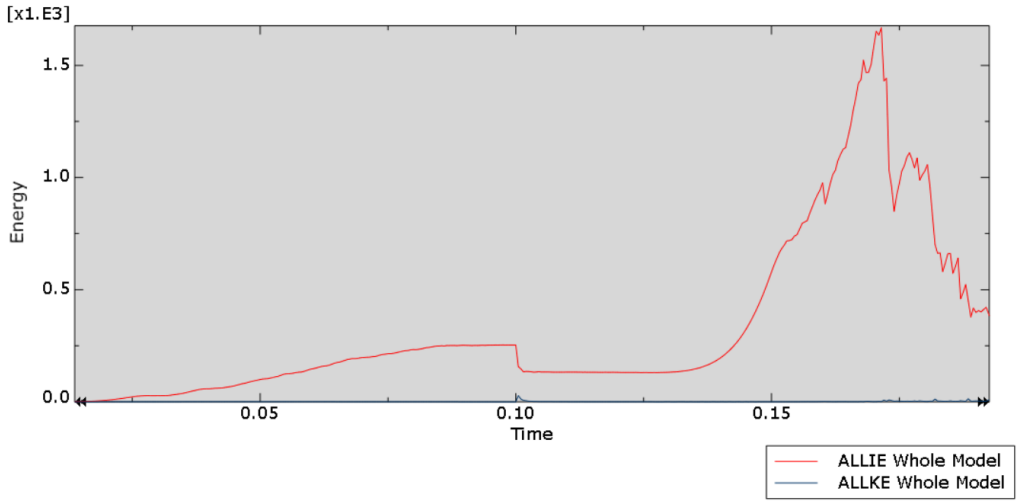


Figure 10

Linear regression Points to obtain Stiffness of 111.8 N/mm

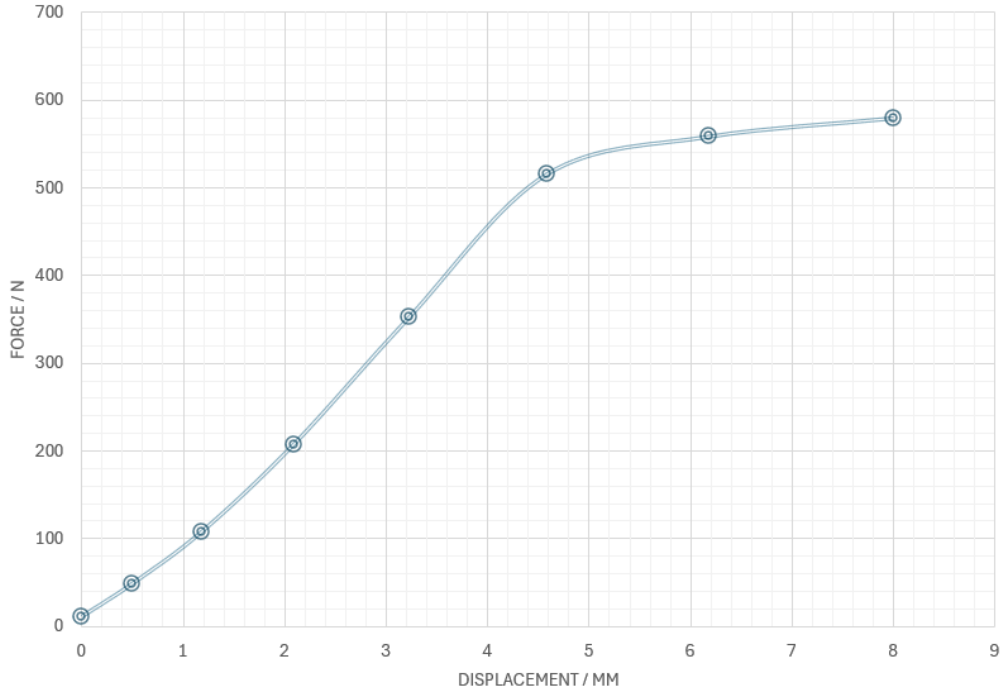


Figure 11

ABAQUS Tendon Displacement Nodes Graph

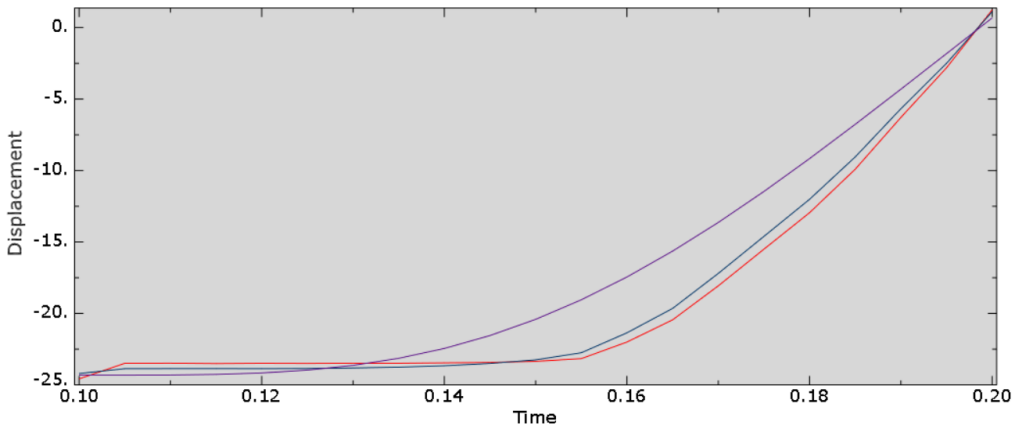


Figure 12

ABAQUS Refined Geometry Model Pull out Force Graph

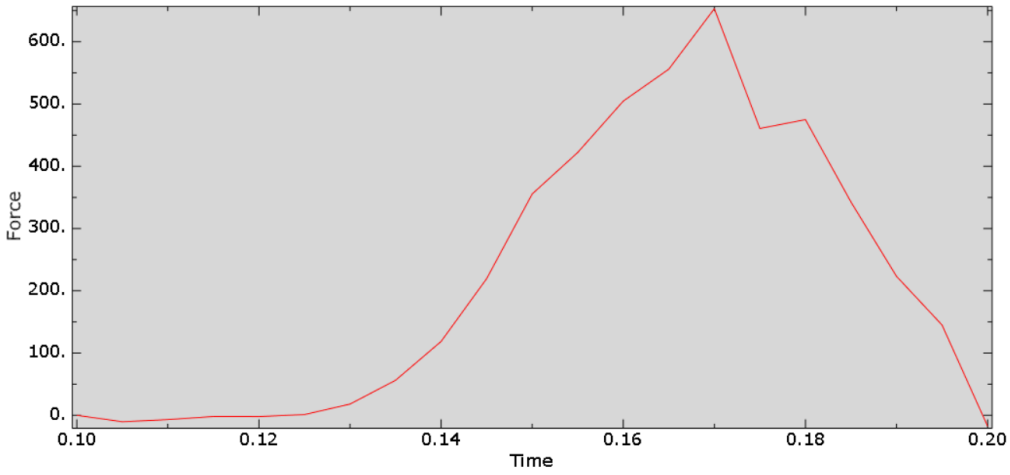


Figure 13